25

NASA CONTRACTOR REPORT **NASA CR-66663**

NASA CR-66663

GPO PRICE $ __________

CFSTI PRICE(S) $ __________

Hard copy (HC) 3-00

Microfiche (MF) .65

ff 653 July 65

FACILITY FORM 602

N68-31835	
(ACCESSION NUMBER)	(THRU)
105	1
(PAGES)	(CODE)
CR-66663	30
(NASA CR OR TMX OR AD NUMBER)	(CATEGORY)

FINAL REPORT

STUDY OF DIRECT VERSUS ORBITAL ENTRY FOR MARS MISSIONS

Volume V - Appendix C - Entry Configuration Analysis

Prepared by

MARTIN MARIETTA CORPORATION
DENVER, COLORADO

for

Langley Research Center

AUG 1968
RECEIVED
NASA STI FACILITY
INPUT BRANCH

NATIONAL AERONATUICS AND SPACE ADMINISTRATION • WASHINGTON, D.C. • AUGUST 1968

NASA CR-66663

FINAL REPORT

STUDY OF DIRECT VERSUS ORBITAL ENTRY FOR MARS MISSIONS

VOLUME V: APPENDIX C - ENTRY CONFIGURATION ANALYSIS

By Herbert C. Norman, Harry E. Sparhawk

Distribution of this report is provided in the interest of information exchange. Responsibility for the contents resides in the author or organization that prepared it.

Prepared under Contract No. NAS1-7976 by
MARTIN MARIETTA CORPORATION
Denver, Colorado

for

NATIONAL AERONAUTICS AND SPACE ADMINISTRATION

FOREWORD

This Final Report for the "Study of Direct Versus Orbital Entry for Mars Missions" (NASA Contract NAS1-7976) is provided in accordance with Part III A.4 of the contract schedule as amended. The report is in six volumes as follows:

NASA CR-66659 - Volume I - Summary;

NASA CR-66660 - Volume II - Parametric Studies, Final Analyses, and Conceptual Designs;

NASA CR-66661 - Volume III - Appendix A - Launch Vehicle Performance and Flight Mechanics;

NASA CR-66662 - Volume IV - Appendix B - Entry and Terminal Phase Performance Analysis;

NASA CR-66663 - Volume V - Appendix C - Entry Configuration Analysis;

NASA CR-66664 - Volume VI - Appendix D - Subsystem Studies and Parametric Data.

APPENDIX C

CONTENTS

Page

APPENDIX C -- ENTRY CONFIGURATION ANALYSIS 1
1. AEROHEATING ANALYSIS 1
2. HEAT SHIELD 47
3. AEROSHELL PARAMETRIC STUDY 73
4. REFERENCES . . . . 101 thru 103

Figure

C1 Mission Mode Study Conditions 2
C2 Pressure and Heating Distributions, Sphere-Cone 5
C3 Stagnation Point Convective Heating, VM-7, Orbital Entry R_N = 1.0 ft 6
C4 Maximum Laminar Shear Stress at Cone Edge, VM-7, Orbital Entry 7
C5 Stagnation Point Convective Heating, VM-8, Orbital Entry R_N = 1.0 ft 8
C6 Maximum Laminar Shear Stress (Cone Edge, VM-8), Orbital Entry 9
C7 VM-8 Orbit Mode Turbulent Flow Regime (Cone Edge) 11
C8 Stagnation Point Convective Heating, VM-7, Direct Entry 12
C9 Stagnation Point Equilibrium Radiation Heating, VM-7, Direct Entry 13
C10 Stagnation Point Nonequilibrium Radiation Heating, VM-7, Direct Entry 14
C11 VM-7 Direct Entry Turbulent Flow Regime (Cone Edge) 16
C12 Maximum Laminar Shear Stress (Cone Edge), VM-7, Direct Entry R_B = 7.5 ft 17
C13 Cone Edge Equilibrium Radiation Heating, VM-7, Direct Entry 70° Half-Angle Cone R_B = 7.5 ft . . . 18
C14 Cone Edge Nonequilibrium Radiation Heating, VM-7, Direct Entry 70° Half-Angle Cone 19
C15 Radiation Heating to Base, VM-7, Direct Entry R_B = 7.5 ft 20
C16 Stagnation Point Convective Heating, VM-4, Direct Entry R_N = 3.75 ft 21

APPENDIX C

Page

C56 Aeroshell Parametric Studies, Nose Cap Weight . . 81
C57 Aeroshell Parametric Studies, Conical Shell Weight 81
C58 Aeroshell Parametric Studies, Aft Frame Weight . . 82
C59 Aeroshell Parametric Studies, Aft Frame Weight . . 82
C60 Aeroshell Parametric Studies, Total Flap Weight . 83
C61 Aeroshell Parametric Studies, Airmat Weight . . . 83
C62 Structural Weight, Orbital Entry, V_E = 14 765 fps, γ = -20° 85
C63 Structural Weight, Orbital Entry, V_E = 14 765 fps, γ = -38° 85
C64 Structural Weight, Direct Entry, V_E = 21 000 fps, γ = -30° 86
C65 Structural Weight, Direct Entry, V_E = 21 000 fps, γ = -38° 86
C66 Structural Weight, Direct Entry, V_E = 24 000 fps, γ = -30° 87
C67 Structural Weight, Direct Entry, V_E = 24 000 fps, γ = -38° 87
C68 Structural Weight, Direct Entry with Flaps, V_E = 21 000 fps, γ = -30° 88
C69 Structural Weight, Direct Entry with Flaps, V_E = 21 000 fps, γ = -38° 88
C70 Structural Weight, Direct Entry with Flaps, V_E = 24 000 fps, γ = -30° 89
C71 Structural Weight, Direct Entry with Flaps, V_E = 24 000 fps, γ = -38° 89
C72 Structural Weight, Direct Entry with Airmat, V_E = 21 000 fps, γ = -30° 90
C73 Structural Weight, Direct Entry with Airmat, V_E = 21 000 fps, γ = -38° 90
C74 Structural Weight, Direct Entry with Airmat, V_E = 24 000 fps, γ = -30° 91
C75 Structural Weight, Direct Entry with Airmat, V_E = 24 000 fps, γ = -38° 91
C76 Airmat Cone Configuration 98

Table
C1 Material Properties of SLA-561 48
C2 Material Properties of ESA-5500M 49
C3 Material Properties of PPA-1078 51

APPENDIX C

ENTRY CONFIGURATION ANALYSIS

APPENDIX C

1. AEROHEATING ANALYSIS

Parametric Data

Definition of parameters in study. - Parameters studied are defined in the following paragraphs.

Entry parameters: The maximum entry flightpath angles and the ranges of velocities to be used in the Mars Mission Mode Study were specified in reference C1. The minimum flightpath angles were specified to be 2σ above skipout. The resulting V_E, γ_E boxes are shown in figure C1 for both the orbit and direct entry modes. The specific V_E, γ_E combinations for which aeroheating data were generated are also shown in figure C1.

An entry weight range of 500 to 10 000 lb is specified by reference C1. The possible aeroshell diameter is large (30 ft) when aeroshell extensions are considered. It is convenient to use ballistic coefficient in parametric entry analyses rather than specific weights and diameters. A ballistic coefficient range of 0.1 to 0.6 was used to cover the possible combinations of entry weights and aeroshell diameters. An intermediate value of 0.3 was used so that variations with ballistic coefficient can be defined.

Configurations: A 70° half-angle cone was selected as the reference configuration during the Phase B Voyager study (ref. C2). Therefore, the orbital mode analysis was based on the 70° cone configuration with a nose-to-base radius ratio of 0.50.

A valid mission mode comparison is made by using the 70° cone for the direct mode as well. Actually the larger axial force coefficient of the 70° should be even more advantageous for performance-limited systems of the current study than for the Phase B Voyager system. However, limited aeroheating data have been obtained for the 60° cone so that comparisons can be made. The nose-to-base bluntness ratio was assumed to be 0.50 to eliminate an additional variable.

This aeroheating analysis is generally limited to two points on the aeroshell. These points are the stagnation point and the cone edge. Analyses at these two points are considered adequate for defining the heating to the aeroshell and the ablator weight for this study.

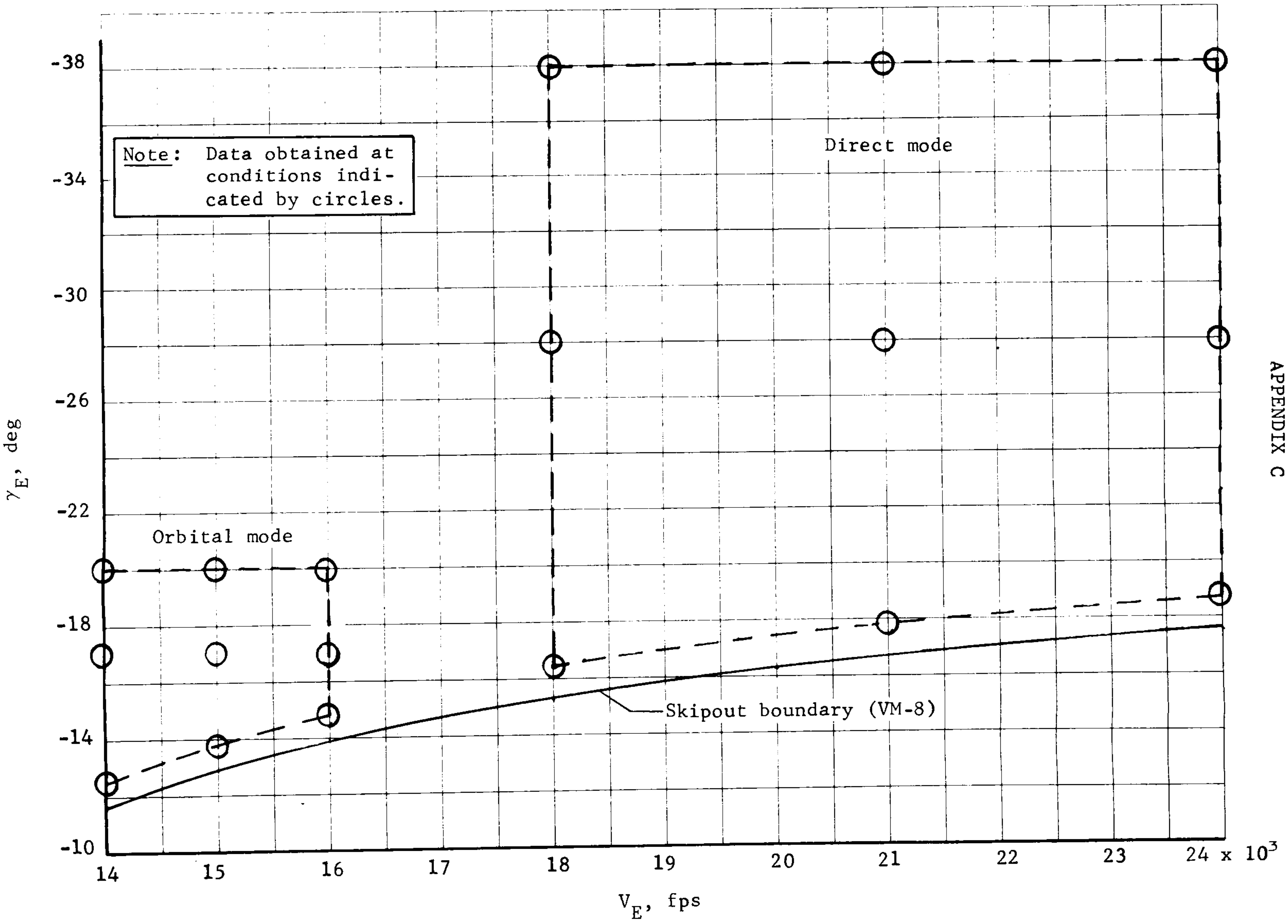

Figure C1.- Mission Mode Study Conditions

APPENDIX C

Aeroshell extensions are considered to be extensions of a 15-ft diameter aeroshell. Cone edge heating data are applied to extensions with proper consideration of extended diameter.

Atmospheres: The convective heating is primarily a function of the physical characteristics of the atmosphere, i.e., scale height, rather than of composition. The highest heating rates are encountered in the low-scale height atmospheres, while the greatest total heat loads occur in the low-scale height atmospheres. The VM-7 and VM-8 atmospheres were found to be critical in the Phase B Voyager study and were used in the Mars Mission Mode Study for orbital entry.

Radiation heating, which becomes significant for direct mode entry, is a strong function of atmosphere composition. VM-7 is still used as the critical high-scale height atmosphere because the composition is the same for all the high-scale height atmospheres. VM-4 was used as the critical low-scale height atmosphere because of the greater radiation intensity at high velocities in this atmosphere than in VM-8.

Scale factors and uncertainties: Convective laminar heating and radiation heat transfer can be scaled to any aeroshell size. Turbulent convective heating scale factors are provided with the data:

Stagnation convective heat transfer rate scales as the inverse ratio of the square root of the nose radii;

Equilibrium radiation heat transfer rate scales directly as nose radius or aeroshell diameter;

Nonequilibrium radiation is considered to be independent of aeroshell size.

There are uncertainties associated with the prediction of heat transfer in the Martian atmosphere at the current time. The following uncertainty factors have been assigned to the predicted heating rates for design purposes:

Convective heat transfer, 1.5;

Equilibrium radiation, 2.0;

Nonequilibrium radiation, 3.0;

Base heating, convective and radiation, 2.0.

APPENDIX C

Aeroheating data. - The aeroheating data presented in this appendix consist of summaries of maximum heating rates, total heating loads, and aerodynamic shear stresses. Such summaries allow rapid evaluations of the effects of V_E, γ_E and B and comparisons of the mission mode. Time histories of entry trajectory and heating parameters are available in reference C3 for the entire matrix of cases worked in this study. The analysis techniques used in generating these data are discussed in the subsection of this appendix entitled "Analysis Techniques."

Normalized pressure and laminar convective heating distributions are given in figure C2 for both the 60 and 70° half-angle cones. The design stagnation pressure is used as twice the dynamic pressure. Dynamic pressure summaries are presented in Section 1 of Appendix B. These normalized distributions are independent of atmosphere and entry parameters.

Orbit mode: For the VM-7 atmosphere, the summary of total heat (Q) and maximum heating rate ($\dot{q}$) is given in figure C3 for the stagnation point of a 1.0-ft radius sphere. These data scale as the inverse of the square root of the nose radius. Maximum heating rates increase with increases in entry velocity, flightpath angle, and ballistic coefficient. Total heating loads increase with increases in entry velocity and ballistic coefficient and increase with decreasing flightpath angle.

Laminar flow exists over the cone surface during the entire heating pulse for the matrix of parameters studied in the orbit mode. Thus, the heating distribution of figure C2 can be used with the properly scaled data of figure C3 to obtain maximum heating distributions for any size aeroshell. Maximum values of the laminar aerodynamic shear stress at the edge of the cone are shown in figure C4. The shear stress is a weak function of aeroshell diameter, and it is considered to be independent of diameter for this parametric study. Convective base heating is estimated to be 2% of stagnation.

For the VM-8 atmosphere, summary stagnation point heating data are presented in figure C5. Higher maximum heating rates and lower total heat loads are experienced in VM-8 than in VM-7 for a given set of conditions. Maximum laminar shear stress data are shown in figure C6.

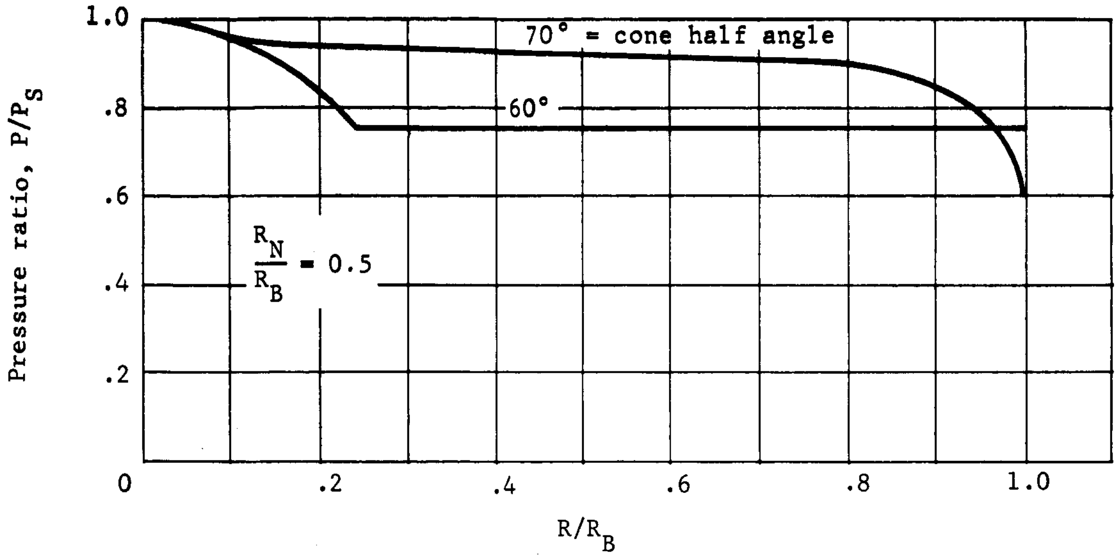

(a) Pressure Distribution

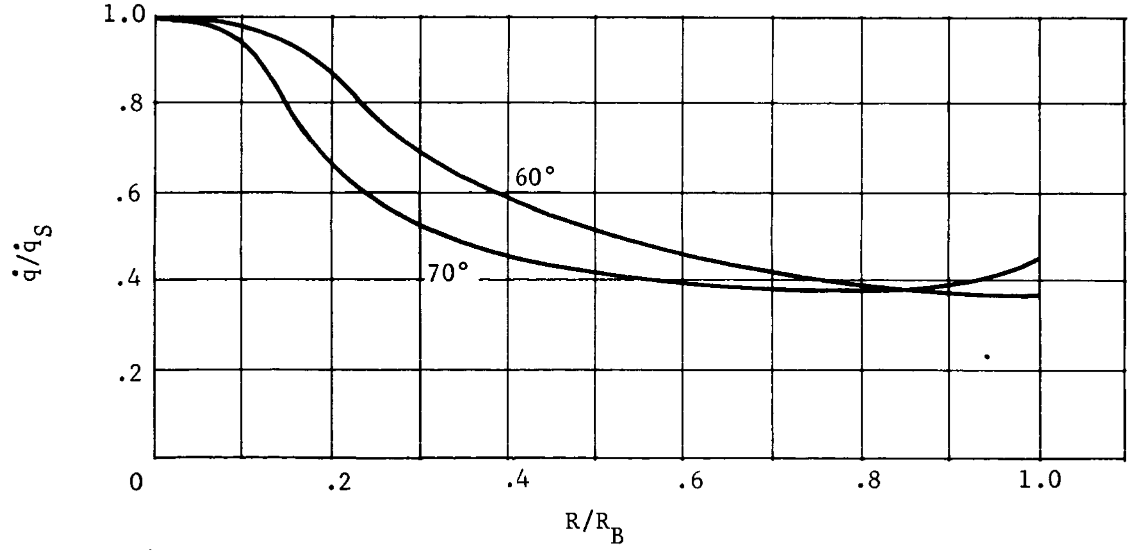

(b) Laminar Convective Heating Rate Distribution

Figure C2.- Pressure and Heating Distributions, Sphere-Cone

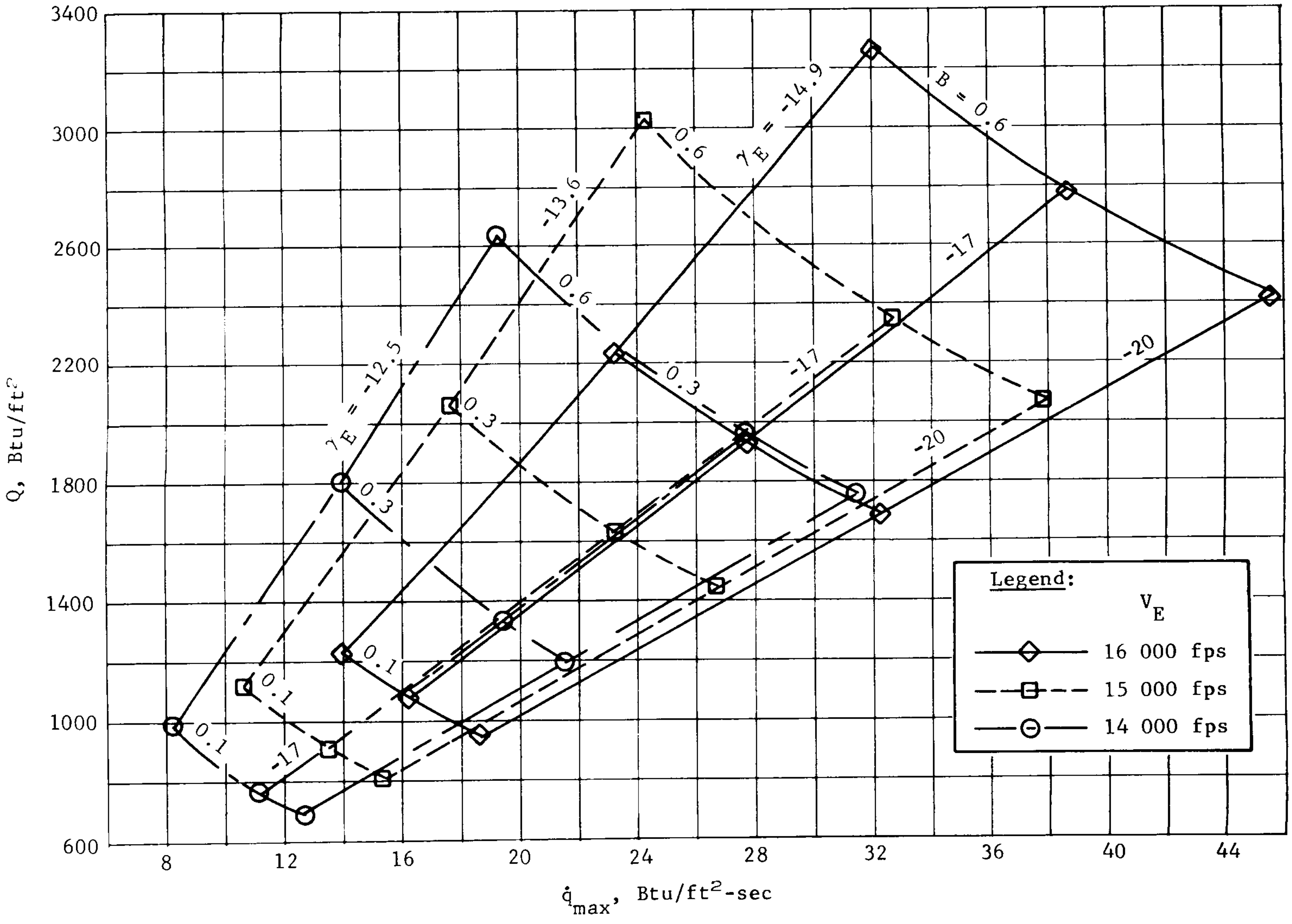

Figure C3.- Stagnation Point Convective Heating, VM-7, Orbital Entry R_N = 1.0 ft

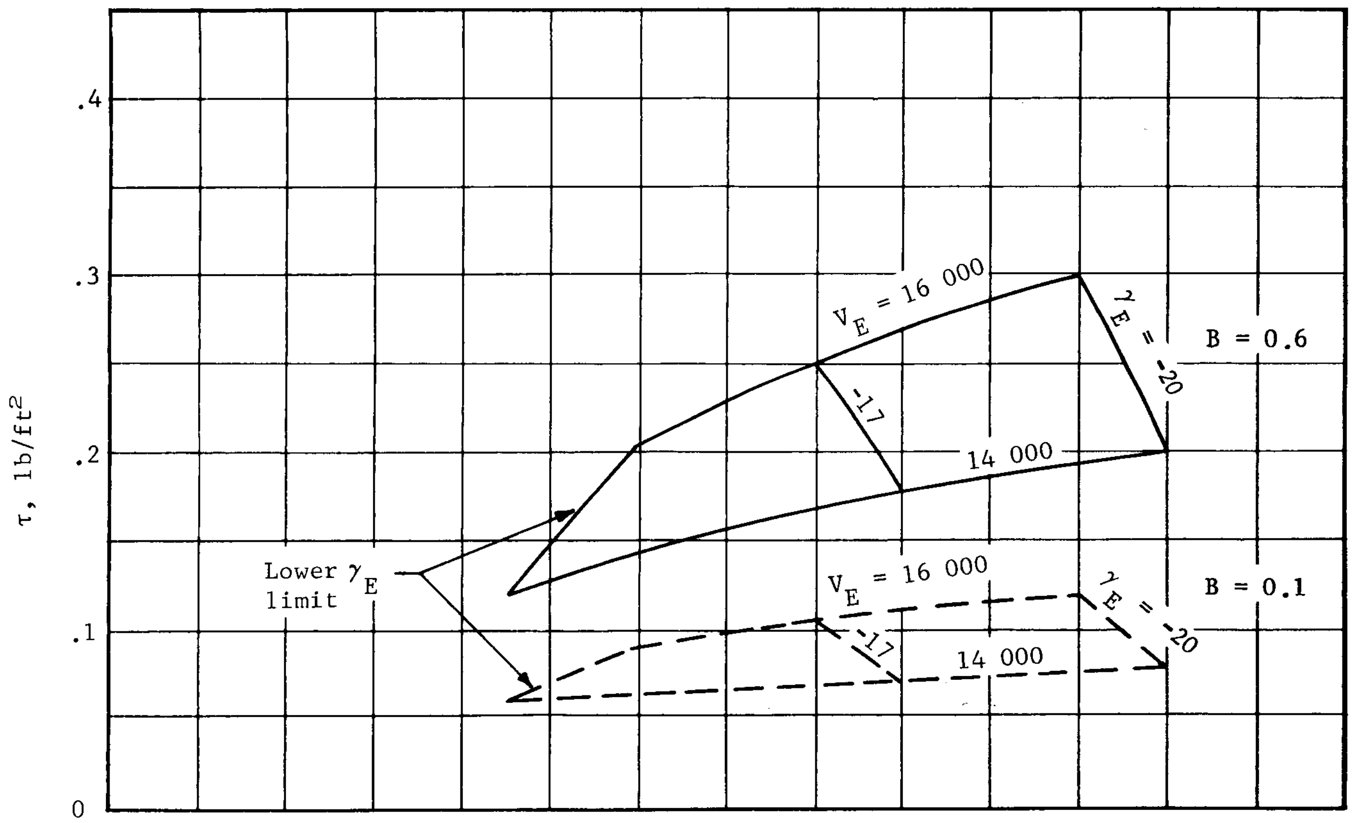

Figure C4.- Maximum Laminar Shear Stress at Cone Edge, VM-7, Orbital Entry

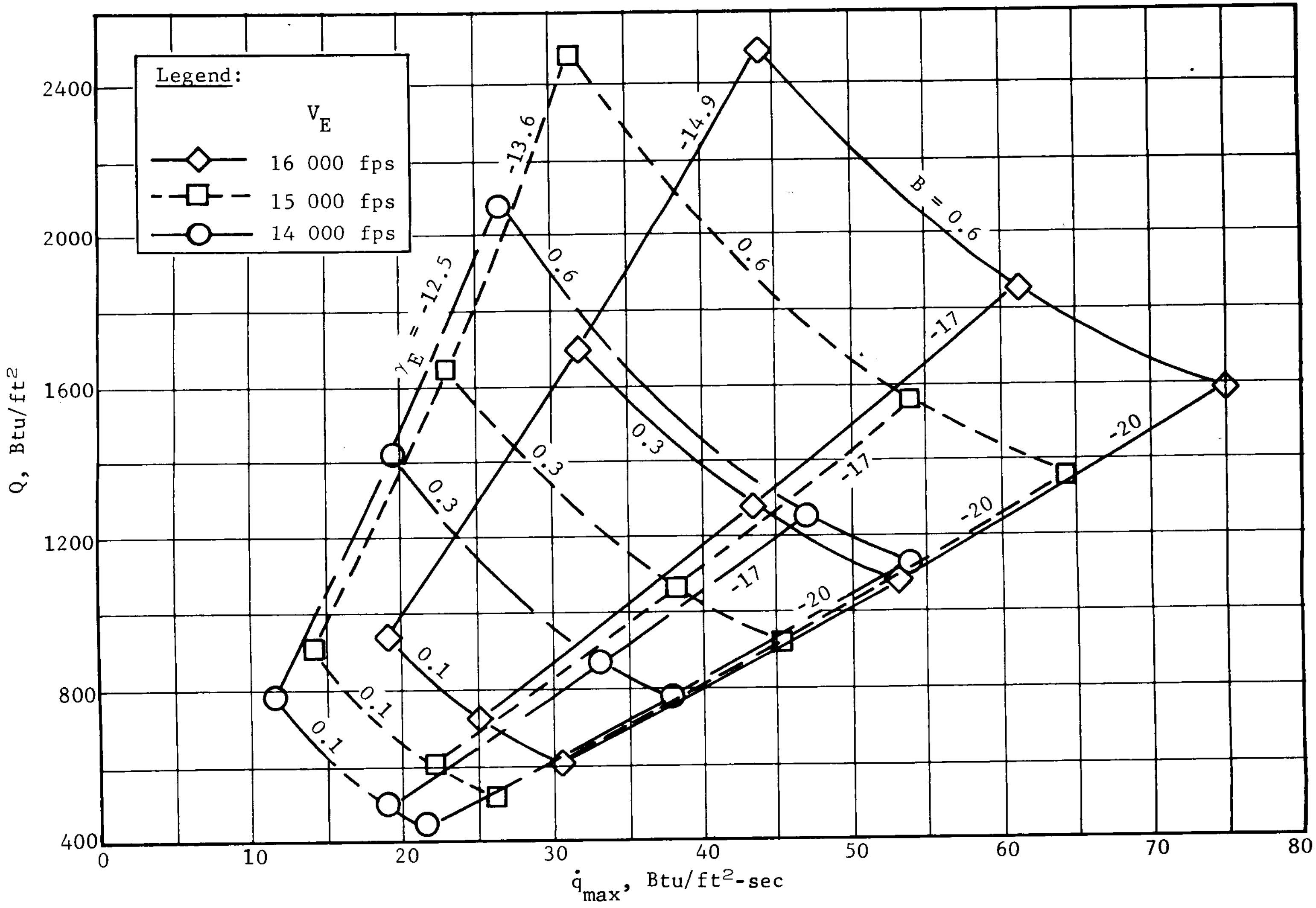

Figure C5.- Stagnation Point Convective Heating VM-8, Orbital Entry R_N = 1.0 ft

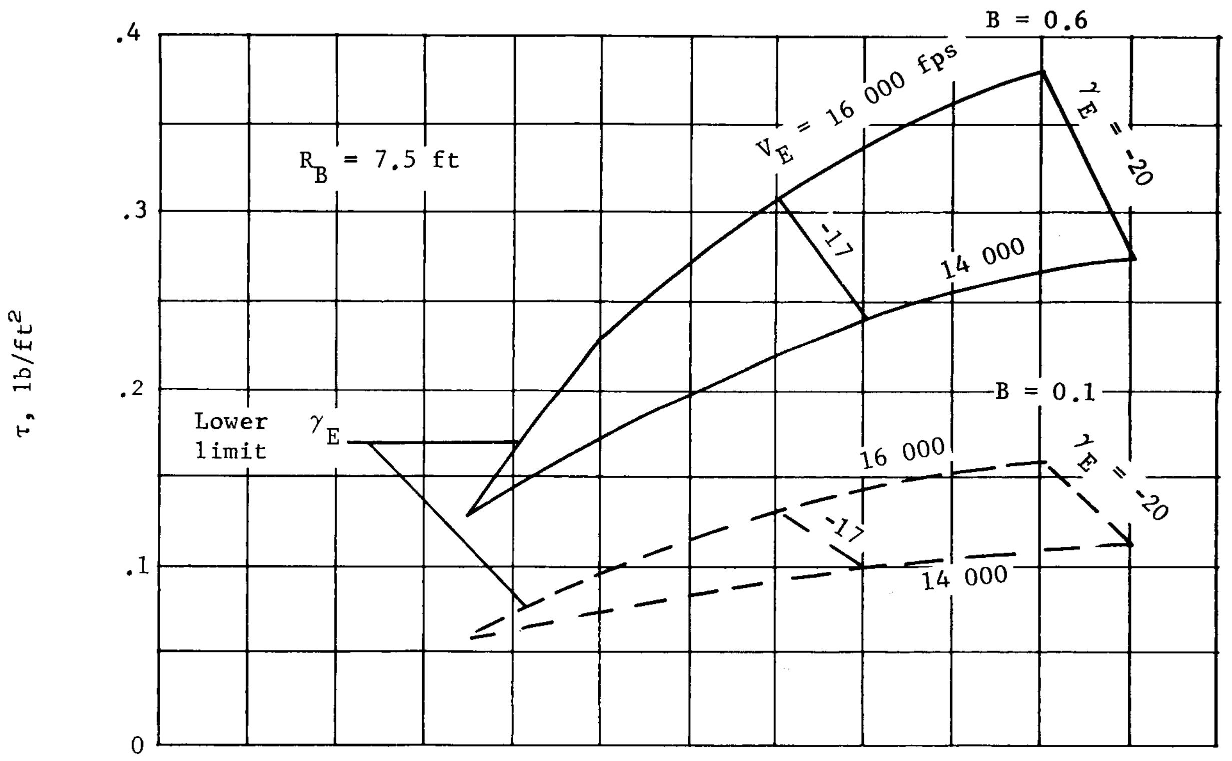

Figure C6.- Maximum Laminar Shear Stress (Cone Edge) VM-8, Orbital Entry

Transition to turbulence can occur at the cone edge for a limited range of ballistic coefficients, flightpath angles, and aeroshell diameters. Turbulent flow occurs at the edge of the cone for aeroshell diameters greater than 12 ft for the combinations of B and γ_E shown in figure C7. The conditions for which turbulent flow was found in this study do not vary significantly over the entry velocity range of 14 000 to 16 000 fps. The transition Reynolds' number is reached near the time of maximum heating rate for all cases because the Reynolds' number is increasing rapidly with time. For the parametric study, it is assumed that transition in VM-8 occurs at the time of maximum heating and that the flow goes turbulent over the entire cone at this time. Factors have been derived to account for the effects of turbulence on heating rate and shear stress. These factors are considered to be constant with time during entry and to apply over the small range of entry conditions and aeroshell diameters of concern. These factors, also shown in figure C7, are:

Turbulent edge heating rate/stagnation heating rate $\left(\dot{q}_{e_{TURB}}/\dot{q}_s\right) = 1.8$;

Turbulent edge total heating/stagnation point total heating $\left(Q_{e_{TURB}}/Q_s\right) = 1.12$;

Turbulent edge shear stress/laminar edge shear stress $\left(\tau_{e_{TURB}}/\tau_{e_{LAM}}\right) = 3.5$.

Direct mode, 70° cone: For the VM-7 atmosphere, direct mode heating data are presented for a 15-ft diameter aeroshell. The nose radius is 3.75 ft. Stagnation point convective heating data are presented in figure C8. Equilibrium radiation heating data for the stagnation point are given in figure C9. Nonequilibrium radiation heating data are presented in figure C10.

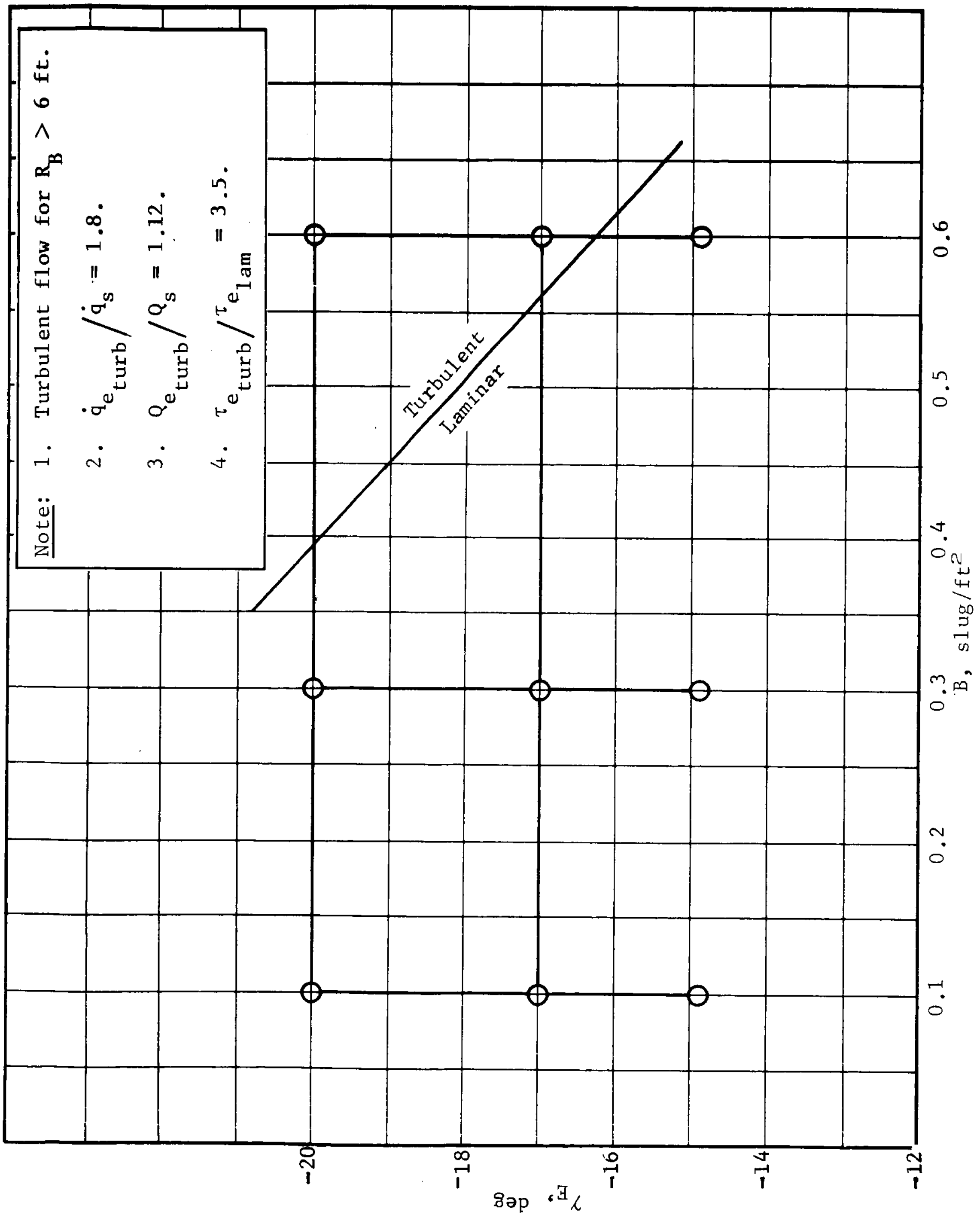

Note:
1. Turbulent flow for $R_B > 6$ ft.
2. $\dot{q}_{e_{turb}}/\dot{q}_s = 1.8$.
3. $Q_{e_{turb}}/Q_s = 1.12$.
4. $\tau_{e_{turb}}/\tau_{e_{lam}} = 3.5$.

Figure C7.- VM-8 Orbit Mode Turbulent Flow Regime (Cone Edge)

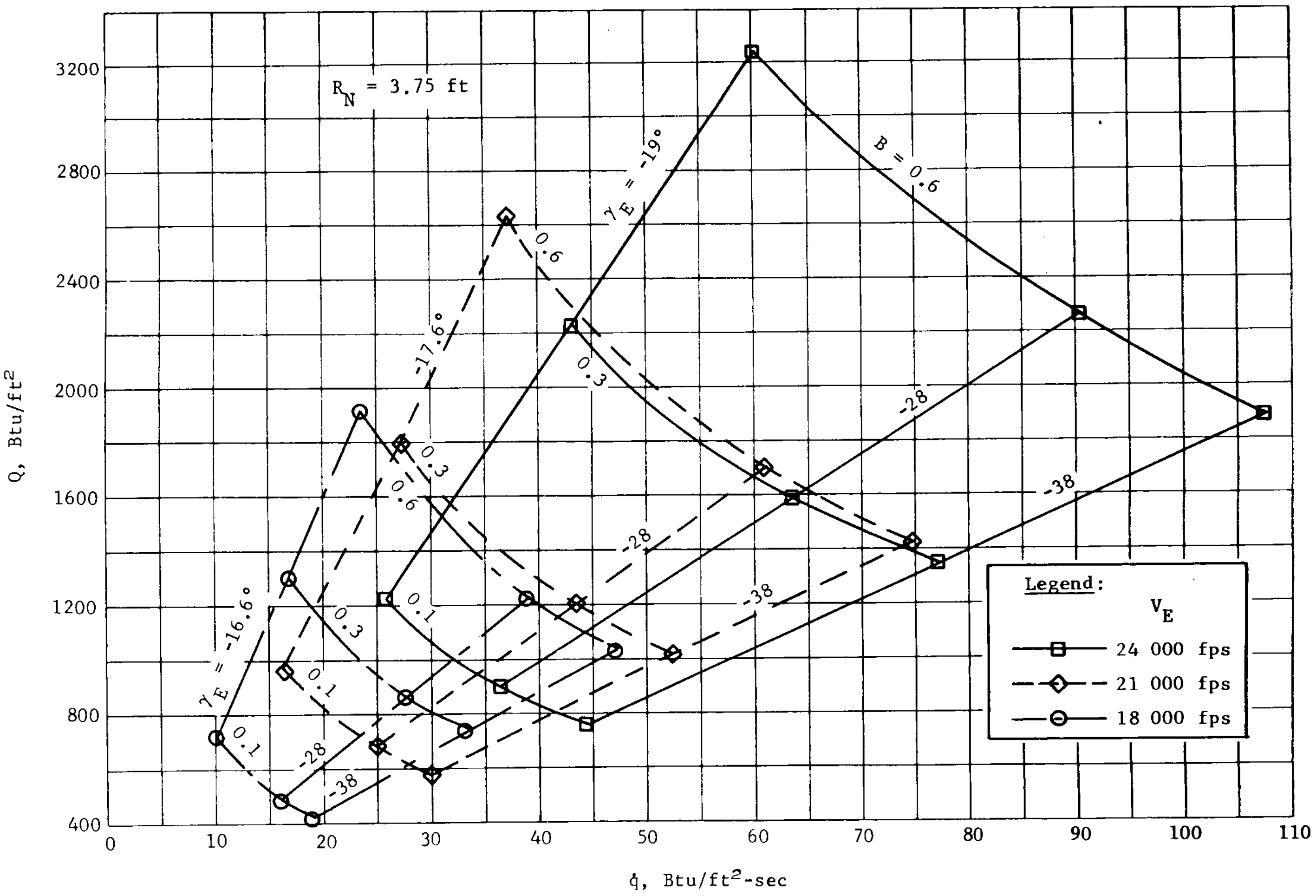

Figure C8.- Stagnation Point Convective Heating, VM-7, Direct Entry

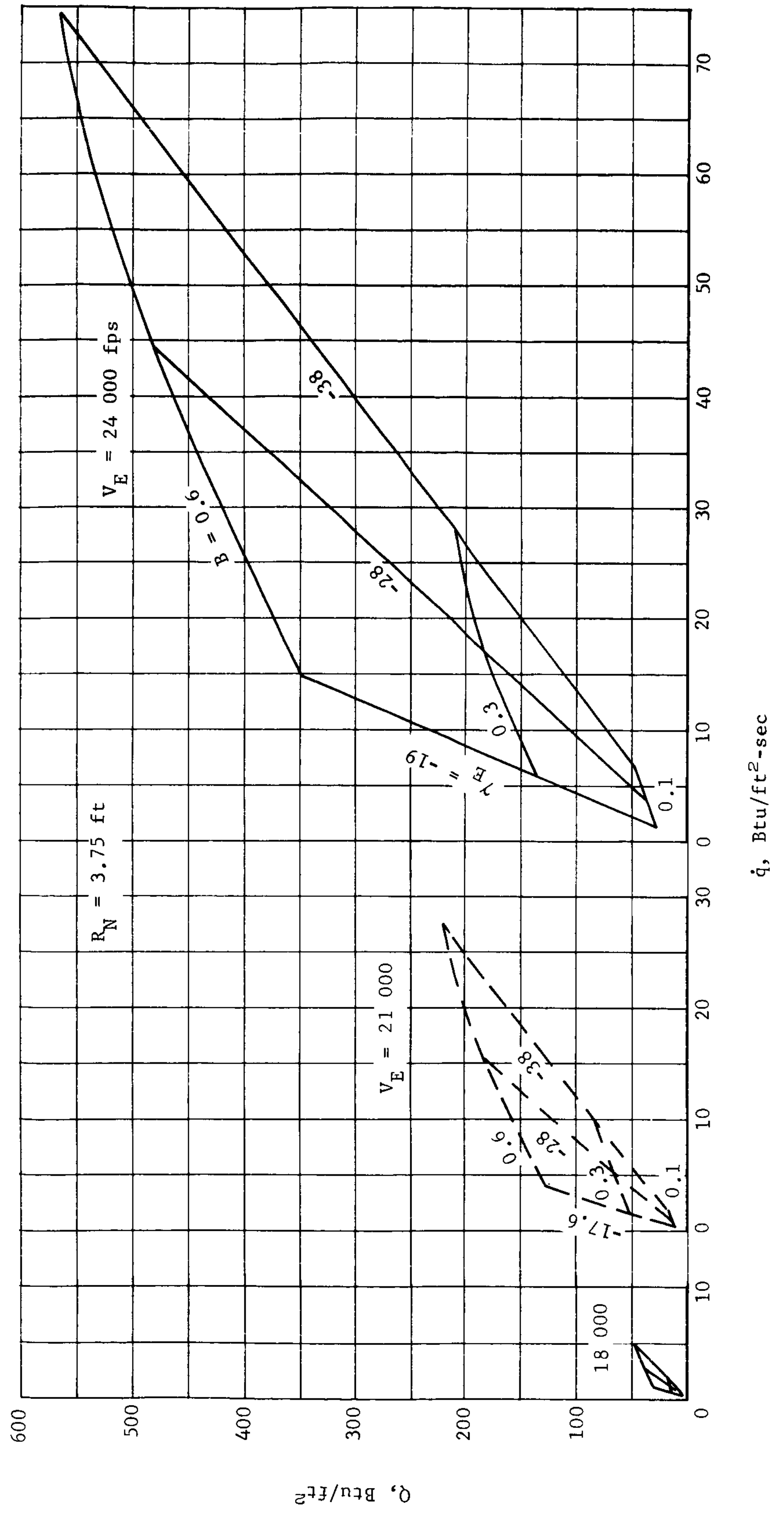

Figure C9.- Stagnation Point Equilibrium Radiation Heating, VM-7, Direct Entry

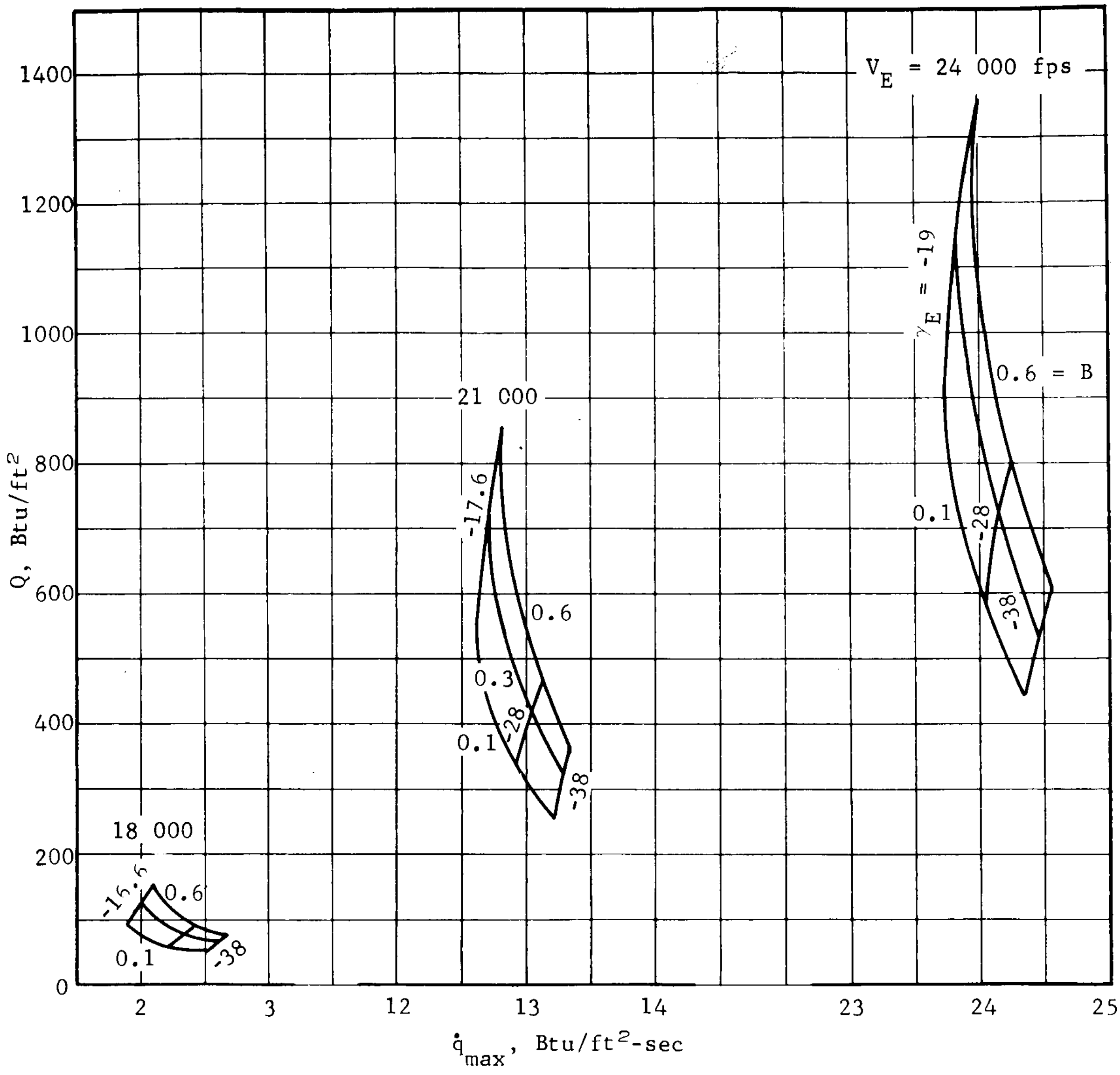

Figure C10.- Stagnation Point Nonequilibrium Radiation Heating, VM-7, Direct Entry

Turbulent flow conditions exist at the cone edge for a range of conditions similar to the orbit mode in VM-8. This range of conditions is indicated in figure C11. In this case, the transition to turbulence occurs at about the time that the heating rate has decreased to one-half its maximum. The factors used to account for the effects of turbulence are:

Turbulent edge heating rate/stagnation heating rate $\left(\dot{q}_{e_{TURB}}/\dot{q}_{s}\right) = 1.4$;

Turbulent edge total heating/stagnation point total heating $\left(Q_{e_{TURB}}/Q_{s}\right) = 0.8$;

Turbulent edge shear stress/laminar edge shear stress $\left(\tau_{e_{TURB}}/\tau_{e_{LAM}}\right) = 3.0$.

This combination of B, γ, and diameter for which turbulence exists is considered to be independent of entry velocity. Laminar maximum shear stress values are shown in figure C12 and are considered independent of aeroshell diameter. Equilibrium radiation heating at the cone edge is given in figure C13, and nonequilibrium heating is given in figure C14.

Radiation heating to the base is summarized in figure C15. The convective heating is estimated to be 2% of stagnation.

For the VM-4 atmosphere, stagnation point convective heating data are presented in figure C16. Stagnation point radiation equilibrium data are shown in figure C17, and radiation nonequilibrium data are shown in figure C18.

Turbulent flow conditions occur at the cone edge for a wide range of the V_E, γ_E, B, R_B matrix studied. Therefore, it is necessary to provide more detailed information on the effects of turbulence than for the previous cases. The turbulent flow boundaries are defined in figure C19 in terms of γ_E, B, and R_B. These boundaries are still relatively independent of entry velocity. Transition to turbulence occurs very near the time of maximum convective heating rate for all cases in this low-scale height atmosphere. Transition is assumed to occur at $\dot{q}_{max}$ for this study. Turbulent heating ratios $\left(\dot{q}_{e_{TURB}}/\dot{q}_{s}\right)$ at the edge are presented in figure C20 as functions of V_E, γ_E, B, and R_B. Laminar shear stress data are shown in figure C21, and turbulent shear stress data are shown in figure C22. These data are considered to be independent of aeroshell size.

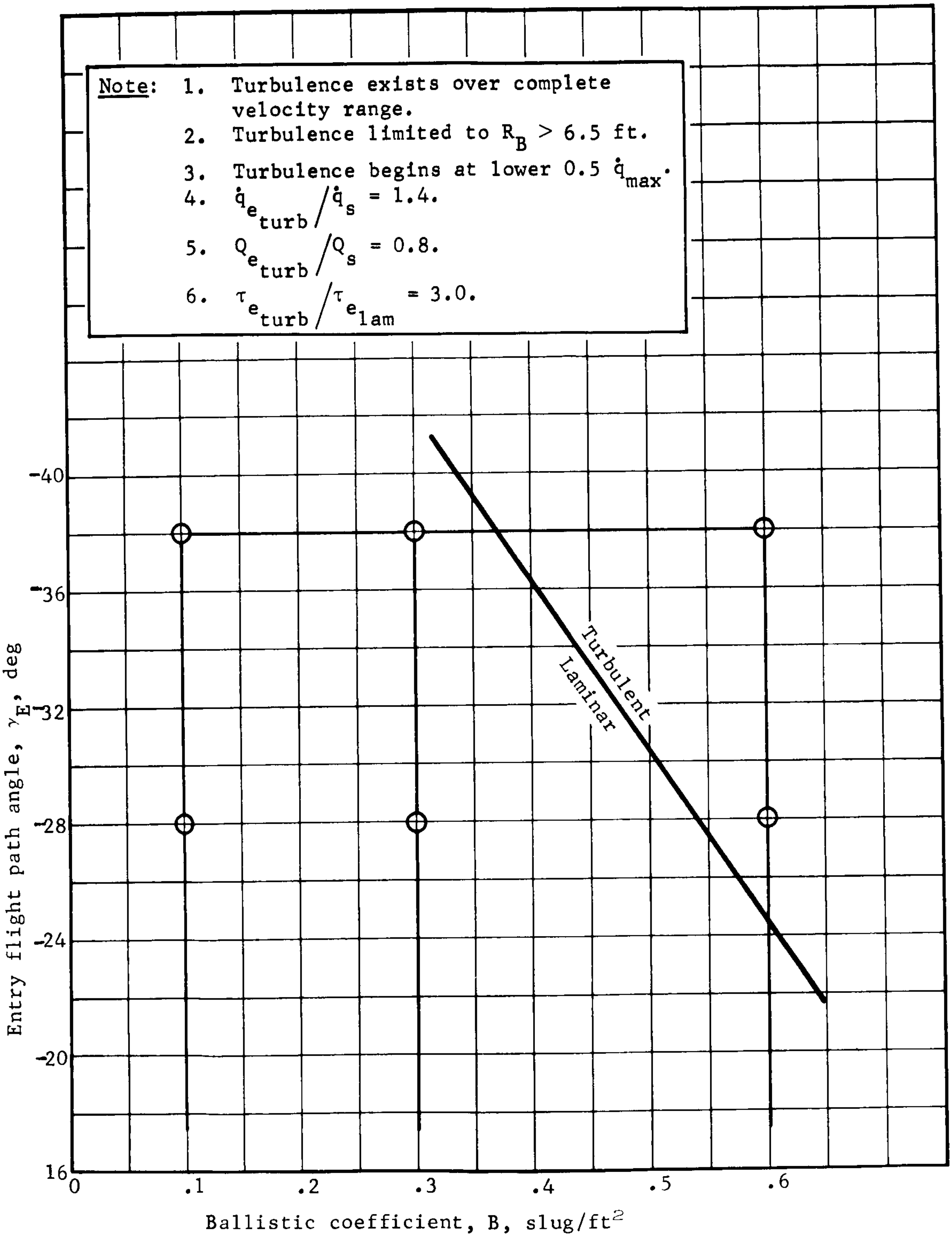

Note:
1. Turbulence exists over complete velocity range.
2. Turbulence limited to $R_B > 6.5$ ft.
3. Turbulence begins at lower $0.5\ \dot{q}_{max}$.
4. $\dot{q}_{e_{turb}} / \dot{q}_s = 1.4$.
5. $Q_{e_{turb}} / Q_s = 0.8$.
6. $\tau_{e_{turb}} / \tau_{e_{lam}} = 3.0$.

Figure C11.- VM-7 Direct Entry Turbulent Flow Regime (Cone Edge)

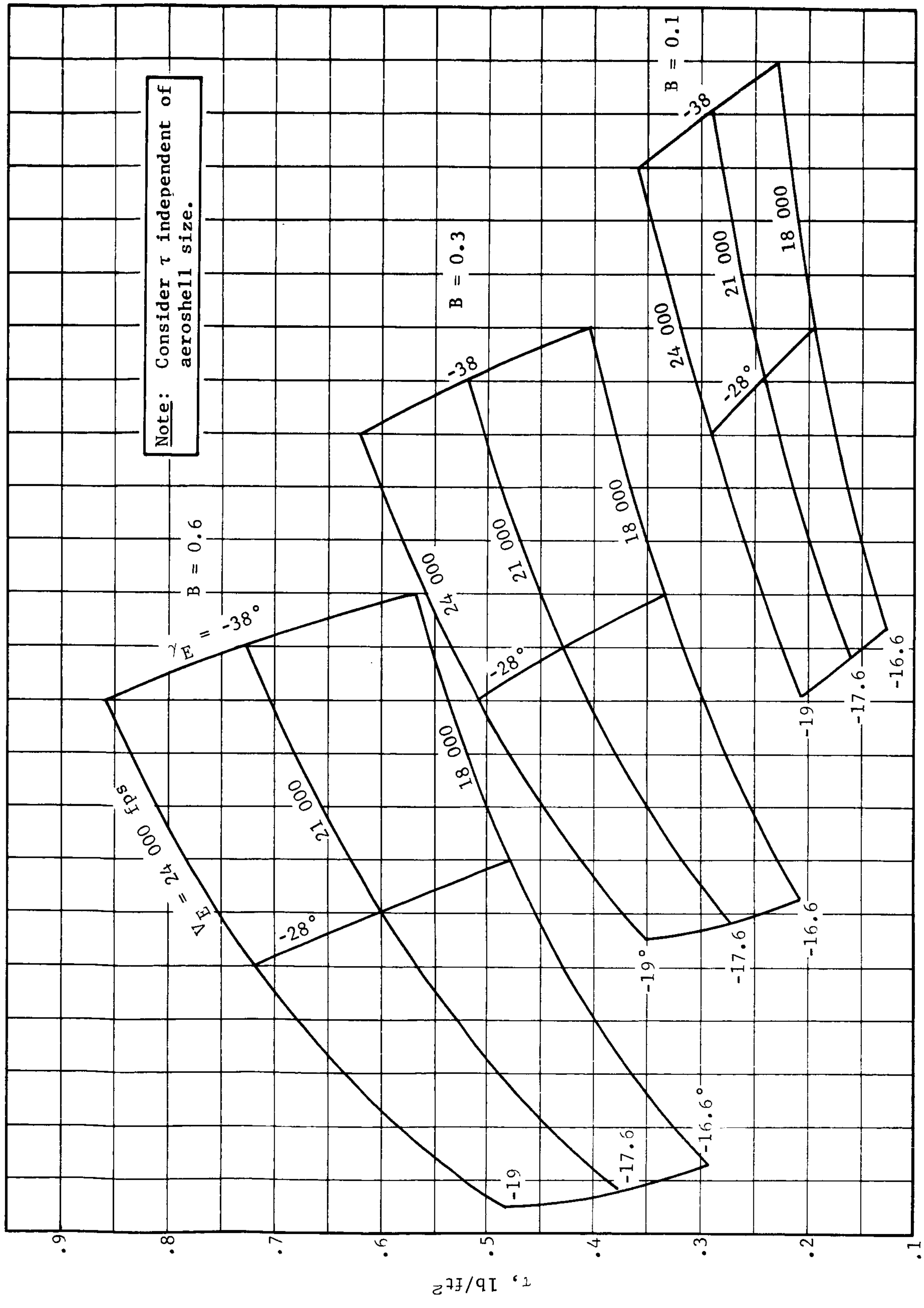
Note: Consider τ independent of aeroshell size.

Figure C12.- Maximum Laminar Shear Stress (Cone Edge) VM-7, Direct Entry R_B = 7.5 ft

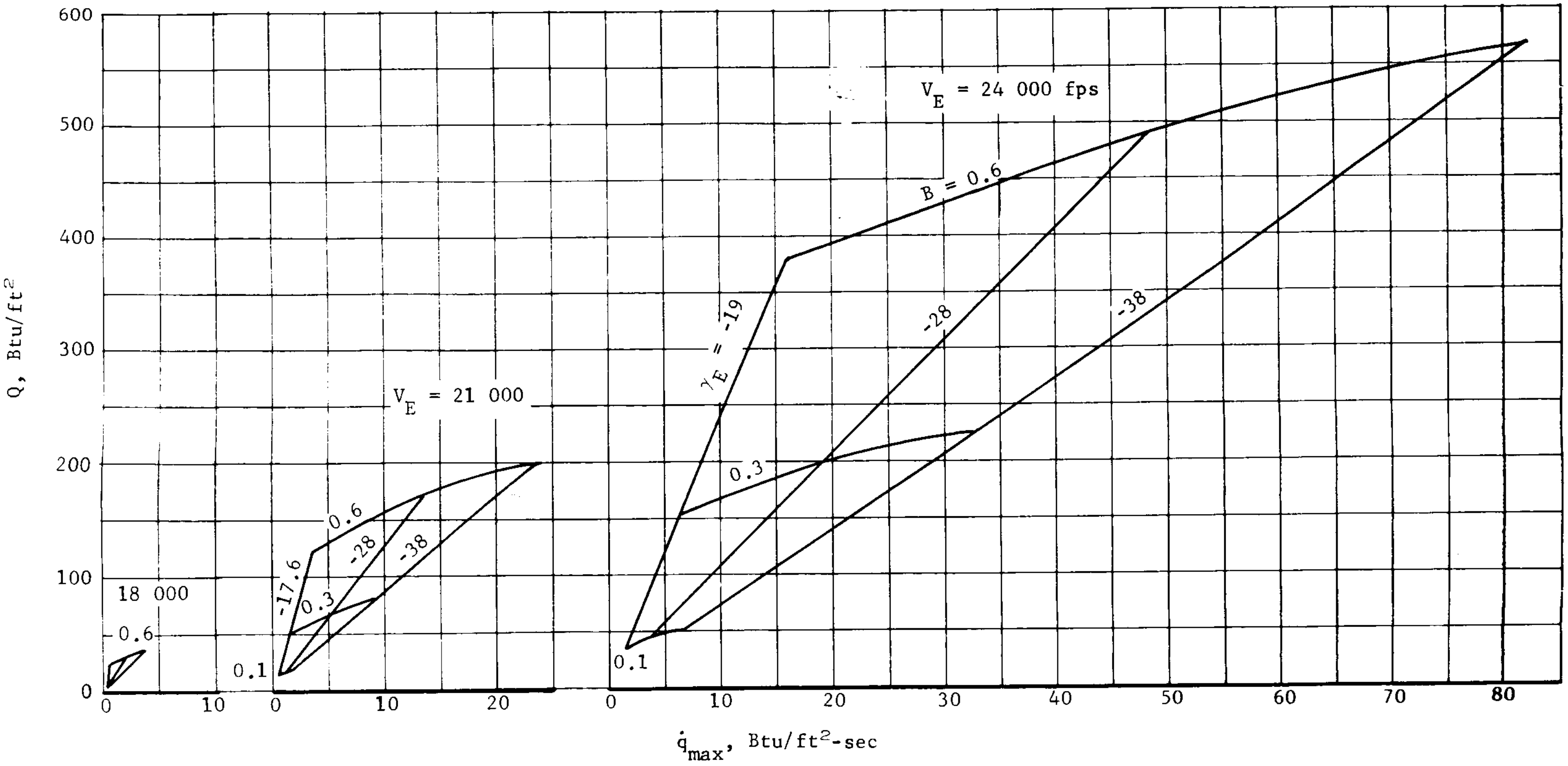

Figure C13.- Cone Edge Equilibrium Radiation Heating, VM-7, Direct Entry 70° Half-Angle Cone R_B = 7.5 ft

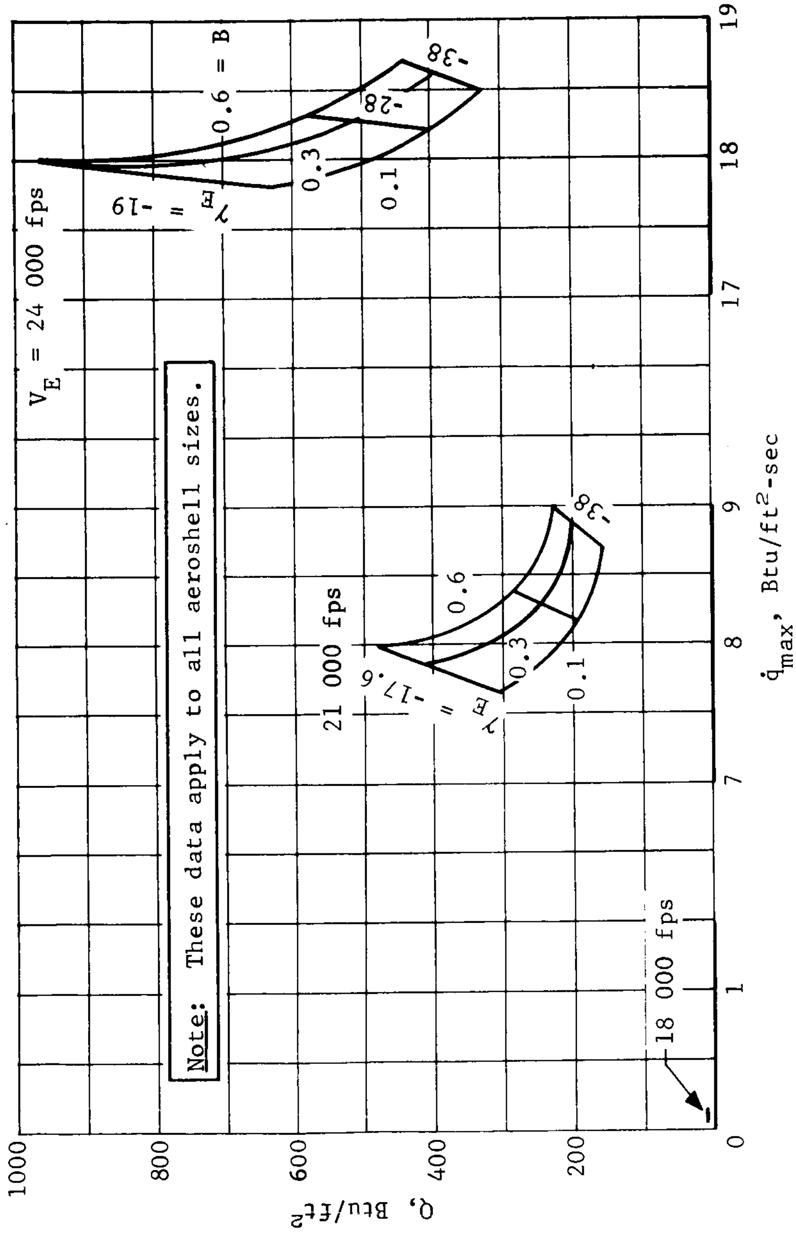

Figure C14.- Cone Edge Nonequilibrium Radiation Heating, VM-7, Direct Entry 70° Half-Angle Cone

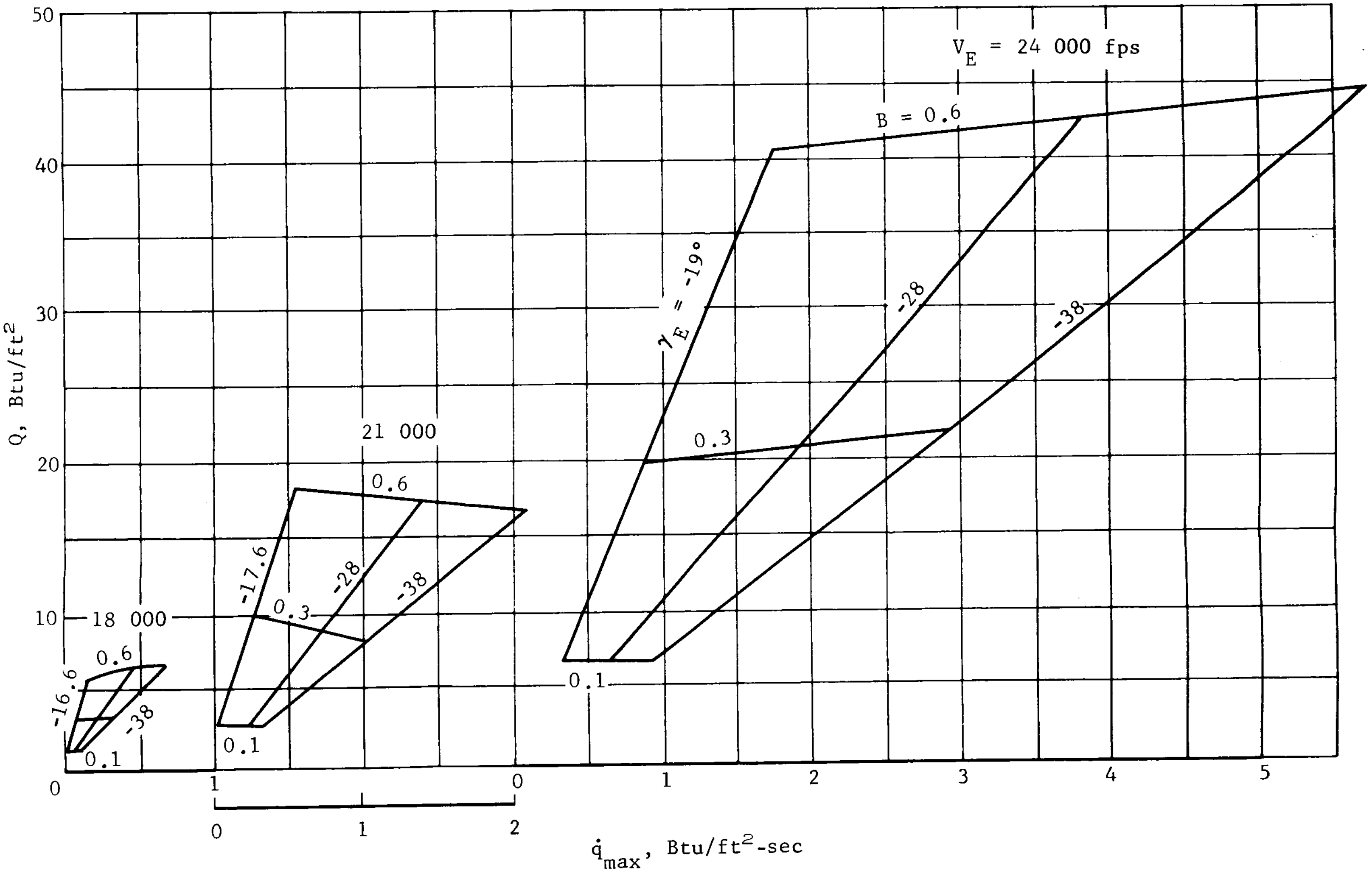

Figure C15.- Radiation Heating to Base, VM-7, Direct Entry R_B = 7.5 ft

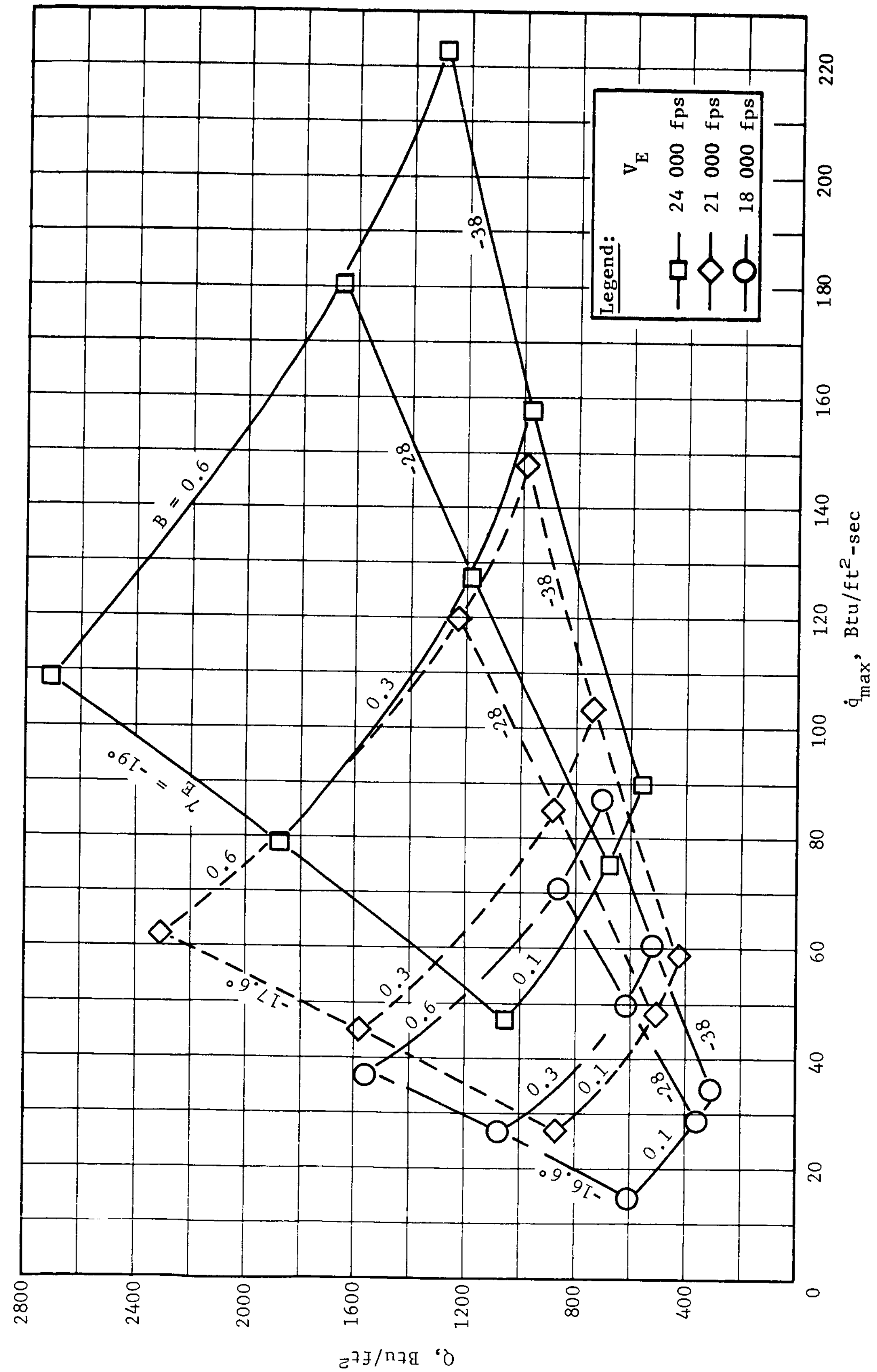

Figure C16.- Stagnation Point Convective Heating, VM-4, Direct Entry R_N = 3.75 ft

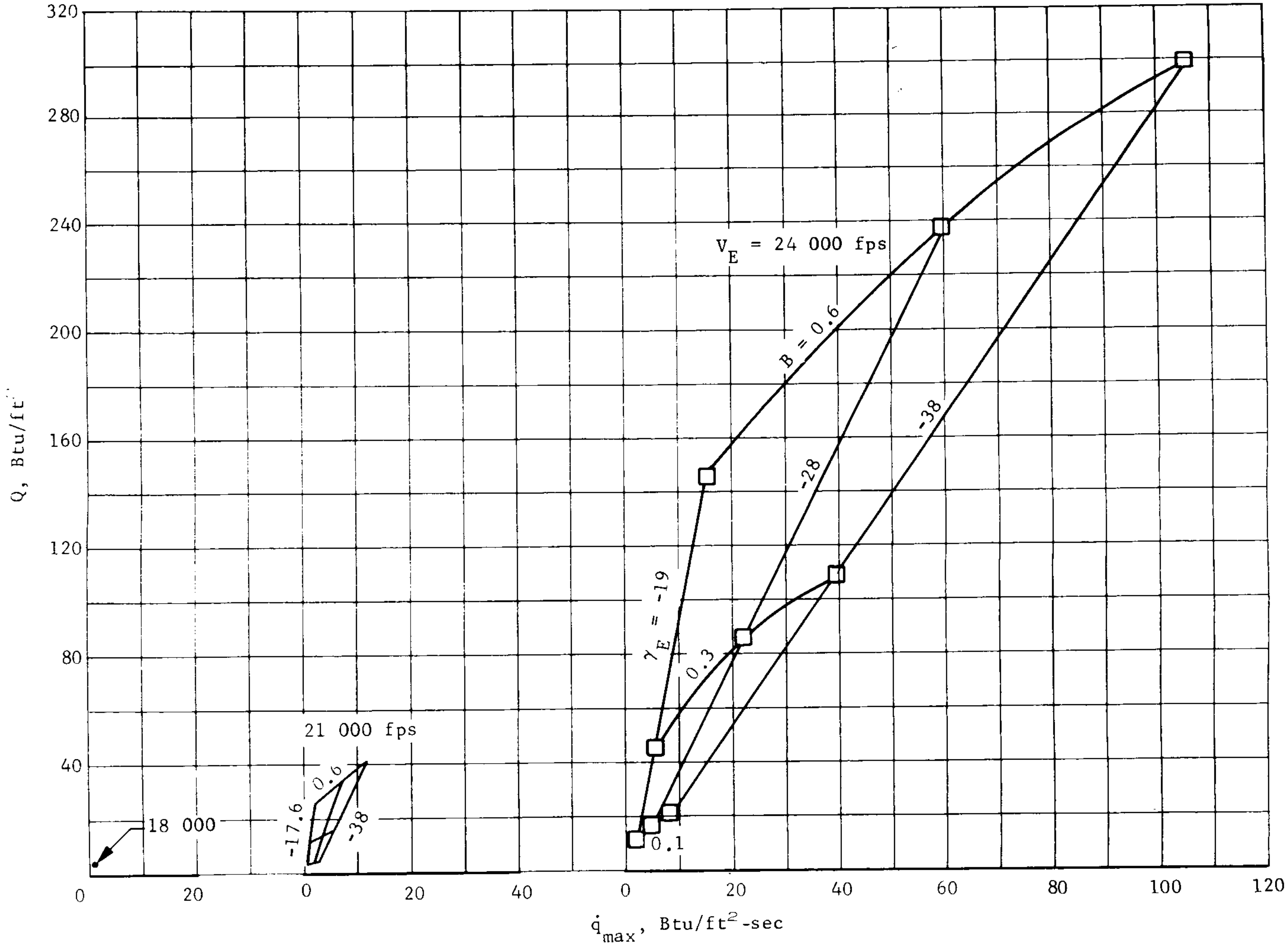

Figure C17.- Stagnation Point Equilibrium Radiation Heating, VM-4, Direct Entry R_N = 3.75 ft

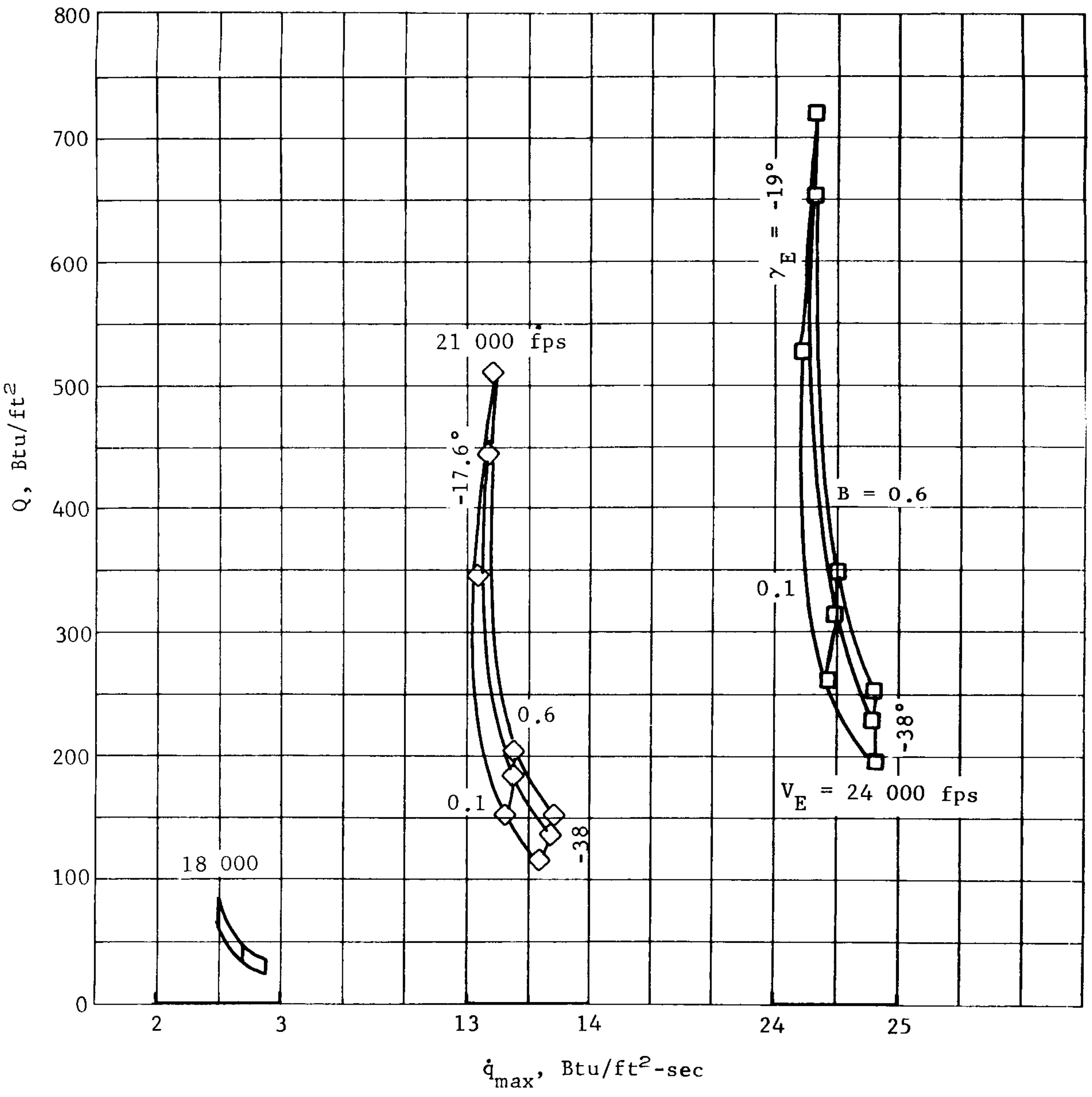

Figure C18.- Stagnation Point Nonequilibrium Radiation Heating, VM-4, Direct Entry

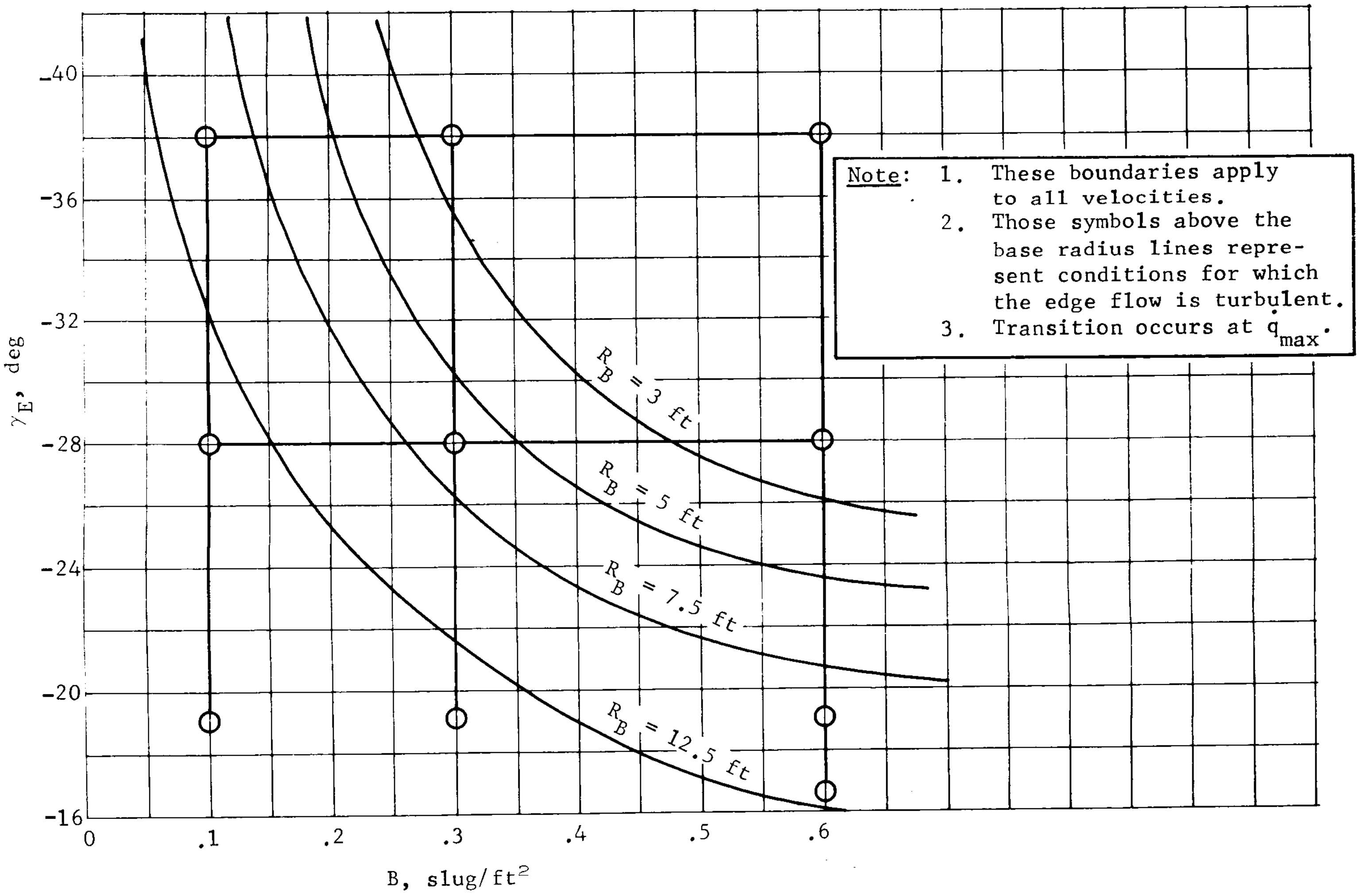

Note: 1. These boundaries apply to all velocities.
2. Those symbols above the base radius lines represent conditions for which the edge flow is turbulent.
3. Transition occurs at $\dot{q}_{max}$.

Figure C19.- Turbulent Flow Regime (Cone Edge) VM-4, Direct Entry 70° Half-Angle Cone

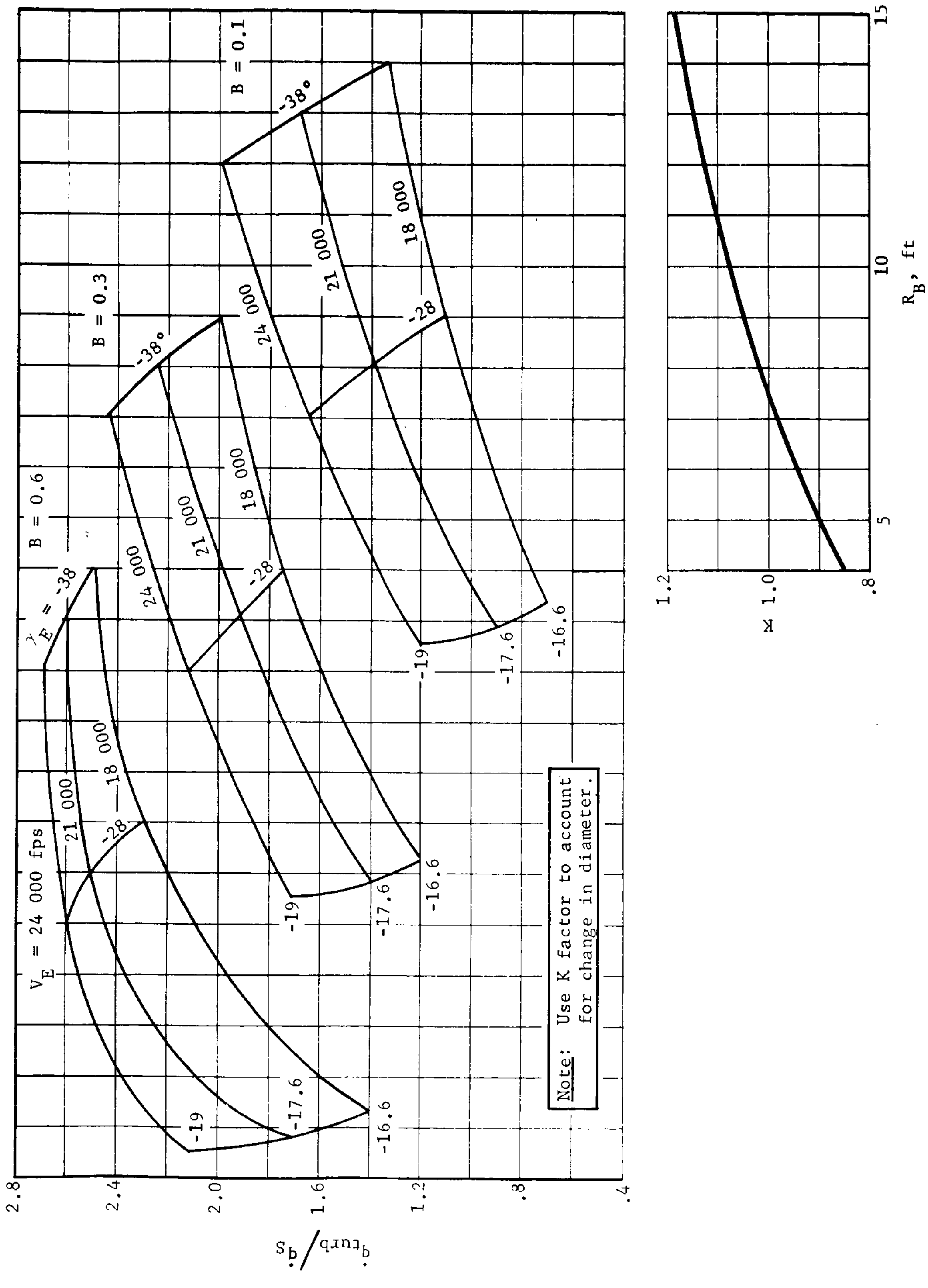

Figure C20.- Turbulent Convective Heating Ratios (Cone Edge) VM-4, Direct Entry 70° Half Angle Cone, R_B = 7.5 ft

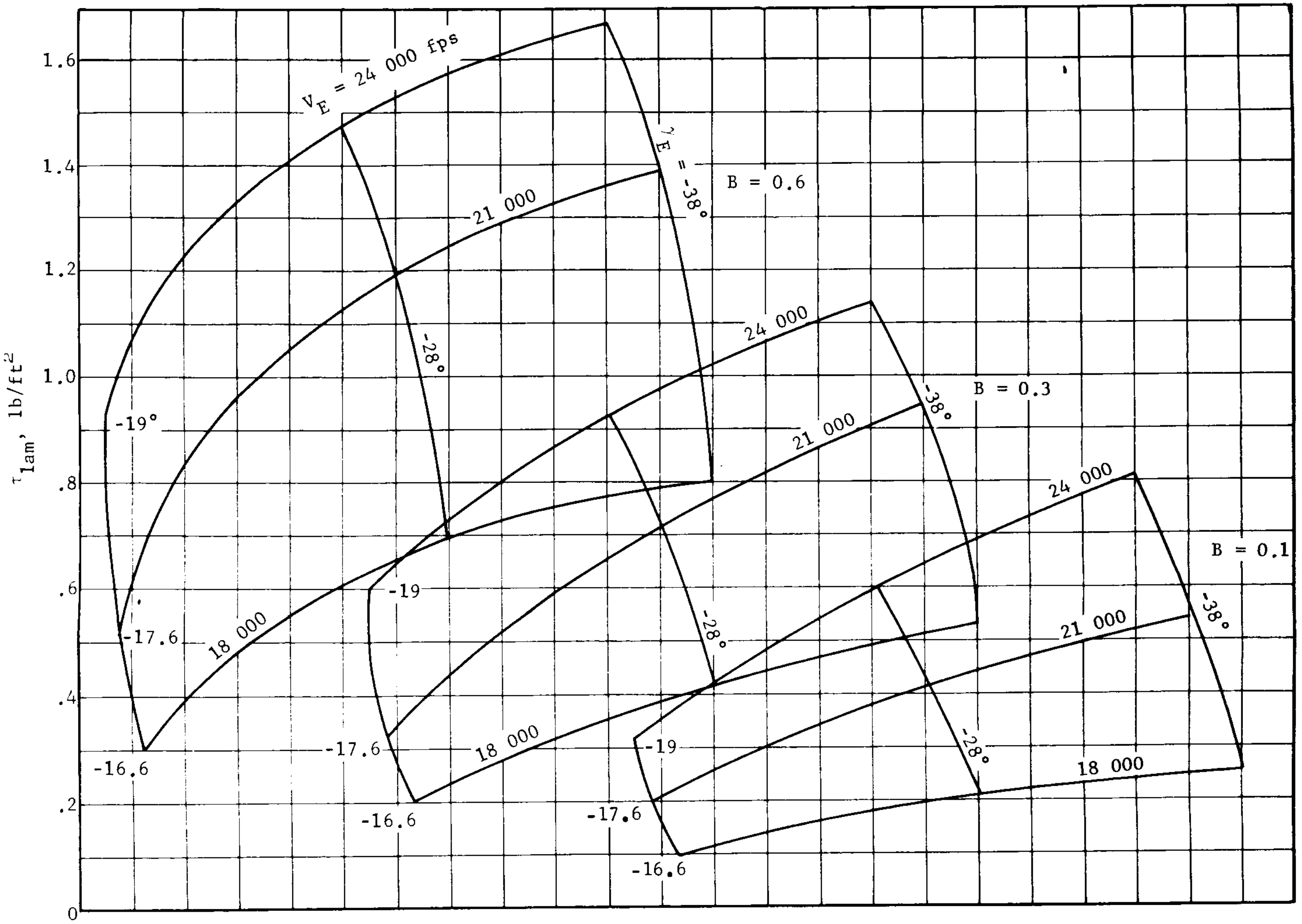

Figure C21.- Laminar Shear Stress (Cone Edge) VM-4, Direct Entry 70° Half-Angle Cone

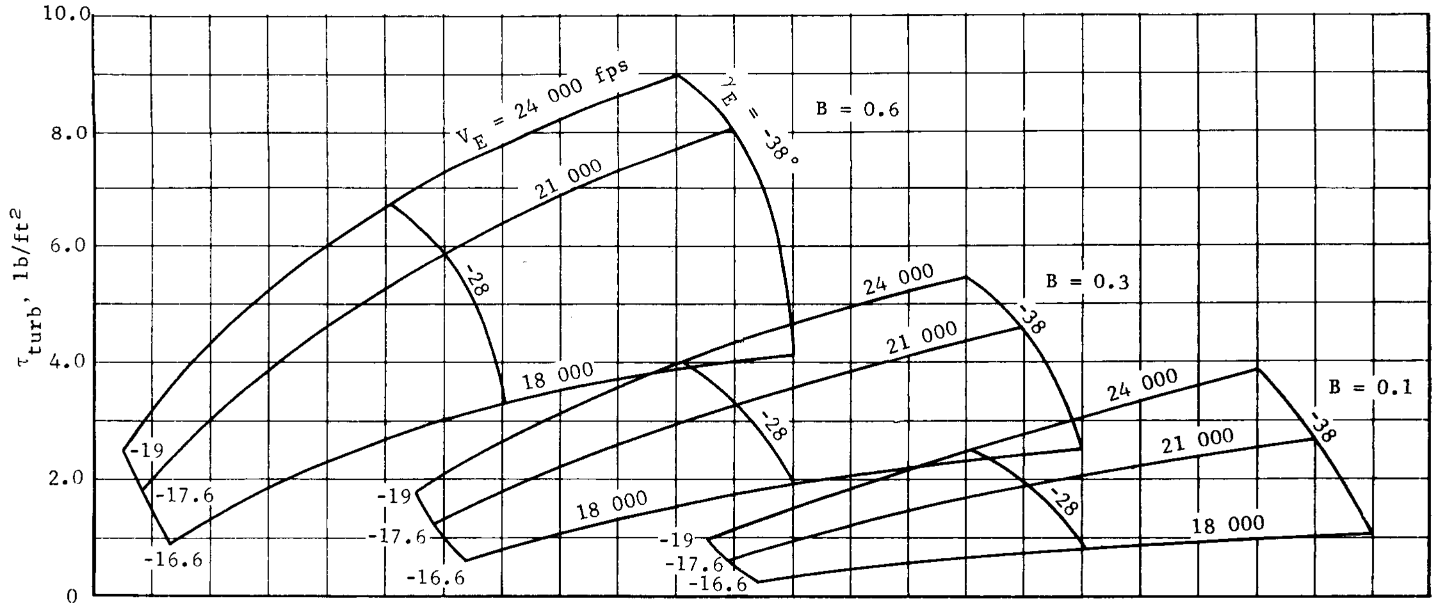

Figure C22.- Turbulent Shear Stress (Cone Edge) VM-4, Direct Entry 70° Half-Angle Cone

APPENDIX C

Equilibrium radiative heating at the edge is presented in figure C23, and nonequilibrium radiative heating is presented in figure C24.

Radiative heating to the base of the vehicle is shown in figure C25. Convective heating is estimated to be 2% of stagnation.

The analysis of the 60° cone has been limited to VM-4 because the turbulent flow regimes are expected to result in the most critical comparisons. The 60° cone was only analyzed at entry velocities of.18 000 and 21 000 fps. The conditions for which turbulence exist seem to be more velocity-dependent than for the 70° cone. Turbulent flow boundaries are presented in figure C26 for an entry velocity of 18 000 fps and in figure C27 for 21 000 fps.

Turbulent edge heating factors are given in figure C28 for the 60° cone. Vorticity interaction is expected to increase the heating over the cone significantly, and vorticity interaction factors are given in figure C28 as a function of velocity. The edge heating ratio with vorticity interaction becomes

$$\left(\dot{q}_{e_{\text{TURB}}} \Big/ \dot{q}_{s}\right)_{\text{with vort}} = \left(\dot{q}_{e_{\text{TURB}}} \Big/ \dot{q}_{s}\right) \times \text{Vorticity Factor}$$

Laminar shear stress values are presented in figure C29, and turbulent values are presented in figure C30.

Discussion of parametric data. - Parametric data are discussed in the following paragraphs.

Mission mode influence: A mission mode comparison must be tempered by the system constraints that result in different entry corridors, different size aeroshells, and different ballistic coefficients for orbital and direct modes. However, a meaningful comparison of the effect of entry mode on aeroheating can be based solely on the parametric data presented in the "Aeroheating Data" paragraph of this subsection. Aeroheating data will be presented as a function of velocity because this is a primary distinction between modes. The entry flightpath angles to be used are -17° for the orbital mode and -28° for the direct mode. These may be near nominal entry angles for the two modes, they do not represent critical design cases because these are generally the minimum and/or maximum entry angles. A ballistic coefficient of 0.3 and an aeroshell diameter of 15 ft are used for both modes. The chosen parameters represent conditions for which data are available, and no interpolation is required. This mission mode comparison is based on data for the cone edge because this is more significant to the heat shield design than is the stagnation point.

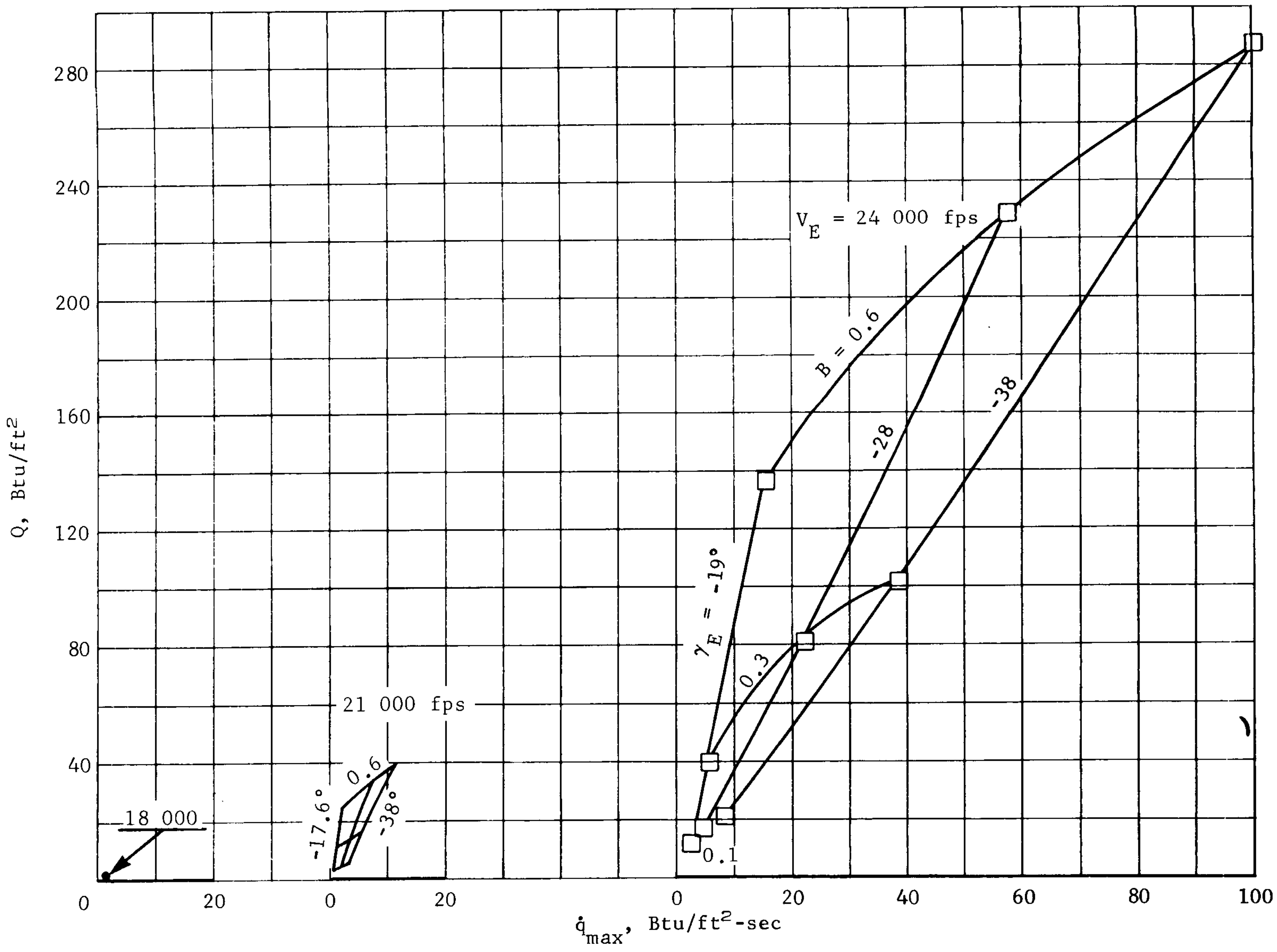

Figure C23.- Cone Edge Equilibrium Radiation Heating, VM-4, Direct Entry, 70° Half-Angle Cone, R_B = 7.5 ft

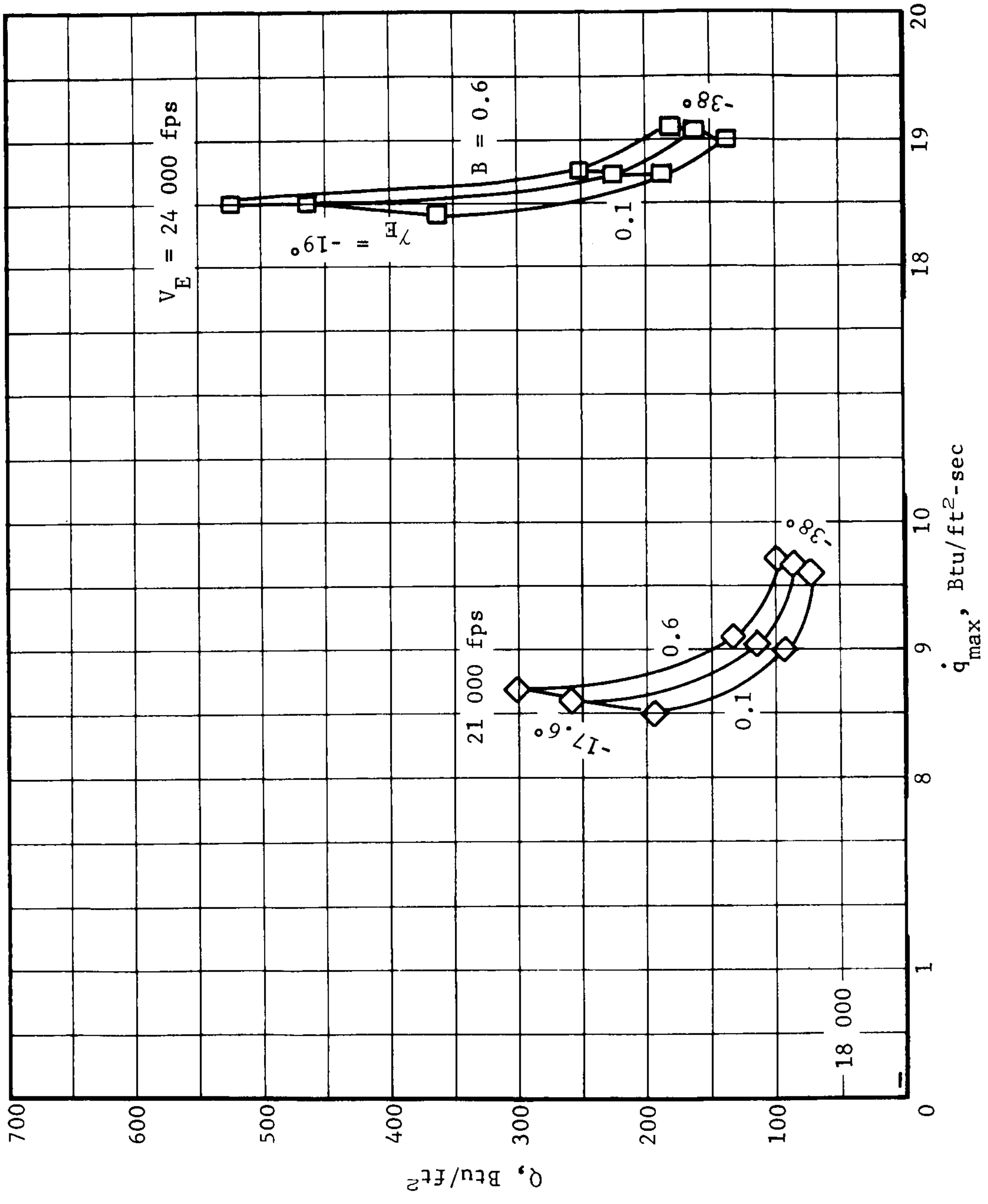

Figure C24.- Cone Edge Nonequilibrium Radiation Heating, VM-4, Direct Entry 70° Half-Angle Cone

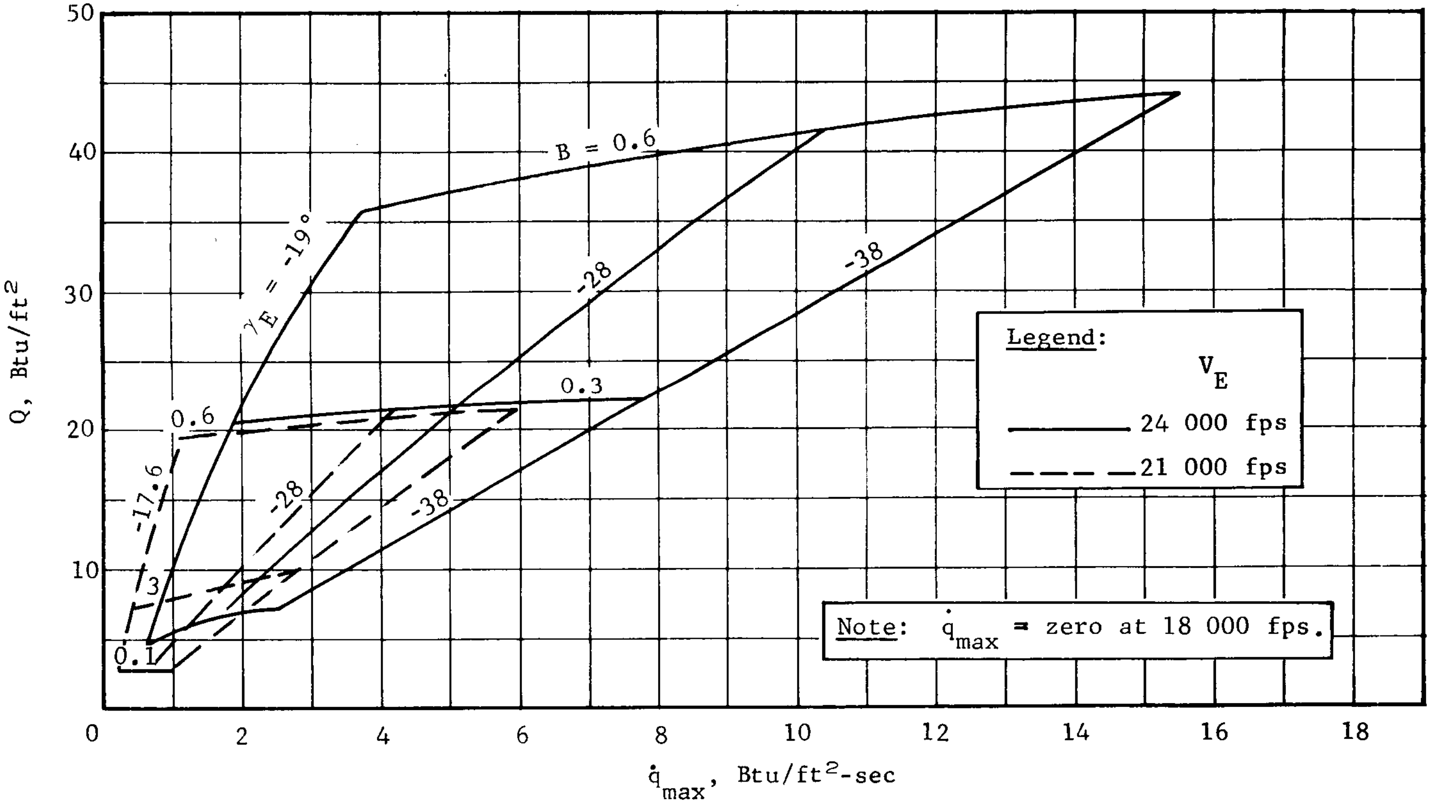

Figure C25.- Radiation Heating to Base, VM-4, Direct Entry, R_B = 7.5 ft

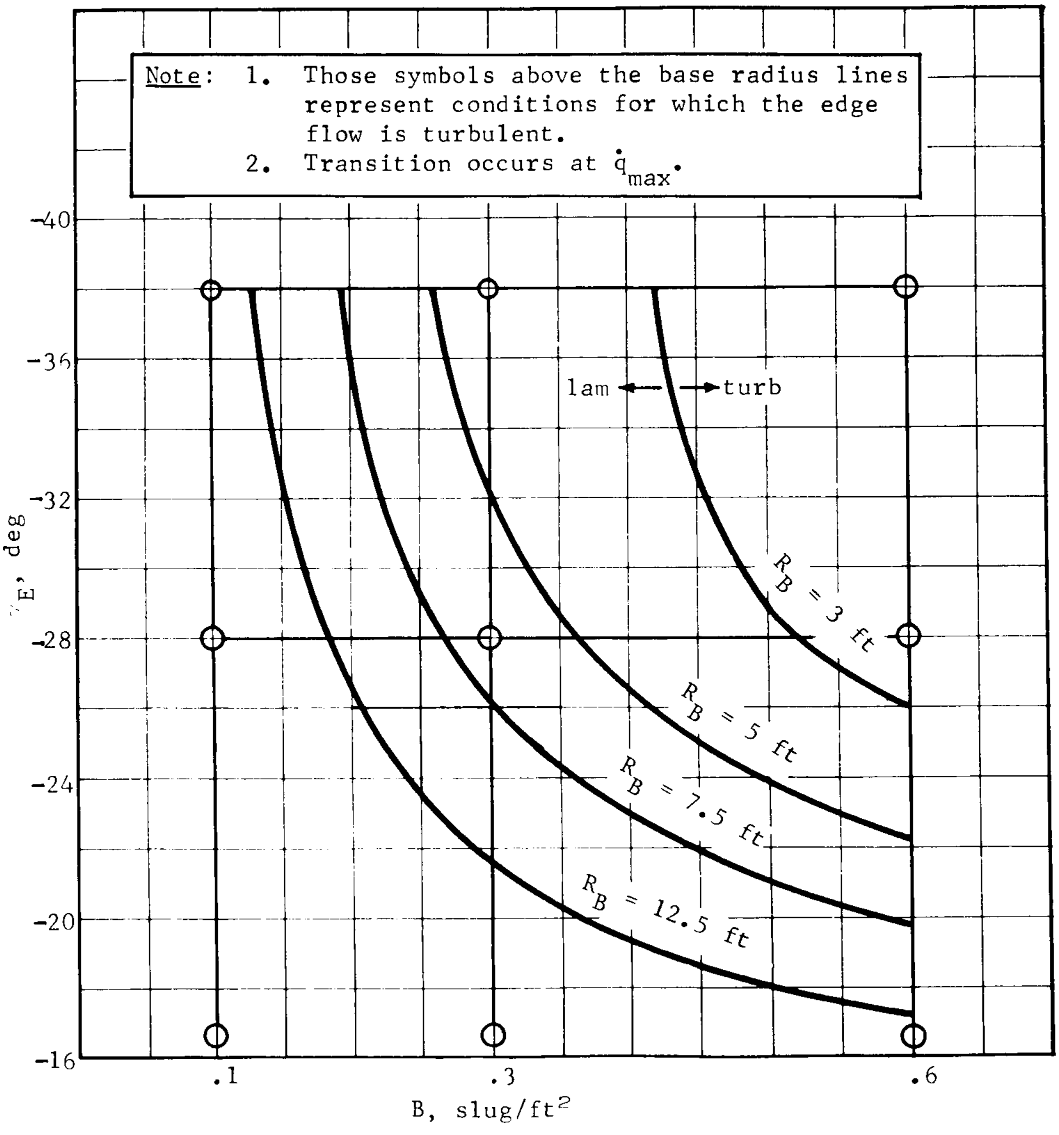

Figure C26.- Turbulent Flow Regime (Cone Edge) VM-4, Direct Entry 60° Half-Angle Cone, V_E = 18 000 fps

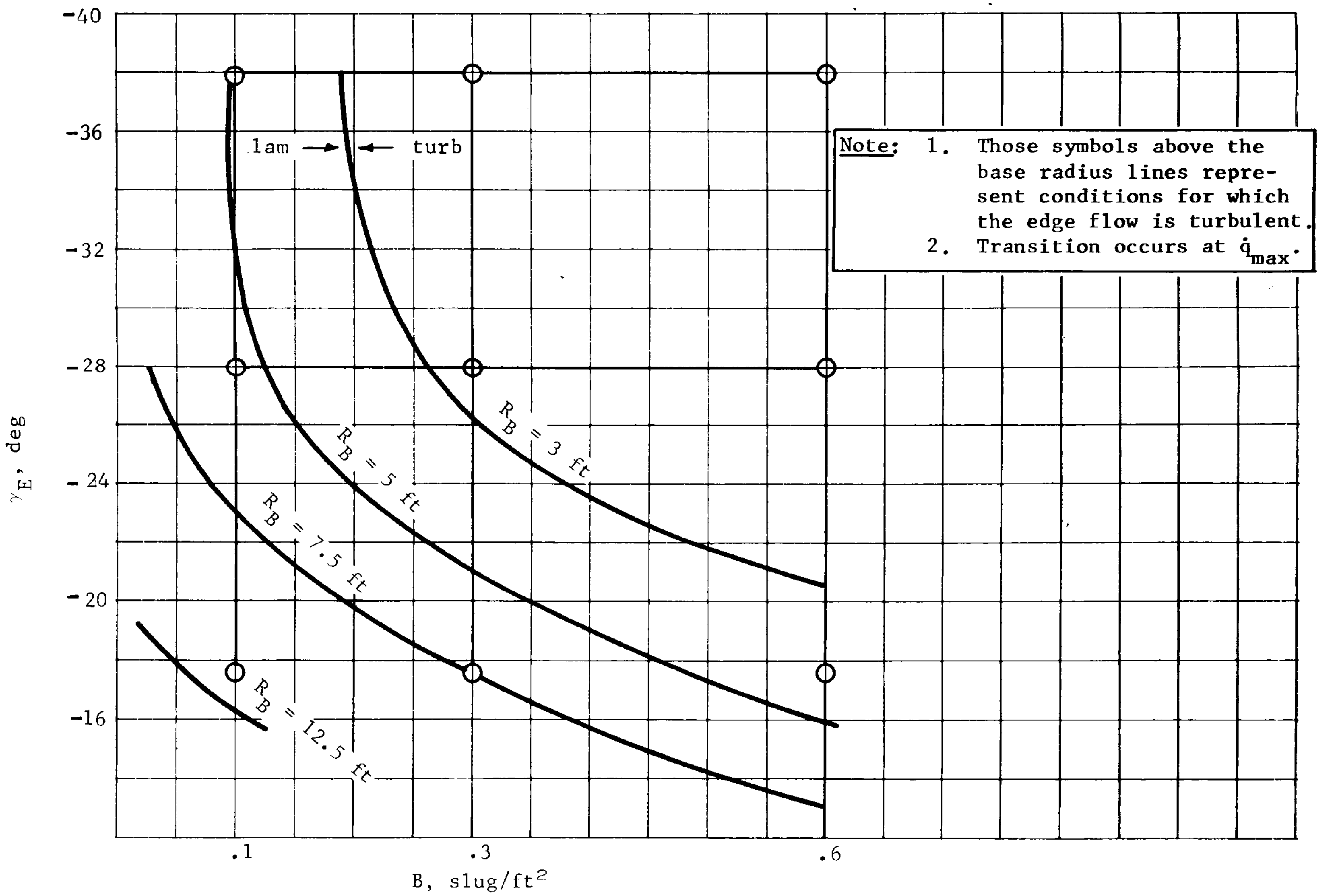

Note: 1. Those symbols above the base radius lines represent conditions for which the edge flow is turbulent.
2. Transition occurs at $\dot{q}_{max}$.

Figure C27.- Turbulent Flow Regime (Cone Edge) VM-4, Direct Entry 60° Half-Angle Cone, V_E = 21 000 fps

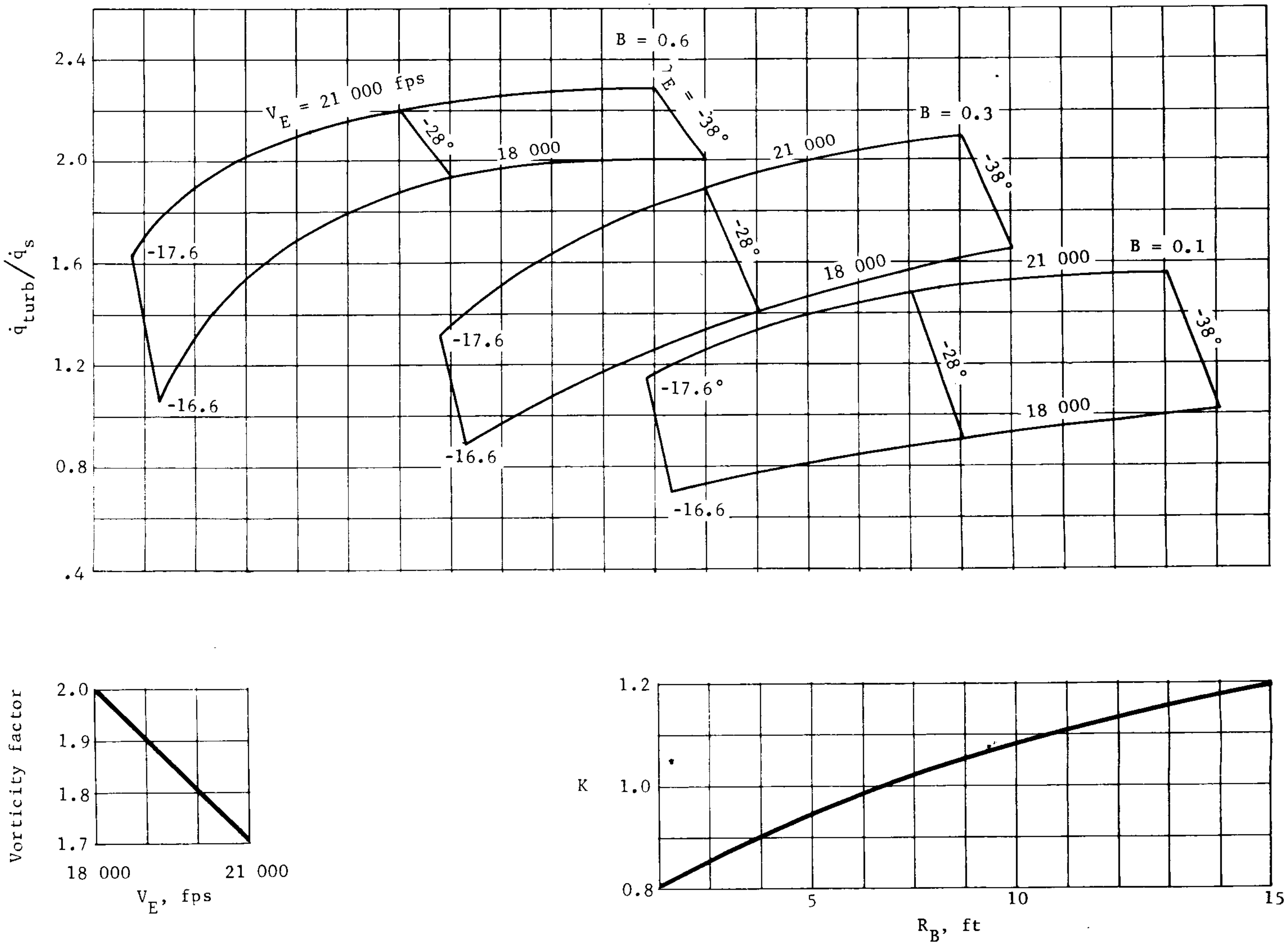

Figure C28.- Turbulent Convective Heating Ratios (Cone Edge) VM-4, Direct Entry 60° Half-Angle Cone, R_B = 7.5 ft

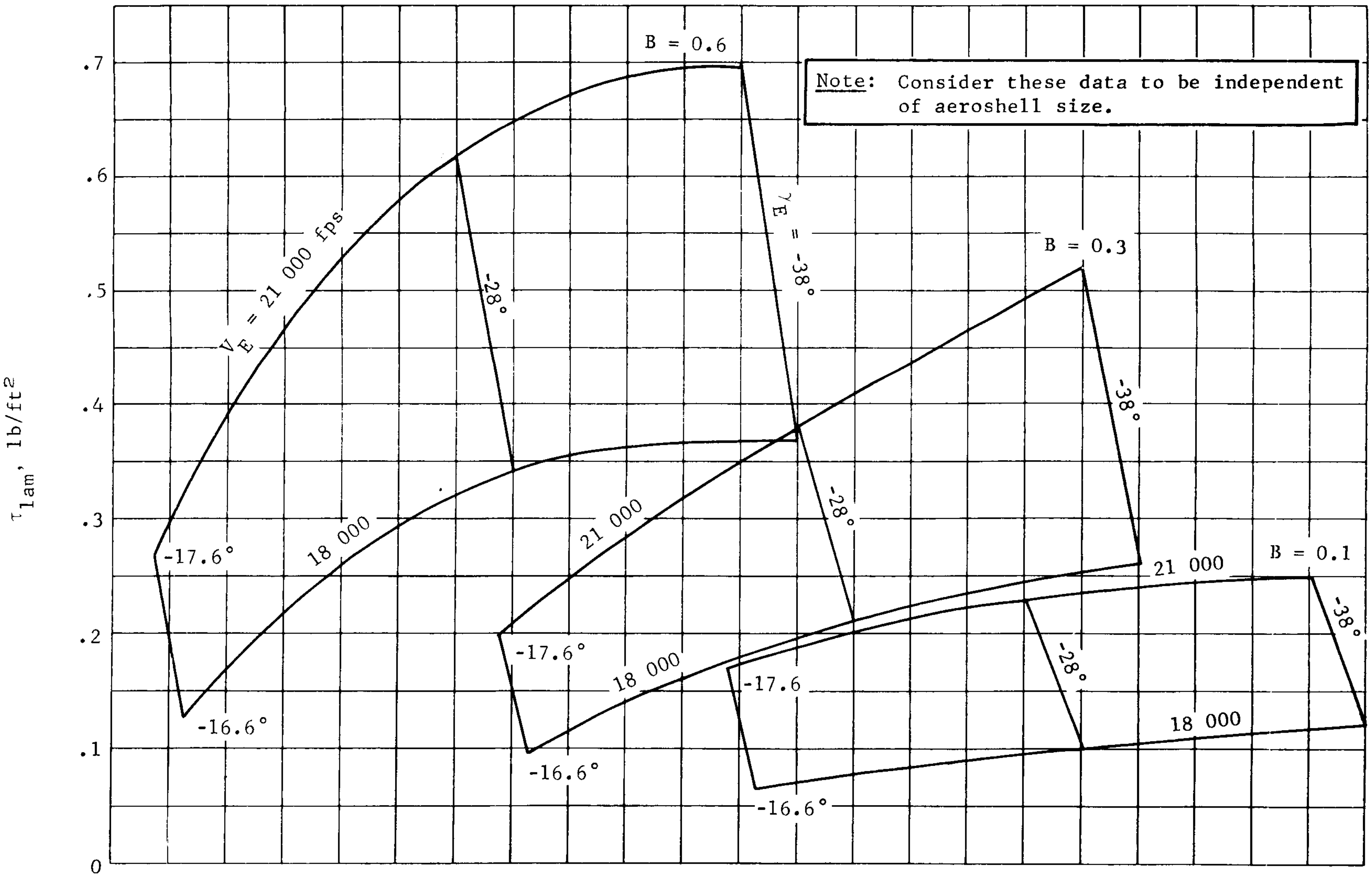

Figure C29.- Laminar Shear Stress (Cone Edge) VM-4, Direct Entry 60° Half-Angle Cone

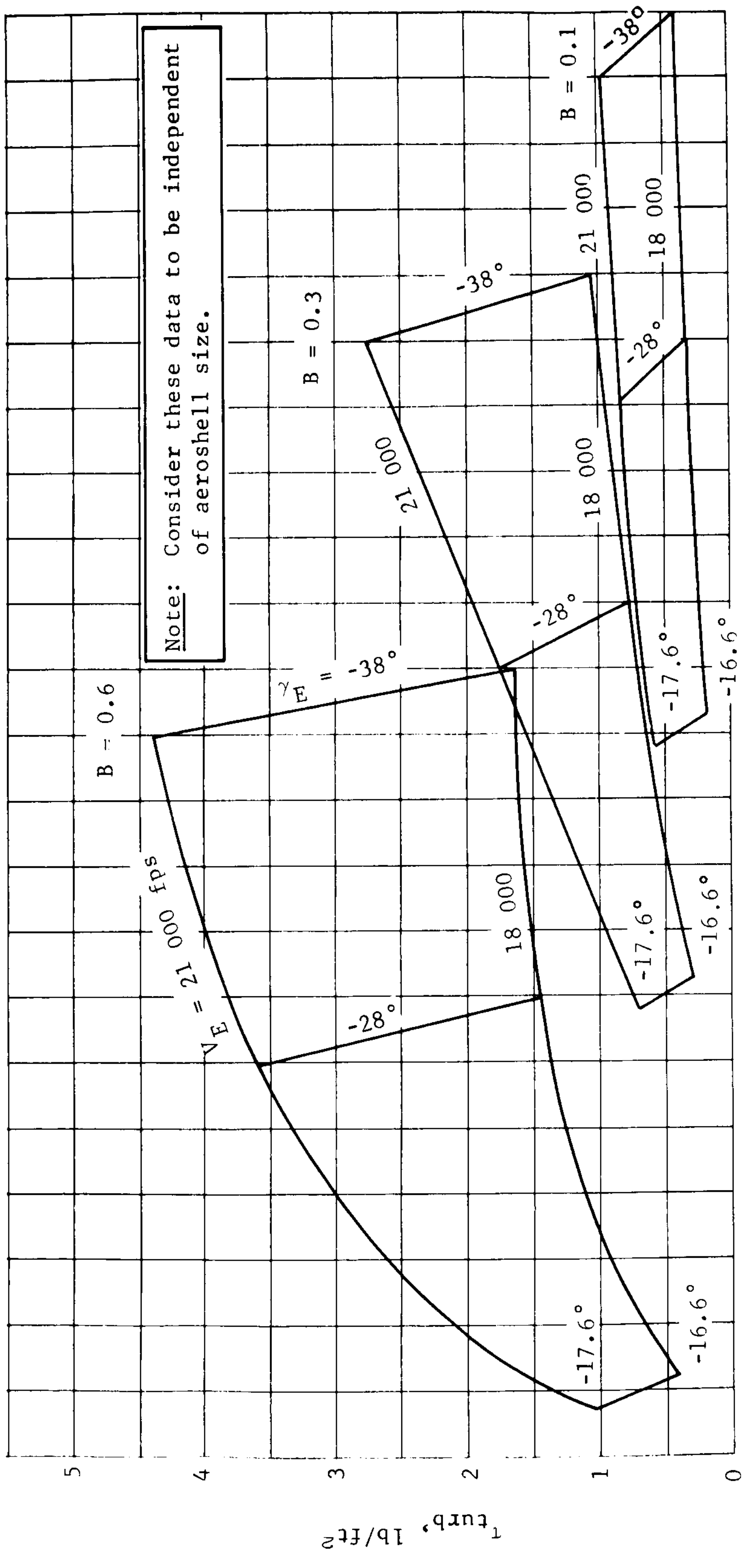
Note: Consider these data to be independent of aeroshell size.

Figure C30.- Turbulent Shear Stress (Cone Edge) VM-4, Direct Entry 60° Half-Angle Cone

Maximum heating rate data for the selected conditions are presented in figure C31. Laminar convective heating rate exhibits a steady increase with velocity and discontinuity between modes because of difference in entry flightpath angle. The direct mode laminar heating rate at 18 000 fps is twice that of the orbital mode and is 4 times as great at 21 000 fps. However, the turbulent convective heating rate in VM-4 is four times as great as the laminar. The turbulent heating rate can be high enough to require the use of a more dense ablator with a resulting greater heat shield weight (see Section 2 of this appendix). Maximum radiative heating rate is insignificant at the lowest direct entry velocities but can be dominant at the highest direct mode velocities. In fact, when the uncertainty factors of the "Definition of Parameters in Study" paragraph of this subsection are applied the combination of radiative and laminar convective heating at high velocities can also require a change in ablator material.

Total heating load data are presented in figure C32. Here the laminar convective data show a decrease from the orbit to the direct mode because of the differences in entry flightpath angle. The largest laminar heating loads occur in VM-7 for both modes. However, turbulent heating in VM-4 is dominant for the direct case. The differences in magnitude between orbital and direct modes are less pronounced for total heating, which determines ablator thickness, than they are for heating rate. Radiation heating loads are insignificant at the lowest direct entry velocities but are of major importance at the highest velocities. Maximum laminar heating loads are associated with minimum flightpath angles because of the long flight times involved. Therefore, data are also shown in figure C32 for the minimum entry angles from figure C1 in the VM-7 atmosphere. When the total radiative and convective loads are considered, it is not apparent whether VM-7 or VM-4 is the more critical heat shield design case. This implies that the influence of turbulent heating on heat shield design may result more from consideration of maximum heating rate than from total heating load.

Two significant factors arise from an inspection of figures C31 and C32. Radiative heating and turbulent convective heating can exert strong influences on heat shield design for the direct mode. The influence of radiative heating is further complicated by the uncertainty in current estimates. This problem can be largely eliminated by restricting entry velocities to less than 20 000 fps. Transition to turbulence is a function of entry conditions, primarily entry angle, and of configuration, i.e., ballistic coefficient and diameter.

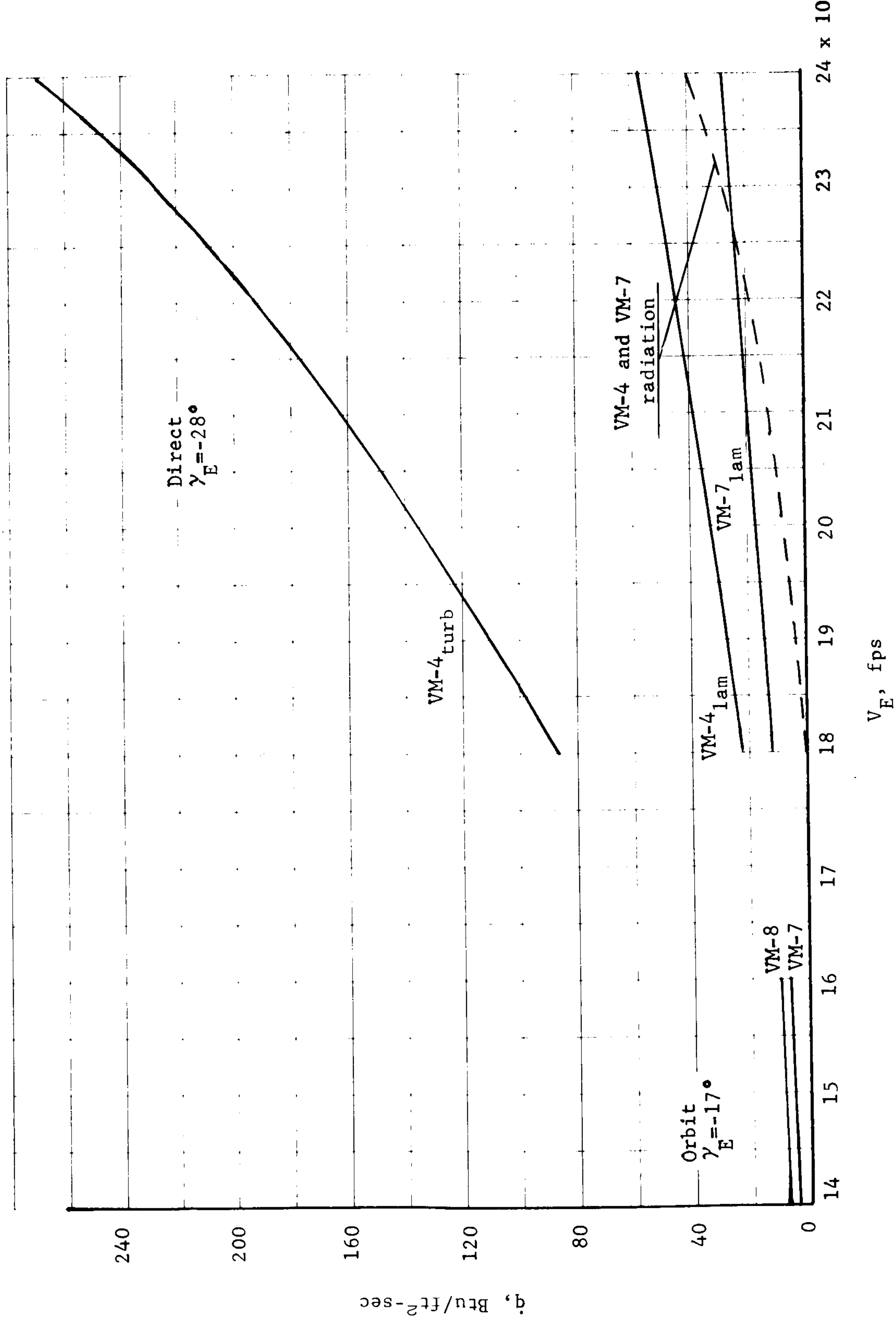

Figure C31.- Mission Mode Maximum Heating Rate Comparison, B = 0.30, Diameter = 15 ft

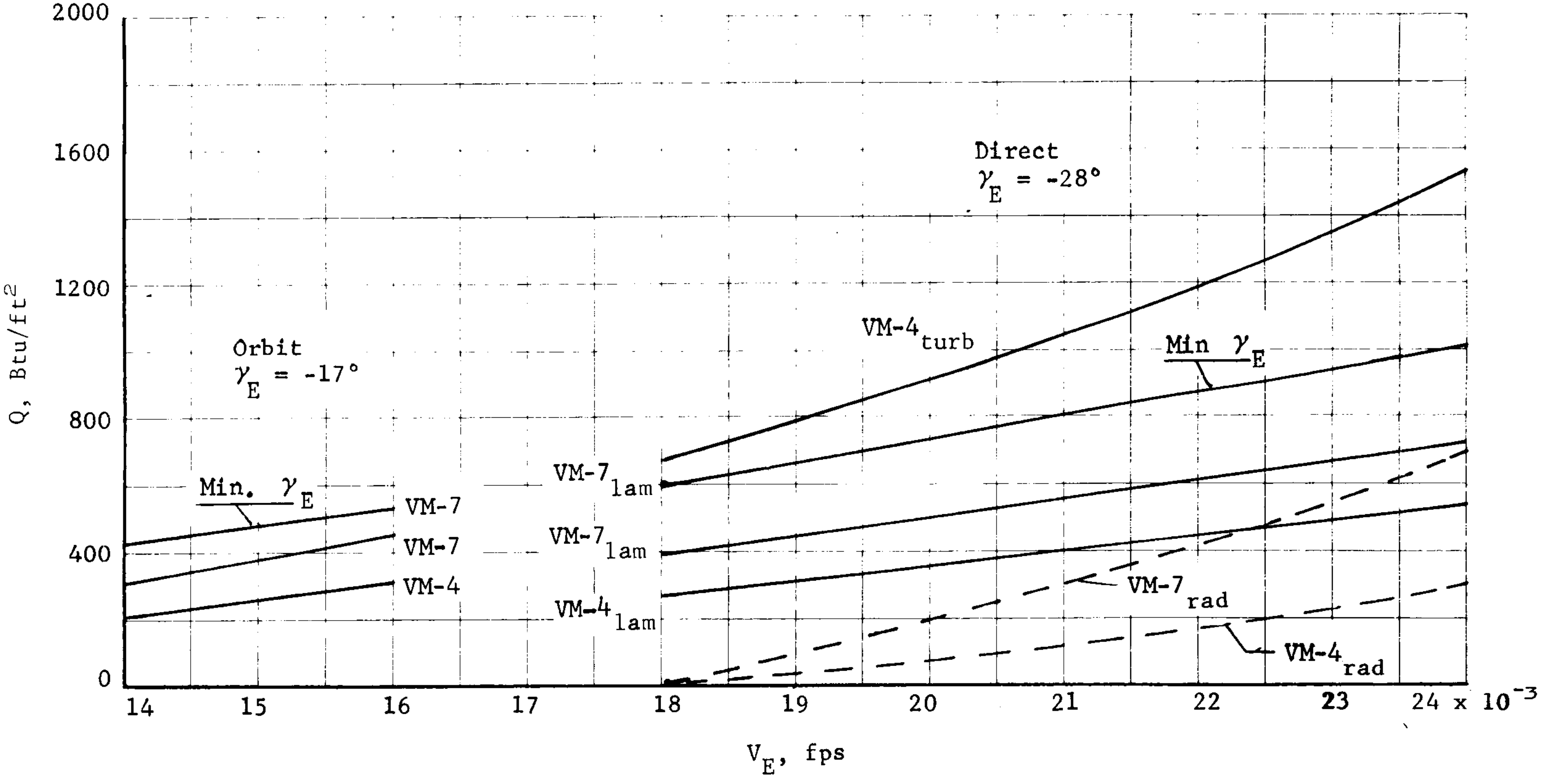

Figure C32.- Mission Mode Total Heating Load Comparison, B = 0.30, Diameter = 15 ft

An inspection of figure C19 shows that there are combinations of these parameters for which turbulence does not exist. However, it is unlikely that both the entry corridor and configuration can be so constrained as to avoid turbulence. The turbulence problem is further complicated by the lack of confidence in the flow transition criteria. Thus, the estimates of aerodynamic heating for the direct mode are characterized by two important uncertainties that require conservatism in current estimates and can have significant influences on ablator weight requirements. The direct mission mode will require a more complex and costly experimental program to adequately define the aerodynamic heating than will the orbital mode.

Aerodynamic heating to the base is expected to be of a low level. However, differences in base heating between modes are similar to the differences in forebody heating. The base convective heating is twice as great at the lowest direct entry velocities as at orbital entry velocities. The convective heating to the base increases as entry velocity increases and radiative heating may be significant at the higher direct entry velocities. The estimated heating must be protected against, even though it is of a low level. The large difference in relative magnitudes of base heating for the orbital and direct entry modes may require different forms of base heat protection.

Direct mode configuration influence: A simple comparison of the aeroheating for the 60 and 70° cones can be based on the normalized heating distributions of figure C2 when the aeroshell diameter is fixed. It appears that the total heat load to the 60° cone is greater than that to the 70° cone even for this comparison with no vorticity interaction. The vorticity interaction factor shown in figure C28 may be conservative for this nose bluntness ratio but it is clear that any vorticity interaction results in a definitely greater heating load to the 60° cone. This sort of comparison is valid at low direct mode velocities where radiation heating is not large. Radiation heating to the 60° cone is always less than to the 70° cone, and this fact could become predominant in the comparison of heating at the higher direct mode velocities.

Aeroshell structural weight comparisons based on the data of section 3 of this appendix were made for a ballistic coefficient of 0.35. The diameters of the 60 and 70° cones were varied so that entry weight remained constant (see tabulation).

Cone angle, deg	70	60	70	60
Base diameter, in.	120	124.8	180	187.2
Aeroshell weight, lb	127	119	368	330

The 60° cone exhibits slightly lower structural weights for given conditions than does the 70° cone. This will be compensated for in some degree by increased booster shroud diameter to accommodate the increased 60° cone aeroshell diameter.

More detailed analysis is required to establish the optimum aeroshell configuration for the direct mode. This cursory analysis of the configuration influence indicates that significant differences do not exist between the 60 and 70° cones and that a valid mission mode comparison can be made using the 70° half-angle cone.

Analysis Techniques

A point mass trajectory with a constant ballistic coefficient was used to determine the trajectory parameters required to predict the heating environment. The perfect gas law and the hydrostatic equations were used with the VM atmospheric data to determine atmospheric properties at each calculation point. The atmospheric viscosity was calculated using Sutherland's equation with modification for atmospheric composition variation according to data prepared by the National Bureau of Standards.

Equilibrium thermodynamic properties were obtained for the desired atmospheric compositions with the JPL thermochemistry and normal shock computer program (ref. C4) and from correlations with the data of reference C5 for the transport properties. The viscosity was correlated with the data of references C6 and C7. It was assumed that the properties of the shock layer in the stagnation point regions were identical with the properties behind a normal, equilibrium shock wave.

The stagnation point convective heating rate was calculated using the data for variable gas composition of Marvin and Pope (ref. C8). Interpolation between tabular values was used to obtain the necessary constants for gas mixtures not included in reference C8.

APPENDIX C

The stagnation point equilibrium radiation heating rate including the effect of self-absorption of CO(4+) was determined using experimental data and the correlations of references C9 thru C13. A combination of the program described in reference C4 and the techniques of Kivel and Baily (ref. C14) and French (ref. C15) was used to predict the radiation intensities for arbitrary gas mixtures. The data for VM-8 are presented in reference C13, while data for VM-4 and VM-7 are presented in figures C33 and C34.

The nonequilibrium radiation heating rate is presented in figure C35 as a function of velocity. This curve is based on the experimental data and correlations of references C16 and C17. The data of reference C17 and recent results from the Martin Marietta Corporation shock tube indicate that the CN nonequilibrium radiation component is not significant for orbital entry. The assumption was made that the nonequilibrium radiation started at an altitude where the density and energy were sufficient to sustain it. A possible significant source of nonequilibrium radiation for the orbit mode is the CO_2 vibration-rotation component. This is discussed in reference C2, but is not considered in this study because its magnitude is uncertain and its inclusion might distort the study results. This source of radiation needs to be investigated experimentally so that its importance can be evaluated.

Pressure distributions were obtained through the use of applicable theory. The pressure distribution for a 60° half-angle cone can be approximated by Newtonian theory for a shock density ratio of 0.05 while a 70° half-angle cone pressure distribution can be predicted by the single strip integral method. These pressure distributions were used with the reference enthalpy method to predict the laminar and turbulent convective heating rate distributions and the laminar and turbulent shear stress values. Correlations of turbulent heating parameters from the reference enthalpy heating program were used to provide estimates for the wide range of conditions of this study. The transition from laminar to turbulent flow was assumed to occur when the momentum thickness Reynolds' number (refs. C18 thru C20) reached a value of 250. This value is based on the data of reference C21. It was assumed for this study that transition occurred over the entire cone surface simulataneously. Previous studies have shown this assumption to be reasonable when the variation of the transition criterion with local Mach number is considered.

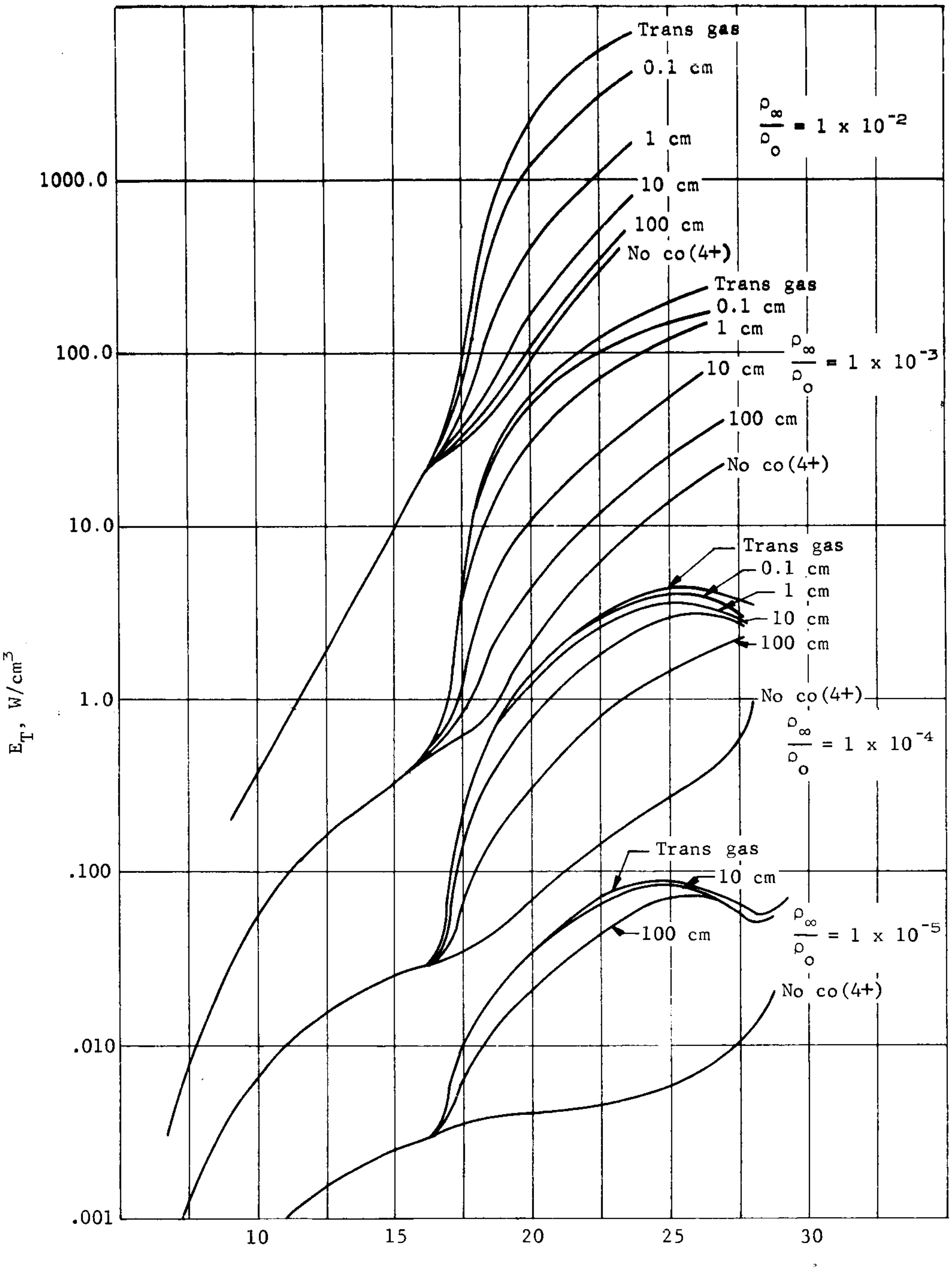

Figure C33.- Radiation Intensity, 68% CO_2 - 32% A (VM-4)

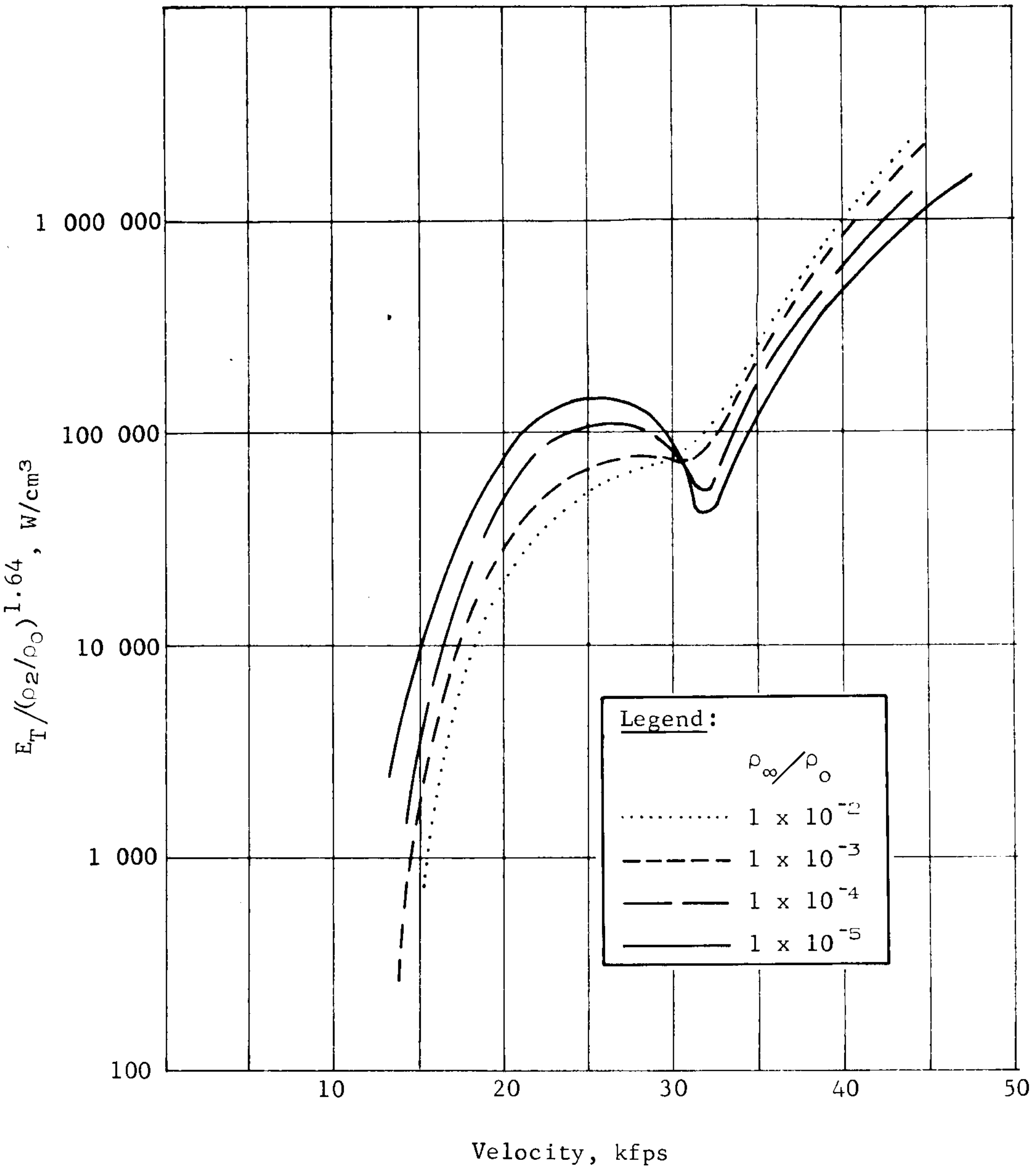

Figure C34.- Radiation Intensity, 20% CO_2 - 80% N_2 (VM-7)

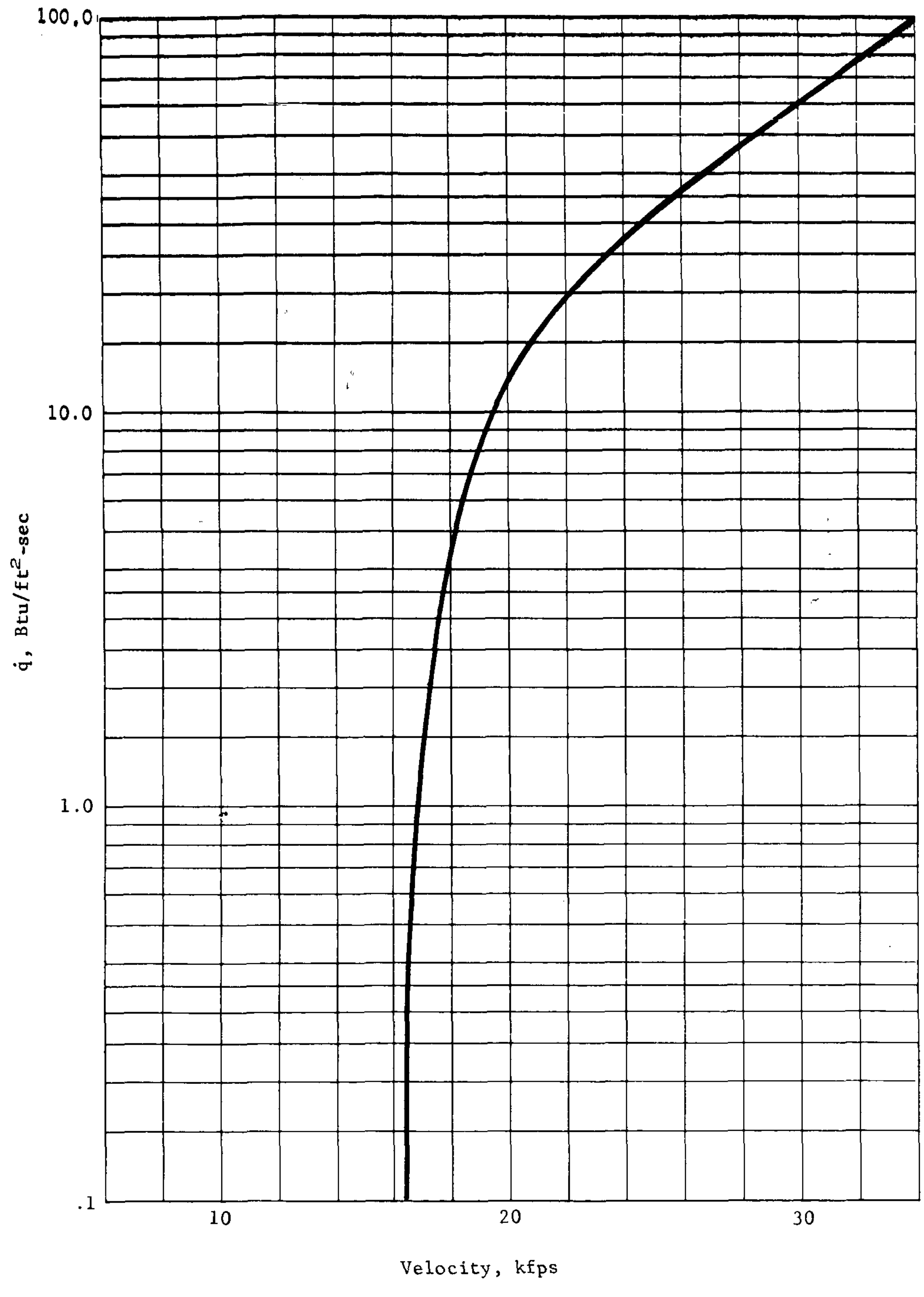

Figure C35.- VM-4 and VM-7 Nonequilibrium Radiation

APPENDIX C

The radiation components at the cone edge, equilibrium, nonequilibrium, and entropy layer radiation, were calculated in a manner similar to the stagnation point calculations. The radiation calculations include the effect of self-absorption of CO(4+) when applicable.

The effect of vorticity interaction on the edge convective heating rate was included for the 60° half-angle cone because the turbulent boundary layer thickness becomes a significant part of the entropy layer thickness. Calculations indicate that the turbulent boundary layer thickness can be one-tenth to one-half of the entropy layer thickness. A conservative approach was assumed for the vorticity interaction effect. The approach was to determine the sharp cone solution and use it as a limiting case. The problem of vorticity interaction does not exist for a 70° half-angle cone because the entire shock layer is an entropy layer. Appropriate factors were determined for the 60° half-angle cone as a function of velocity in the region of interest.

The convective base heating rate was estimated to be 2% of the stagnation point value for the configuration of this study. This figure was based on data correlation of references C22 thru C24 and preliminary data from the Martin Marietta Corporation hot-shot wind tunnel. Radiation heating to the base was estimated on the basis of the experimental data of reference C25.

APPENDIX C

2. HEAT SHIELD

Ablator Material Selection and Design Criteria

For this study, the aeroshell has been considered to be protected from the entry environment with an ablative heat shield system. It is possible that in an actual design, local areas would use nonablative materials or special materials formulated for specific applications such as antenna windows or instrumentation ports. These local areas will have little effect on the total system weight and, therefore, have been omitted in this study. The basic ablative material considered is the SLA-561 low-density cork, elastomeric silicone-based material. This material has been under development by Martin Marietta over the past three years and is formulated specifically for the Mars mission. The material retains its elastomeric properties to -150°F and, therefore, minimizes cold soak and other thermal strains. It can be molded directly over and bonded to large areoshells and, thus, presents no major fabrication problems or strain incompatibilities in conforming to the substructure. Material samples have been exposed to sterilization cycles and vacuum without any apparent degradation. This material is efficient thermally, approximating the performance of corkboard, but possesses a much stronger and tenacious char layer than cork. The development and performance of this material is documented in reference C27.

The SLA-561 has been tested in the plasma arc extensively up to heating rates of 100 Btu/ft^2 sec, which is well beyond the requirements for out-of-orbit entries and covers most of the direct entry cases. The recession mechanism is primarily by melting and vaporization and increases quite rapidly at heating rates greater than 100 Btu/ft^2 sec. Therefore, for this study, the use of the SLA-561 material was limited to regions with heating rates less than 100 Btu/ft^2 sec. This limitation was imposed at this time primarily because of lack of experimental data at higher heating rates and an adequate analytical model at higher heating rates. The thermal properties of SLA-561 are listed in table C1.

High heating rates result from the turbulent flow on the aft regions of aeroshell for the direct entry mode. In these regions, where the heating rate exceeds 100 Btu/ft^2 sec, the ESA-5500M material was used. This material is a modification of the leading edge material used on the Precision Recovery Including Maneuvering Entry (PRIME) lifting body flight test vehicle and is currently being studied for the high-heating rate, high-shear environment associated with Venus entry. This material has been formulated for shear levels approximately 20 times the Mars conditions. Its thermal properties are given in table C2.

APPENDIX C

TABLE C1.- MATERIAL PROPERTIES OF SLA-561

Ablator material conductivity, Btu/in.-sec-°R

$\lambda = 0$ (char)		$\lambda = 0.75$	
1.5×10^{-6}	at 0°R	0.8×10^{-6}	at 0°R
1.5×10^{-6}	at 1500°R	0.8×10^{-6}	at 1500°R
4.0×10^{-6}	at 2400°F	2.3×10^{-6}	at 2400°R

$\lambda = 1.0$ (virgin plastic)	
0.695×10^{-6}	at 0°R
0.695×10^{-6}	at 560°R
0.7×10^{-6}	at 3200°R

(Linear interpolation between lambda and temperature points)

Pyrolysis gas specific heat: 0.60 Btu/lb-°F (constant with temperature)

Char density: 8.25 lb/cu ft

Virgin material density: 14.7 lb/cu ft

Virgin material specific heat: 0.30 Btu/lb-°F

Virgin material heat of pyrolysis 0

Pyrolysis kinetic constants:

$$G = Ae^{-B/T}$$

$$A = 2.78 \times 10^{-10} \ (\text{sec})^{-1}$$

$$B = 34\ 200 \ (°\text{R})$$

Reaction order $n = 3.0$

Char emissivity:

0.70 at 0°R

0.75 at 2000°R

0.92 at 2500°R

0.95 at 3500°R

0.95 at 10 000°R

(Linear interpolation between points)

Char specific heat: 0.37 Btu/lb-°F

APPENDIX C

TABLE C2.- MATERIAL PROPERTIES OF ESA-5500M

Ablator material conductivity, Btu/in.-sec-°R

$\lambda = 1.0$ (virgin plastic)		$\lambda = 0$ (char)	
3.0×10^{-6}	at 0°R	5.0×10^{-6}	at 0°R
3.0×10^{-6}	at 825°R	5.0×10^{-6}	at 450°R
2.5×10^{-6}	at 1050°R	10.0×10^{-6}	at 3500°R
2.5×10^{-6}	at 5100°R	10.0×10^{-6}	at 5500°R

(Linear interpolation between lambda and temperature points)

Pyrolysis gas specific heat:	0.60 Btu/lb-°F (constant with temperature)
Char density:	30.9 lb/cu ft
Virgin material density:	58.0 lb/cu ft
Virgin material specific heat:	0.20 to 0.30 Btu/lb-°F
Virgin material heat of pyrolysis:	0
Pyrolysis kinetic constants:	
Preexponential constant	$A = 2.78 \times 10^{-10}$ (sec)$^{-1}$
Activation energy	B = 34 200 (°R)
Reaction order	$n = 3.0$
Char emissivity:	0.85 at 0°R
	0.85 at 3000°R
	0.90 at 3500°R
	0.90 at 5500°R
Char specific heat:	0.25 to 0.35 Btu/lb-°F

APPENDIX C

For the inflatable airmat afterbody design, a flexible ablative material is required. This material must be capable of being bonded to the airmat and folded for transit to Mars. In addition, because of the possible discontinuity from the straight conical aeroshell to a bulged airmat section, transition to turbulent flow has been assumed. Therefore, the flexible ablator should be capable of relatively high heating rates. In this study, the PPA-1078 foamed elastomeric silicone-based material was selected. This material was initially under development for direct entry Mars missions before the development of the SLA-561 for the out-of-orbit lander configuration. Development information for the PPA-1078 material is documented in reference C28. Additional development and tests are required to obtain near optimum material for this application and to verify the capability of the material to withstand the long-term space exposure in the folded configuration. The thermal properties of PPA-1078 used in these analyses are given in table C3.

The design criteria adopted for the heat shield studies reflect the relative uncertainties associated with the various heating components. For the convective heating rates, a 1.5 factor of safety has been used, which is based on past evaluations of the degree of confidence of convective heating analyses. A factor of safety of 3.0 has been applied to the nonequilibrium bow shock radiation because it is the most uncertain heating component due to a lack of experimental data for corresponding gas mixtures and velocities. The equilibrium radiation analysis is considered more certain and has been assigned an uncertainty factor of safety of 2.0.

These factors of safety were applied to the calculated heating rates for the various trajectories considered and an ablation analyses (T-CAP) used to determine the required heat shield thickness. For the parametric study where many design conditions were considered, the required thicknesses were based on a 400°F peak bond line temperature at anytime up to lander separation. However, for the point design studies, a more explicit criterion was used, which consisted of limiting the bond line temperature to 300°F maximum at time of peak dynamic pressure or 600°F anytime up to lander separation. This is somewhat less conservative than the 400°F peak temperature at anytime; however, it is consistent with structural design criteria.

APPENDIX C

TABLE C3.- MATERIAL PROPERTIES OF PPA-1078

Ablator material conductivity, Btu/in.-sec-°R

λ = 1.0 (virgin plastic)		λ = 0 (char)	
1.5×10^{-6}	at 0°R	2.5×10^{-6}	at 0°R
1.5×10^{-6}	at 825°R	2.5×10^{-6}	at 1450°R
1.25×10^{-6}	at 1050°R	5.0×10^{-6}	at 3500°R
1.25×10^{-6}	at 5100°R	5.0×10^{-6}	at 5500°R

(Linear interpolation between lambda and temperature points)

Pyrolysis gas specific heat:	0.60 Btu/lb-°F (constant with temperature)
Char density:	15.0 lb/cu ft
Virgin material density:	50.0 lb/cu ft
Virgin material specific heat:	0.20 to 0.30 Btu/lb-°F
Virgin material heat of pyrolysis:	0
Pyrolysis kinetic constants:	
Preexponential constant	$A = 2.78 \times 10^{-10}$ (sec)$^{-1}$
Activation energy	$B = 34\ 200$ (°R)
Reaction order	$n = 3.0$
Char emissivity:	0.85 at 0°R
	0.85 at 3000°R
	0.90 at 3500°R
	0.90 at 5500°R
Char specific heat:	0.25 to 0.35 Btu/lb-°F

APPENDIX C

Ablation Analysis Method

The T-CAP III Transient Charring Ablator Program was used to conduct the ablation analyses for this study. The analytical model employed in this program includes up to five material phases -- virgin plastic, the pyrolysis zone, char, pyrolysis vapor, and a viscous melt layer. Histories of the aerothermal and aeromechanical environment are described by curves of convective and radiative heating rates and viscous shear stress and pressure gradients. The heat balance at the surface consists of convective and radiative heat inputs conduction into the ablative layer, convective heat blockage due to mass injection into the boundary layer, reradiation from the surface, and surface chemical reactions. Material removal due to heterogeneous surface reactions, vaporization, sublimation and mechanical erosion, and viscous melt flow are computed where applicable. Internally, the heat absorbed by the pyrolysis vapors as they flow through the char and the heat absorbed or produced during pyrolysis are included with the normal heat conduction and storage terms. The internal degradation, i.e., pyrolysis zone, is computed with an Arrhenius rate function with kinetics derived from Thermogravimetric Analysis (TGA) and plasma-arc data. The thermal response of internal insulation and structure can be included as required for both one and two dimensional heat flow. The following are the equations programed for finite difference solution for arbitrary inputs of material properties and time dependent surface environments:

1) Surface heat balance,

$$\dot{q}\ (\text{conduction}) = \dot{q}\ (\text{convective}) + \dot{q}\ (\text{radiation}) \pm \dot{q}\ (\text{chemical}) - \dot{q}\ (\text{reradiation})$$

$$k \left.\frac{dT}{dx}\right|_{\text{surface}} = \rho_e \mu_e C_H \left(H_r - H_w\right) + \dot{q}_r \pm r\dot{m}_c \Delta H_r - \sigma \epsilon T_w^4 \qquad \text{(C1)}$$

where

k = ablator thermal conductivity

$\rho_e \mu_e C_H$ = net heat transfer coefficient

H_r = recovery enthalpy

$\dot{q}_r$ = radiation heating rate

$\dot{m}_c$ = mass loss rate of surface material

ΔH_r = heat of reaction

σ = Stephan-Boltzmann constant

ϵ = emissivity

T_w = surface temperature;

2) Ablative layer heat balance,

$\dot{q}$ (stored) - $\dot{q}$ (conduction) - $\dot{q}$ (transpiration)

$\dot{q}$ (pyrolysis)

$$\rho(x)c_p \frac{dT}{dt} = \frac{\partial}{\partial x} \frac{(kT)}{\partial x} - \dot{m}_v (x,t)\, c_{p_g} \frac{\partial T}{\partial x} + f\rho_{vp}\, L_p\, (x) \frac{\partial \lambda}{\partial t} \tag{C2}$$

where

$\rho(x)$ = ablator density at x
c_p = ablator specific heat
$\dot{m}_v$ = pyrolysis vapor mass flow at x
c_{p_g} = vapor specific heat
f = volatile fraction of ablator
ρv_p = ablator virgin density
L_p = heat of pyrolysis
$\lambda(x)$ = nondimensional density.

In the ablative layer, the degree of material degradation is described by a nondimensional density λ which is defined as the weight fraction that the pyrolysis reaction has to go to completion. The rate at which the material pyrolyses is a function of and the reaction kinetics. Thus;

$$\frac{\partial \lambda}{\partial t} = -k_r \lambda^n \tag{C3}$$

where

$$\lambda = \frac{\rho(x) - \rho\text{char}}{\rho_{vp} - \rho\text{char}}$$

$k = Ae^{-B/T}$

A,B = Arrhenius rate constants

n = reaction order.

The material reaction kinetics and the order of reaction are obtained for a particular material by TGA. The ablator density at any point and at any time is given by

$$\rho(x,t) = \rho(x,t)\ (\rho_{vp} - \rho\text{char}) + \rho\text{char} \tag{C4}$$

while the mass flux is given by

$$r\dot{m}_v (x,t) = -f\rho_{vp} \int_o^x \frac{\partial\lambda}{\partial t} dx \qquad (C5)$$

where applicable material properties used in the T-CAP III program are taken as temperature-dependent. In addition, thermal conductivity and specific heat are also taken as functions of density to account for changes through the pyrolysis and char zones.

Surface recession.- The mechanisms that control surface recession are functions of the ablative material surface composition and boundary layer gas chemical composition. In the T-CAP III computer program, several optional methods of computing surface recession are used. The particular method selected depends on the types of surface recession, e.g., melting or burning.

Thermochemical recession.- The thermochemical reactions that must be considered for Mars atmospheres are carbon reactions with carbon dioxide and nitrogen and carbon sublimation for graphitic materials (e.g., ESA-5500M and PPA-1078) and vaporization for siliceous materials (e.g., SLA-561). The heating rates typical of Mars entires, being relatively moderate, do not produce temperatures sufficient to initiate nitrogen reactions or sublimation of carbonaceous materials, and, in general, gas phase dissociation of the CO_2 is unimportant as it affects surface recession. Thus, the dominant reaction to be considered is the C-CO_2 reaction. The rate at which this reaction occurs depends on both the reactivity of the material and the rate at which CO_2 is made available to the surface, and the degree of characterization of the materials thermochemical and thermomechanical response to the predicated environment.

An Arrhenius rate equation is used to represent this reaction and, in terms of mass loss of material, is expressed as

$$\dot{m}_c = p^n_{CO_{2w}} k_o e^{-E/RT_w} \qquad (C6)$$

This expression shows that, at constant carbon dioxide pressure, as temperature increases, the reaction rate rises exponentially. However, an increase in reaction rates must necessarily be accompanied by an increased flux of reaction products from the surface. Because removal of the reaction products from the surface is accomplished at a finite rate by convection and diffusion, any increase in mass loss rate due to a temperature increase must result in a decrease in the reactant availability at the reacting surface. Therefore, $P_{CO_{2w}}$ also depends on the boundary layer mass transfer mechanisms. Assuming that the only heterogeneous reactions taking place are oxidative and that carbon monoxide is the only reaction product, it can be shown that the carbon mass flow is related to the mass fraction of CO_2 (at the wall and boundary layer edge) and the boundary layer mass transfer coefficient is as indicated in equation (C2).

$$\dot{m}_c = \frac{\rho_e \mu_e C_m \left(K_{CO_{2e}} - K_{CO_{2w}}\right)}{K_{CO_{2w}} + \frac{M_{CO_2}}{M_c}} \qquad (C7)$$

Equations (C6) and (C7) are independent equations with the unknowns of surface mass flow and quantity of available CO_2. These equations are solved simultaneously for $K_{CO_{2w}}$ and $\dot{m}_c$ and, thus, account for both the so-called rate limited and diffusion limited regimes.

At higher temperatures where sublimination and nitrogen reactions are predominant and vaporization of siliceous materials is significant, thermochemical equilibrium between the char and boundary layer species is assumed with surface recession being controlled by diffusion in the boundary layer. In this case, the net flux of each element is given by equation (C8).

$$(\dot{m})_{iw} = \left(\dot{m}\,\bar{K}_i\right)_w - \rho_e \mu_e C_H \left(\bar{K}_{i_e} - \bar{K}_{i_w}\right) \qquad (C8)$$

These equations, coupled with a general chemical equilibrium requirement at the surface, are solved for the mass transfer and surface recession.

Mechanical erosion.- Mechanical surface shear is significant only for the melting ablative materials in that it controls the melt flow.

The analysis for materials that form a viscous melt layer use the following equations to compute surface recession rates assuming a continuum melt flow:

$$r_{flow} = \int \frac{1}{R} \frac{d}{ds} (uR)\, dx \qquad (C9)$$

where

u = tangential velocity

$$= \tau \int \frac{1}{\mu}\,dy + \left(\frac{dp}{ds} - \rho g \sin\theta\right)\int \frac{x}{\mu}\,dx \qquad (C10)$$

τ = aerodynamic shear stress

$\frac{dp}{ds}$ = local pressure gradient

μ = melt viscosity

R = local body radius.

Parametric study.- Parametric heat shield thickness data and material selections for the out-of-orbit and direct modes have been obtained for a reference aeroshell configuration of 70° half-angle cone with a bluntness ratio of $R_N/R_B = 0.5$ and a 0.030-in. aluminum structure. The data encompass the following range of entry conditions -- entry angles (γ_e) from 3σ above skipout boundary to 20° for out of orbit, and 38° for direct mode, ballistic coefficient (B) from 0.1 to 0.6 slugs/ft^2, and aeroshell base diameters of 6, 15, and 30 ft. The study considered nominal entry velocities of 15 000 fps for the orbit case and 21 000 fps for the direct mode. The effect of velocity variations of ±1 000 fps was evaluated for the orbital case and was found to have only a small effect on the heat shield thicknesses. This is shown in figures C37 and C40. Velocity variations for the direct entry mode are more significant because of the direct influence on the shock layer radiation levels.

Ablator thicknesses for three aeroshell diameters, for the stagnation region and for the cone edge, and for the direct and the out-of-orbit cases are presented in figures C36 thru C47. Discontinuities appear in the direct entry curves. This is caused by the switch from SLA-561 to ESA-5500M at a heating rate of 100 Btu/ft^2 sec for the VM-4 atmosphere. Although the VM-4 atmosphere higher heating rate defines this material transition, the higher total heat VM-7 atmosphere determines the thickness requirement. Thus the material switch is defined by VM-4 but the thicknesses are set in either case by VM-7. In figures C46 and C47, two discontinuities appear. The second discontinuity is caused by the transition to turbulent flow for the VM-7 atmosphere. Because the ablator thicknesses are calculated for only the stagnation point and the cone edge, an estimate of the thickness distribution was made for laminar flow and turbulent flow based on the heating distributions.

These estimated thickness distributions, shown in figures C48 and C49, were used in conjunction with the stagnation point and cone edge thickness curves to estimate the weights for the heat shield system. The ablator thicknesses for the flap extensions were taken as the cone edge values. For the airmat afterbody extensions, the ablator thickness for the PPA-1078 is given in figure C50.

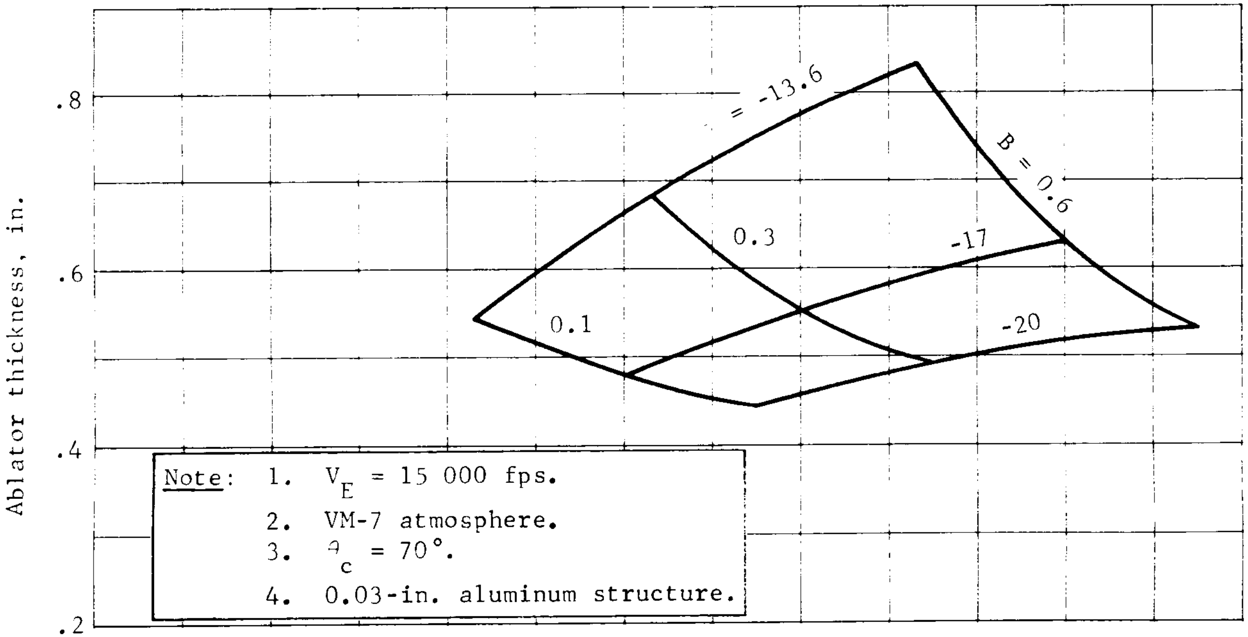

Note: 1. V_E = 15 000 fps.

2. VM-7 atmosphere.

3. $\theta_c = 70°$.

4. 0.03-in. aluminum structure.

Figure C36.- Orbital Entry Mode, Ablator Thickness, Stagnation Point SLA-561, Factored Heating, R_N/R_B = 0.5, Base Diameter = 6 ft

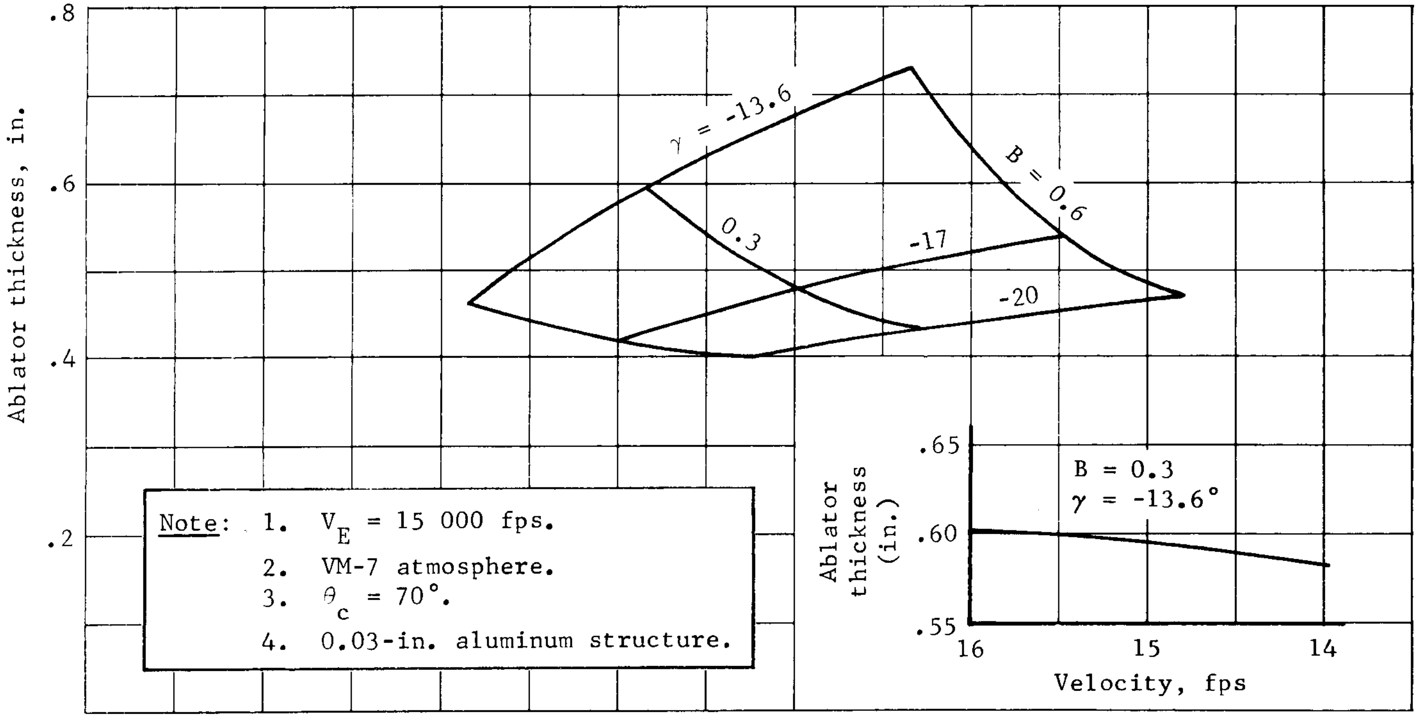

Note: 1. V_E = 15 000 fps.
2. VM-7 atmosphere.
3. θ_c = 70°.
4. 0.03-in. aluminum structure.

Figure C37.- Orbital Entry Mode, Ablator Thickness, Stagnation Point, SLA-561, Factored Heating, R_N/R_B = 0.5, Base Diameter = 15 ft

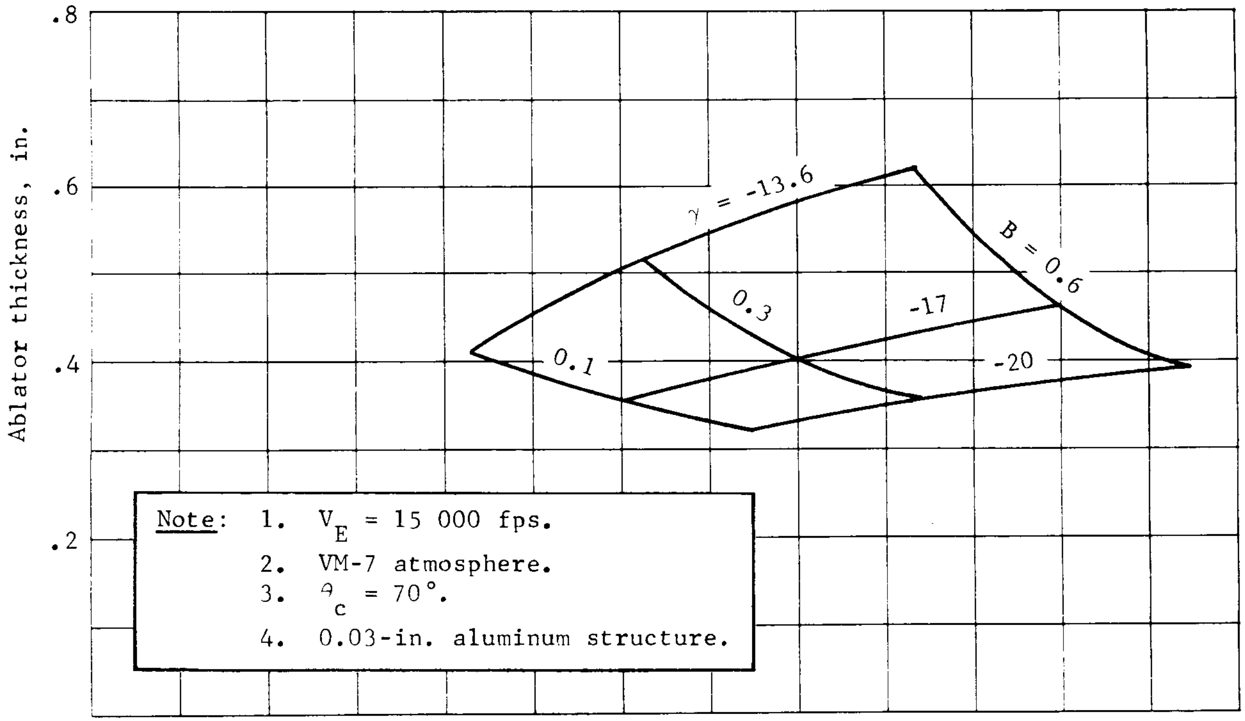

Note: 1. V_E = 15 000 fps.
2. VM-7 atmosphere.
3. $\theta_c = 70°$.
4. 0.03-in. aluminum structure.

Figure C38.- Orbital Entry Mode, Ablator Thickness, Stagnation Point, SLA-561, Factored Heating, $R_N/R_B = 0.5$, Base Diameter = 30 ft

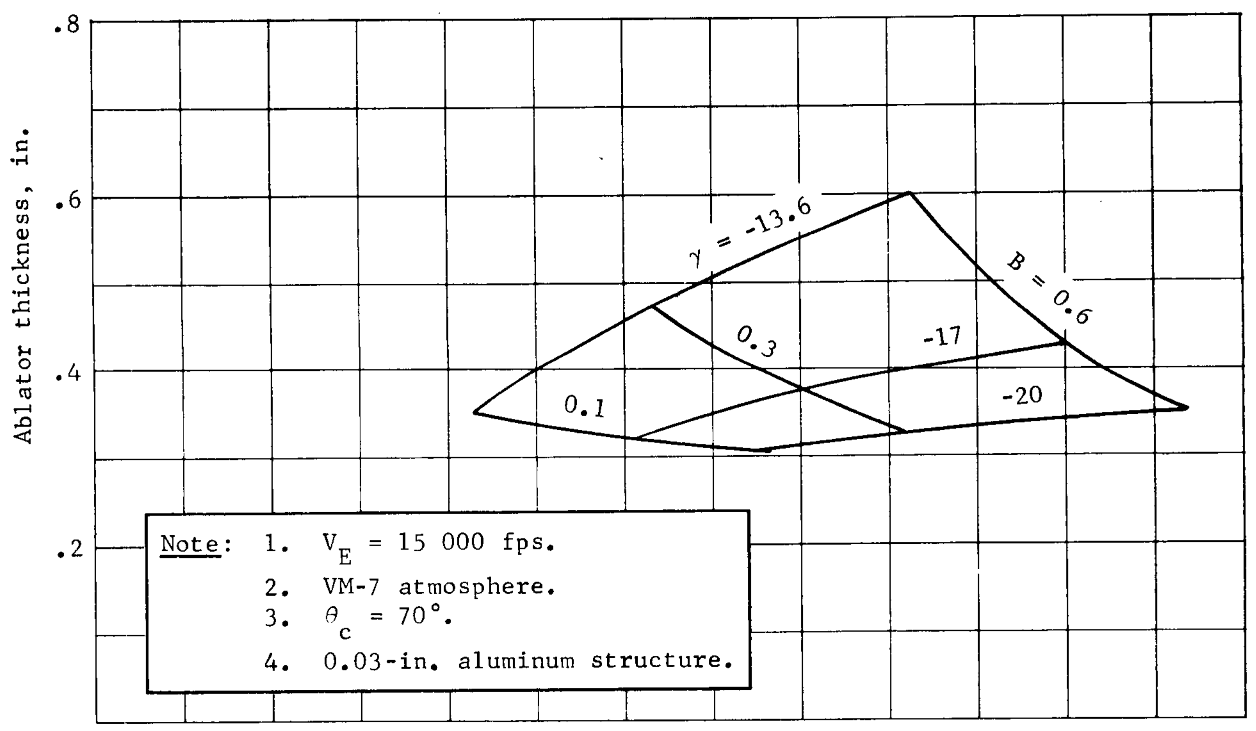

Note: 1. V_E = 15 000 fps.
2. VM-7 atmosphere.
3. θ_c = 70°.
4. 0.03-in. aluminum structure.

Figure C39.- Orbital Entry Mode, Ablator Thickness, Cone Edge, SLA-561, Factored Heating, R_N/R_B = 0.5, Base Diameter = 6 ft

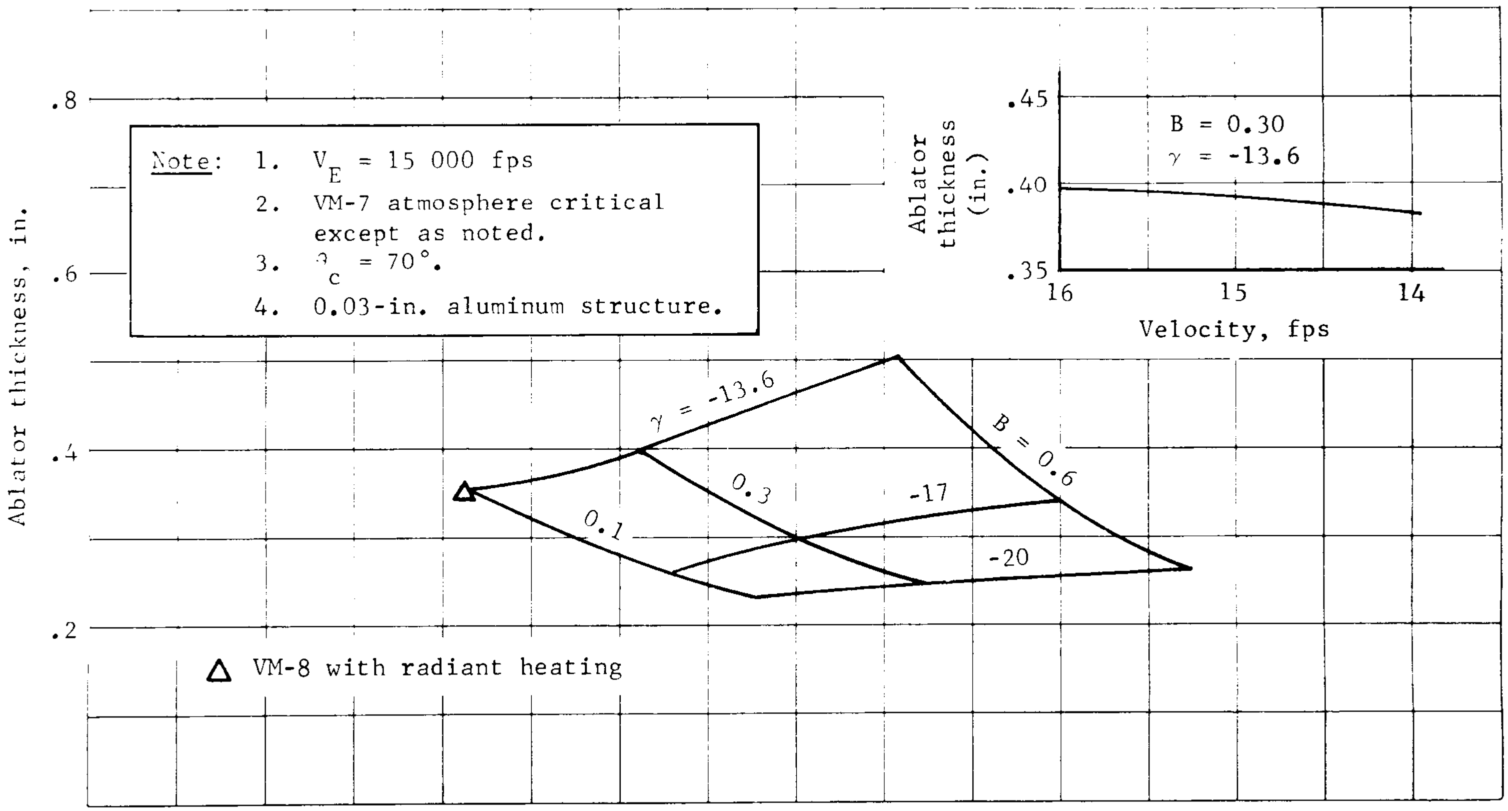

Note:
1. V_E = 15 000 fps
2. VM-7 atmosphere critical except as noted.
3. θ_c = 70°.
4. 0.03-in. aluminum structure.

△ VM-8 with radiant heating

Figure C40.- Orbital Entry Mode, Ablator Thickness, Cone Edge, SLA-561 Factored Heating, R_N/R_B = 0.5, Base Diameter = 15 ft

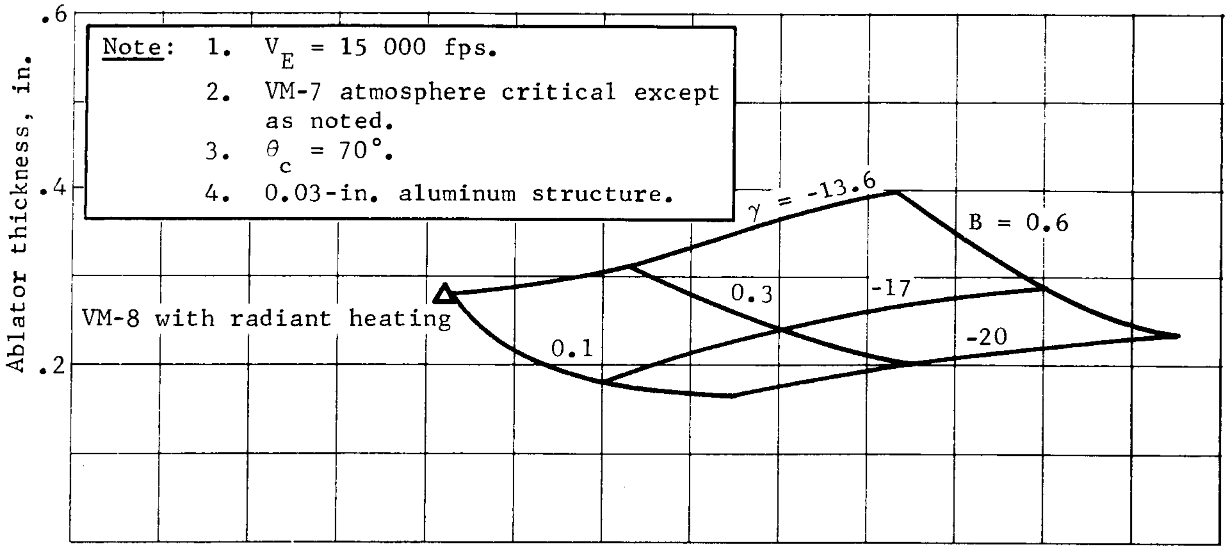

Figure C41.- Orbital Entry Mode, Ablator Thickness, Cone Edge, SLA-561, Factored Heating, R_N/R_B = 0.5, Base Diameter = 30 ft

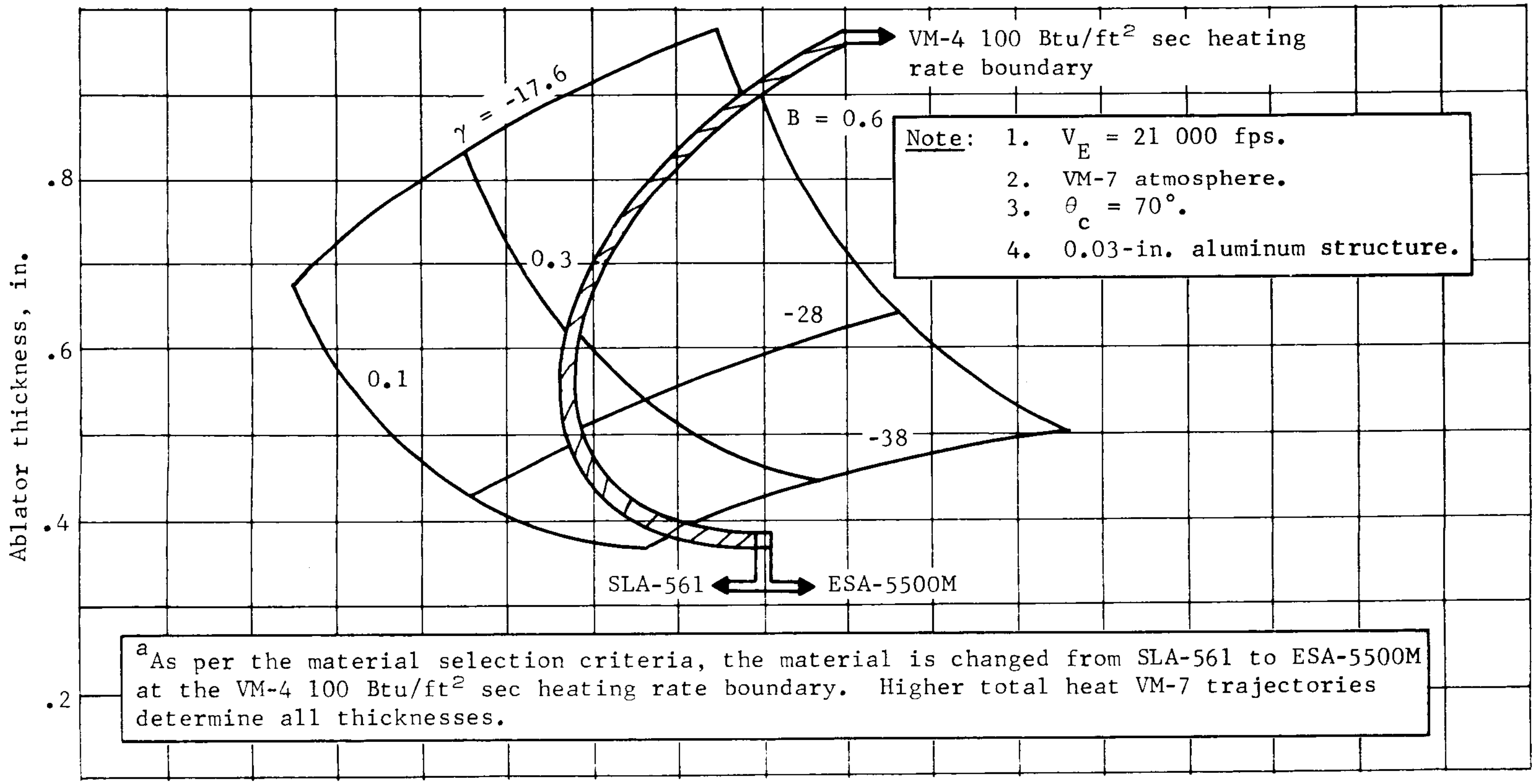

Note: 1. V_E = 21 000 fps.
2. VM-7 atmosphere.
3. θ_c = 70°.
4. 0.03-in. aluminum structure.

[a] As per the material selection criteria, the material is changed from SLA-561 to ESA-5500M at the VM-4 100 Btu/ft² sec heating rate boundary. Higher total heat VM-7 trajectories determine all thicknesses.

Figure C42.- Direct Entry Mode, Ablator Thickness, Stagnation Point, Factored Heating, R_N/R_B = 0.5, Base Diameter[a]

Note: 1. V_E = 21 000 fps
2. VM-7 atmosphere.
3. θ_c = 70 °C.
4. 0.03-in. aluminum structure.

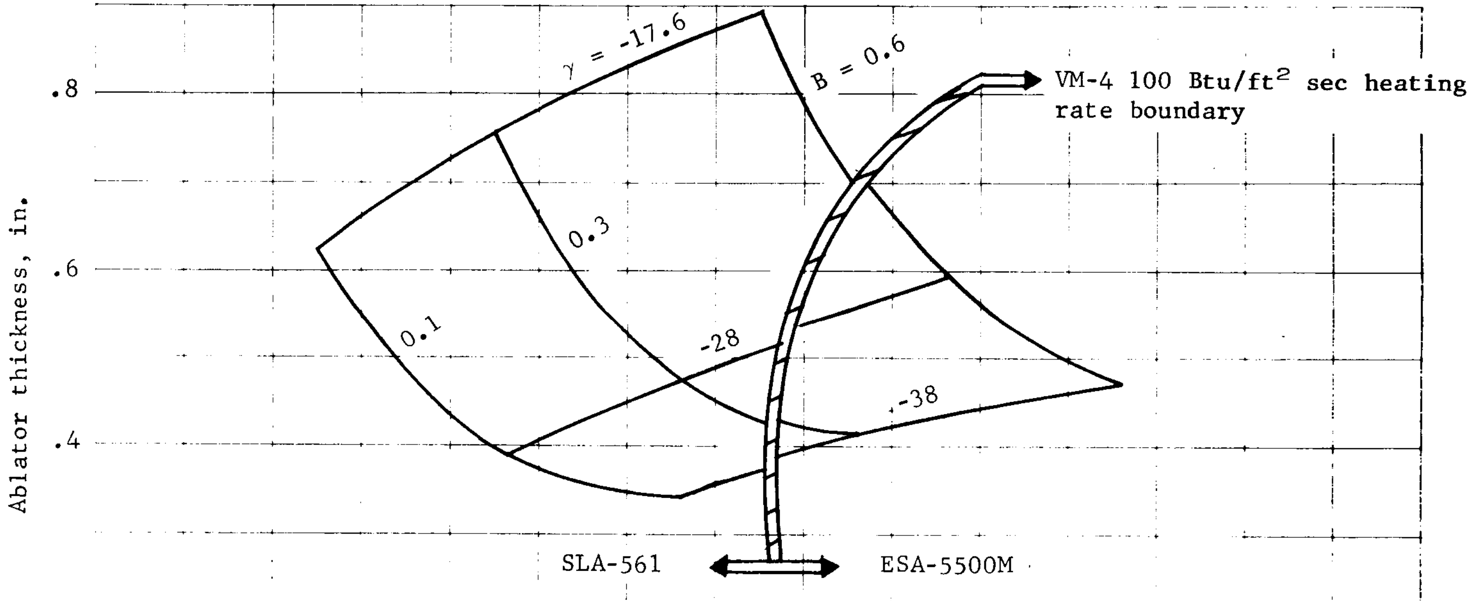

[a] As per the material selection criteria, the material is changed from SLA-561 to ESA-5500M at the VM-4 100 Btu/ft^2 sec heating rate boundary. Higher total heat VM-7 trajectories determine all thicknesses.

Figure C43.- Direct Entry Mode, Ablator Thickness, Stagnation Point, Factored Heating, R_N/R_B = 0.5, Base Diameter = 15 ft[a]

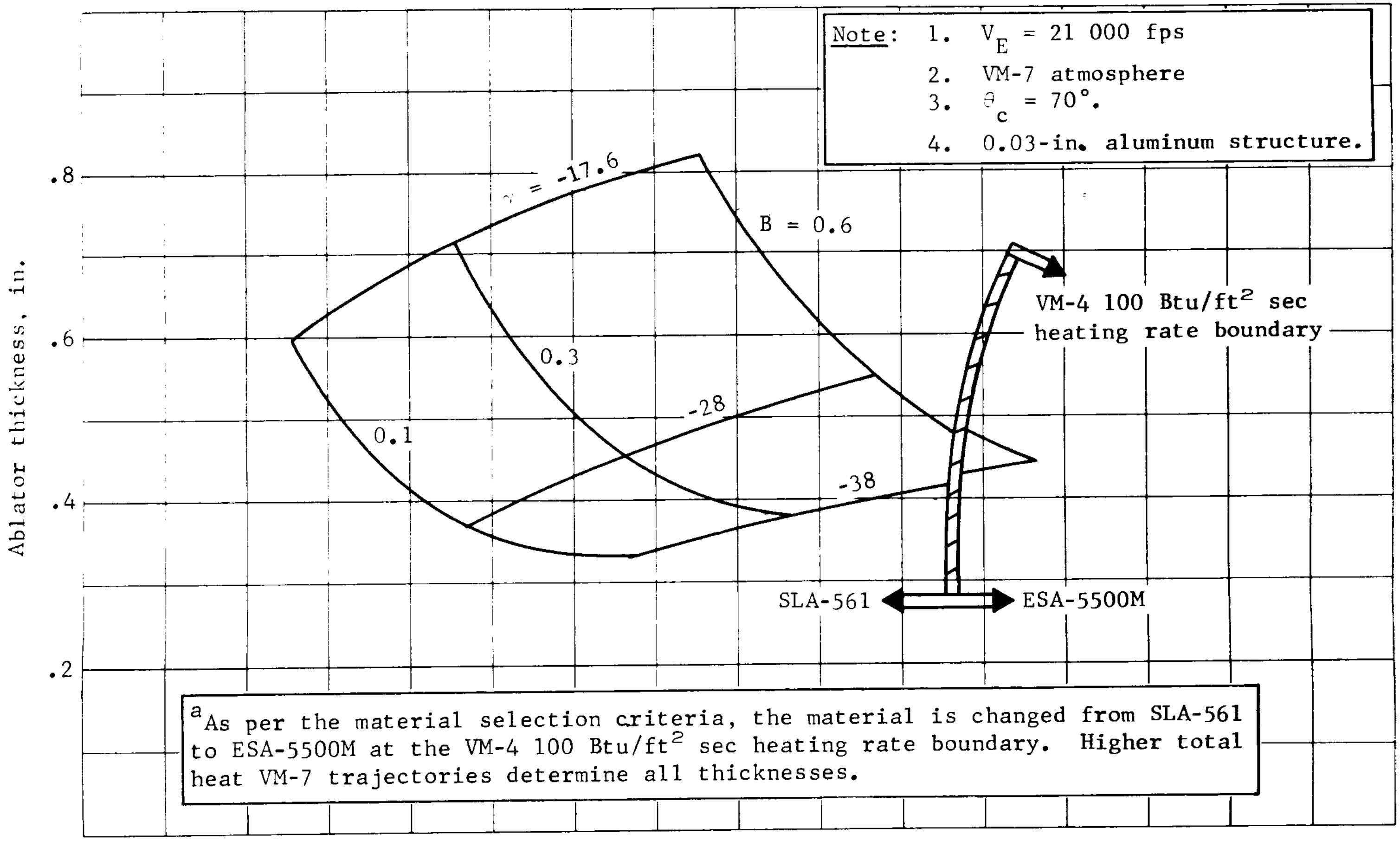

Note: 1. V_E = 21 000 fps
2. VM-7 atmosphere
3. θ_c = 70°.
4. 0.03-in. aluminum structure.

[a] As per the material selection criteria, the material is changed from SLA-561 to ESA-5500M at the VM-4 100 Btu/ft^2 sec heating rate boundary. Higher total heat VM-7 trajectories determine all thicknesses.

Figure C44.- Direct Entry Mode, Ablator Thickness, Stagnation Point, Factored Heating R_N/R_B = 0.5, Base Diameter = 30 ft[a]

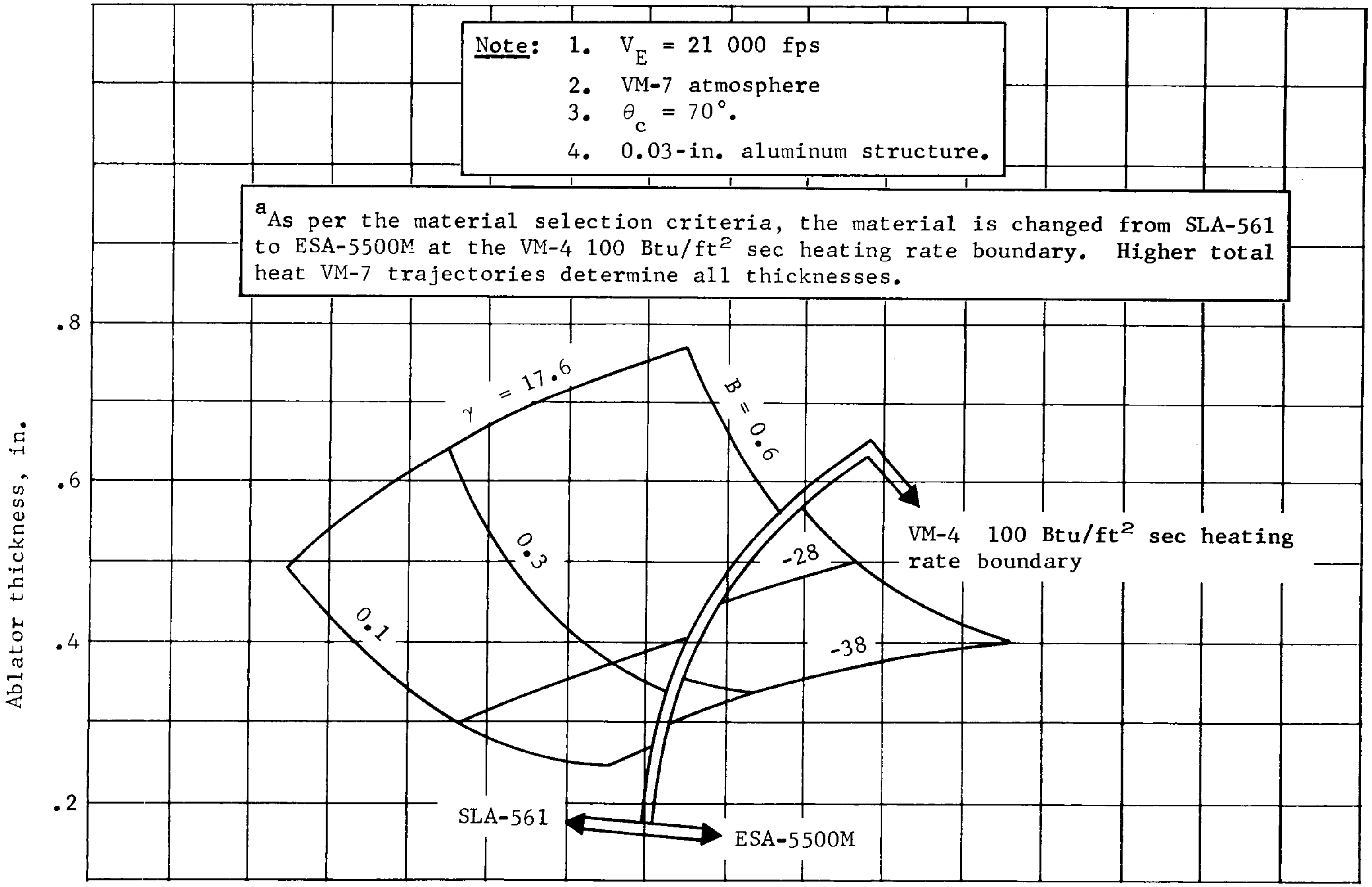

Note: 1. V_E = 21 000 fps
2. VM-7 atmosphere
3. θ_c = 70°.
4. 0.03-in. aluminum structure.

[a] As per the material selection criteria, the material is changed from SLA-561 to ESA-5500M at the VM-4 100 Btu/ft^2 sec heating rate boundary. **Higher total heat VM-7 trajectories determine all thicknesses.**

Figure C45. - Direct Entry Mode, Ablator Thickness, Cone Edge, Factored Heating, R_N/R_B = 0.5, Base Diameter = 6 ft[a]

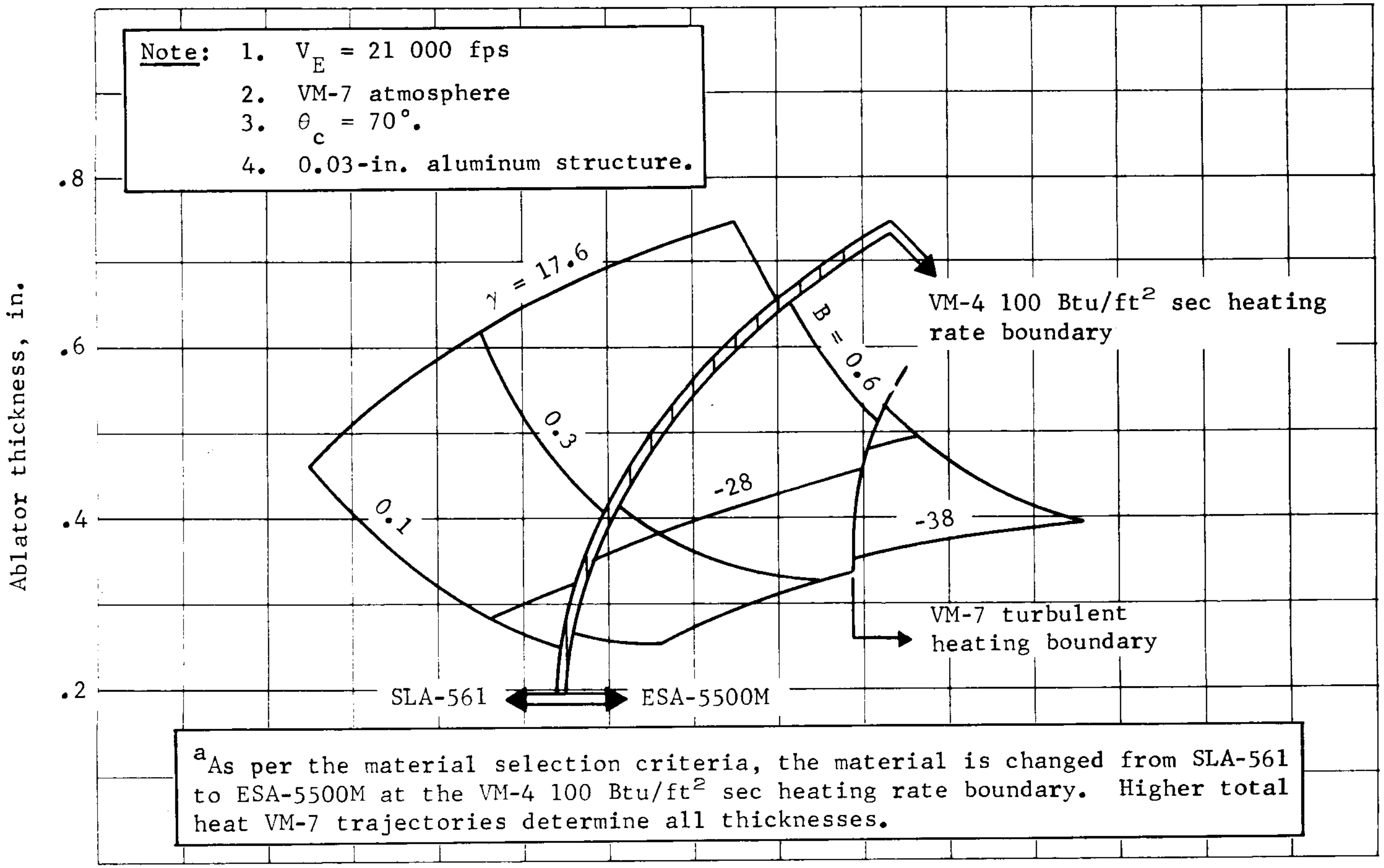

Note:
1. V_E = 21 000 fps
2. VM-7 atmosphere
3. θ_c = 70°.
4. 0.03-in. aluminum structure.

[a] As per the material selection criteria, the material is changed from SLA-561 to ESA-5500M at the VM-4 100 Btu/ft^2 sec heating rate boundary. Higher total heat VM-7 trajectories determine all thicknesses.

Figure C46.- Direct Entry Mode, Ablator Thickness, Cone Edge, Factored Heating R_N/R_B = 0.5, Base Diameter = 15 ft[a]

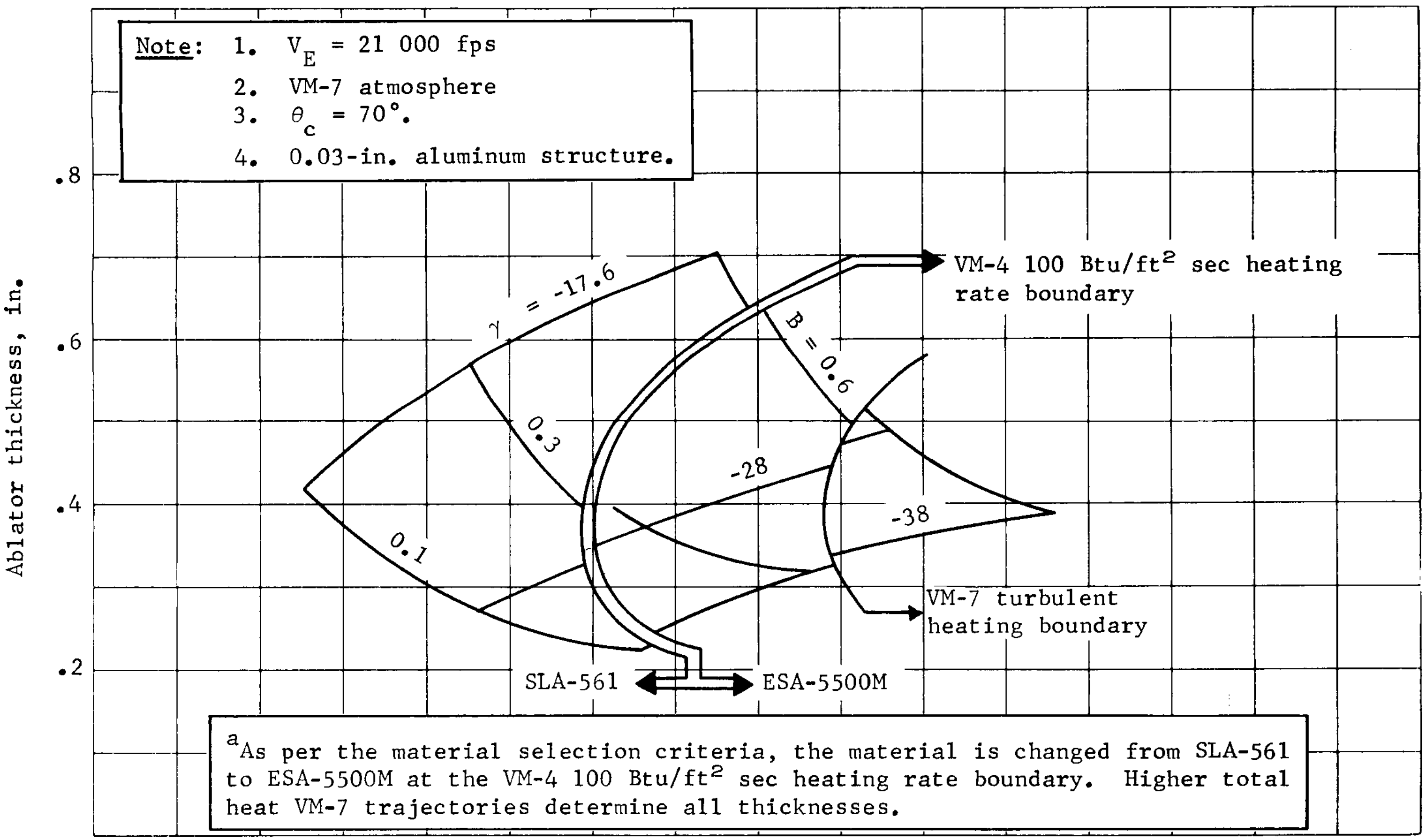

Note:
1. V_E = 21 000 fps
2. VM-7 atmosphere
3. $\theta_c = 70°$.
4. 0.03-in. aluminum structure.

[a]As per the material selection criteria, the material is changed from SLA-561 to ESA-5500M at the VM-4 100 Btu/ft^2 sec heating rate boundary. Higher total heat VM-7 trajectories determine all thicknesses.

Figure C47.- Direct Entry Mode, Ablator Thickness, Cone Edge, Factored Heating R_N/R_B = 0.5, Base Diameter = 30 ft[a]

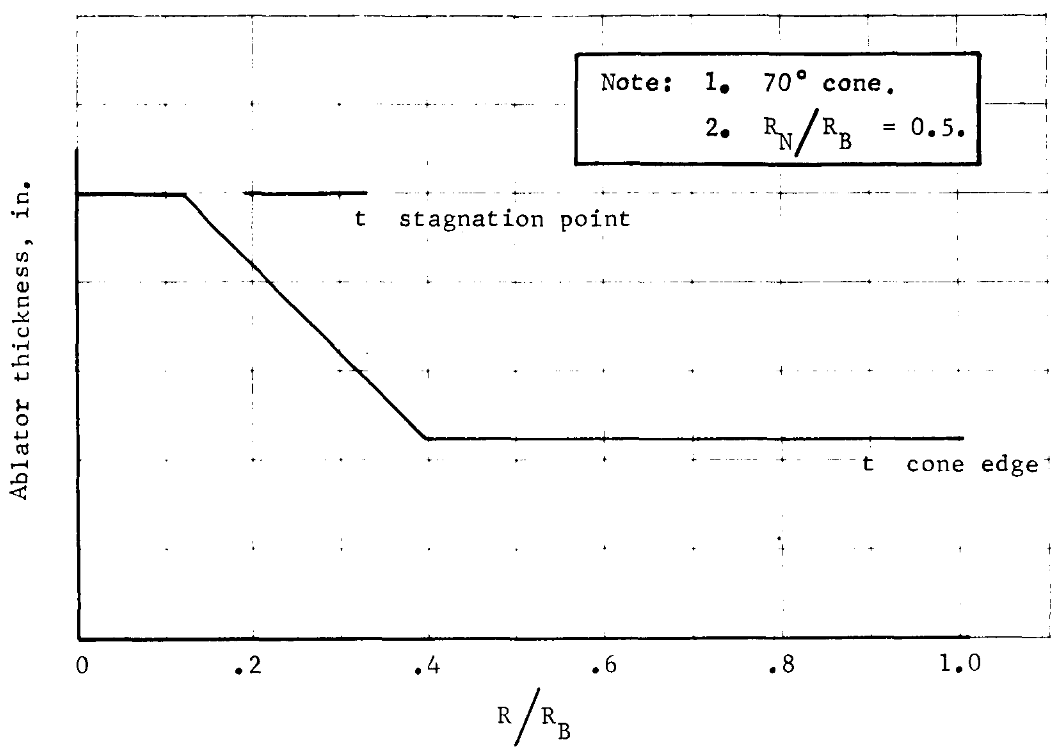

Figure C48.- Ablator Thickness Distribution (Laminar)

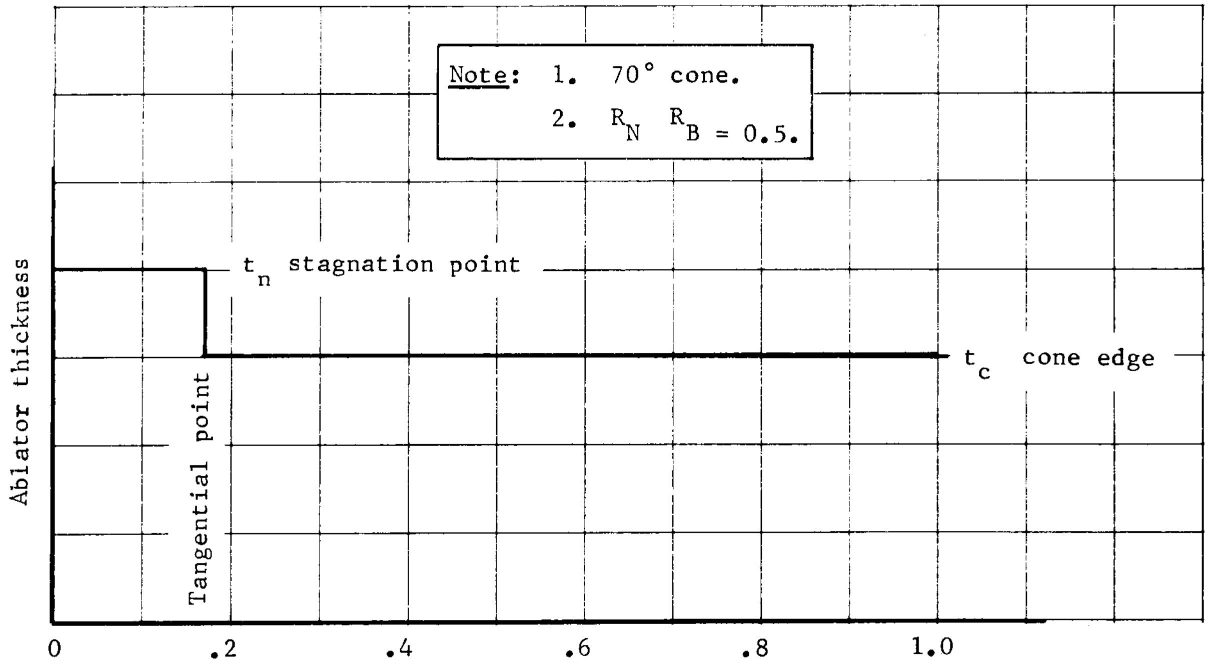

Figure C49. Ablator Thickness Distribution (Turbulent)

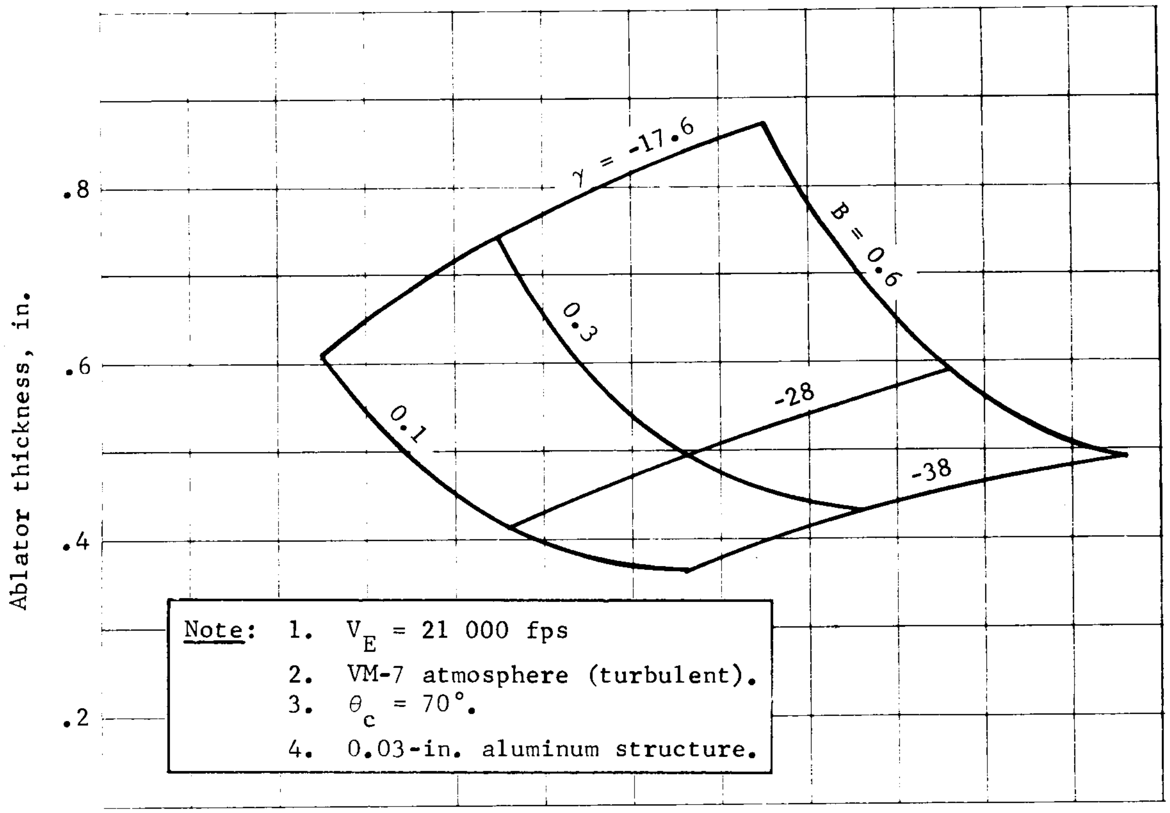

Note:
1. V_E = 21 000 fps
2. VM-7 atmosphere (turbulent).
3. θ_c = 70°.
4. 0.03-in. aluminum structure.

Figure C50.- Direct Entry Mode, Ablator Thickness, Airmat, PPA - 1078, Factored Heating, R_N/R_B = 0.5, Base Diameter = 30 ft.

APPENDIX C

3. AEROSHELL PARAMETRIC STUDY

The data presented herein are a result of aeroshell parametric studies conducted for the Mars Mission Mode Study. General approaches, assumptions, and methods of analysis are discussed. Resulting parametric weight curves are presented.

Study Approach

The aeroshell parametric studies considered an all-aluminum structure with deployable aluminum flaps or inflatable coated-Nomex fabric airmats as required to achieve the desired entry weights and ballistic coefficients.

The methods of analysis used in this study are outlined in this section of this appendix. The configurations analyzed are shown in figures C51 thru C53. The configuration consists of a truncated cone with the half-included angle ranging from 45 to 70°. Previous studies have investigated sandwich structure, integral-rectangular-frame stabilized monocoque structure, and channel-frame stabilized monocoque structure as methods of construction for the conical portion of the aeroshell. The result of this comparison was that the channel-frame structure was the most efficient; therefore, this design was used for the Mars Mission Mode Study.

The study considered a range of design pressures and loads that would satisfy anticipated design conditions for both the direct and orbital entry mode. Constraints on the analysis consist of minimum and/or maximum dimensions or material gages. Constraints on detail structure are given in figure C51. The maximum base diameter for the fixed portion of the aeroshell structure was fixed at 15 ft. Any requirement for a larger aeroshell was accomplished by use of flaps or airmat.

The parametric study initially considered the effect of payload frame radius and frame spacing (BS) on the weight of the conical shell structure in an effort to fix these two variables. Figures C54 and C55 show shell weight variation as a function of these two variables. Figure C54 does not include the weight of the payload frame that, as may be seen in figure C59, increases rapidly with increase in radius.

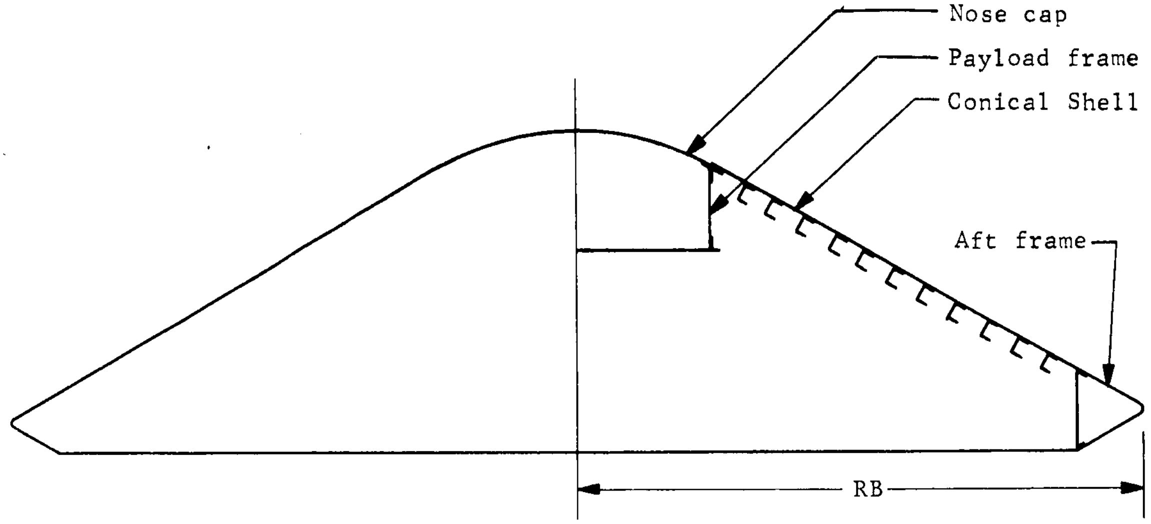
Nose cap
Payload frame
Conical Shell
Aft frame
RB

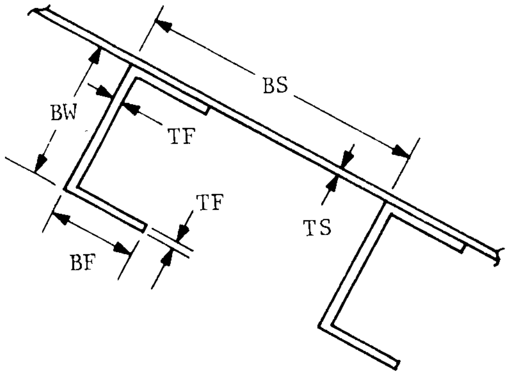
BS
BW
TF
TF
TS
BF

Frame detail

Minimum dimensions and gages, in.

BS = 2.0
TS = .020
BW = .50
BF = .25
TF = .015

Figure C51.- Intermediate Frame Details

As a result of the data in figure C54 and including the information implied in figure C59, the payload frame radius was fixed at the radius to the tangency between the aeroshell conical structure and nose cap. Figure C55 indicates that, for the range of pressures important to the Mars Mission Mode Study (1.0 to 15.0 psi), the frame spacing should be as small as practical. The frame spacing, at midcone, was fixed at 2.0 in. for the parametric study.

Within the constraints mentioned above, the data given in figures C56 thru C61 were generated. The design temperature was 70°F for the payload frame and 300°F for the remainder of the structure. Figures C56 thru C58 allow weighing any rigid aeroshell with a base radius (RB) from 2.0 to 10 ft, a design pressure from 1.0 to 50.0 psi (ultimate), and a half-included angle from 45 to 70°. The data in figure C59 are for a 70° aeroshell, but should be fairly representative down to a 60° aeroshell. Figures C60 and C61 are also for a 70° aeroshell and the effect of cone angle variation is not known at present.

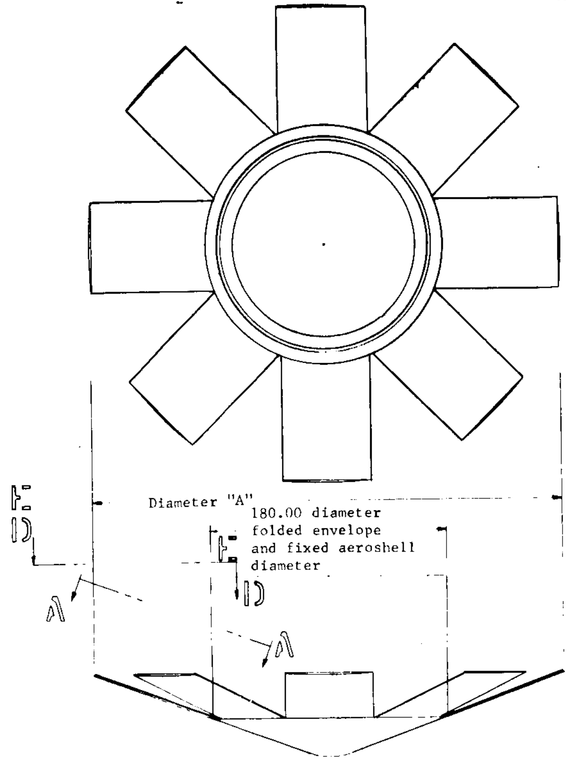
Diameter "A"
180.00 diameter folded envelope and fixed aeroshell diameter
E
D
A
E
D
A

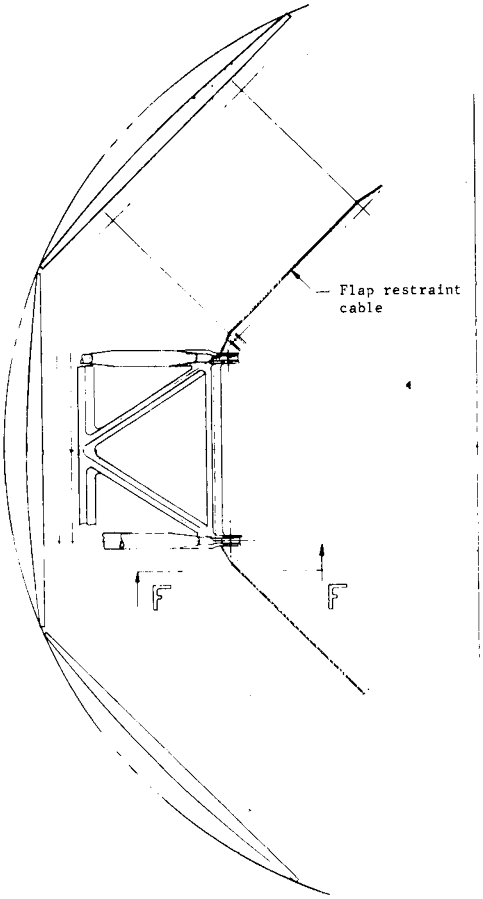
Flap restraint cable
F
F

E - E

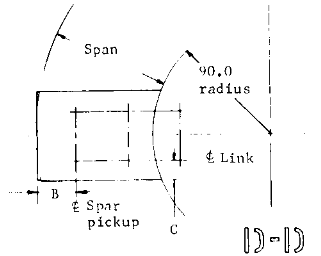
Span
90.0 radius
℄ Link
B
℄ Spar pickup
C

D-D

no scale

Diameter A, ft	Span, in.	B, in.	C, in.
20	30	10.5	14.00
25	60	21.0	14.00
30	90	31.5	15.00
35	120	42.0	19.50
40	150	52.5	24.00
45	180	63.0	26.00

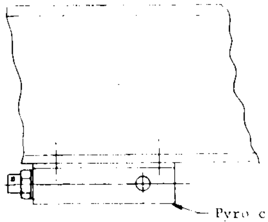
Pyro cable cutter (rotated 48° clockwise)

F - F

Figure C52.- Parametric Layout Study, 15-ft Diameter Fixed Aeroshell with Flaps

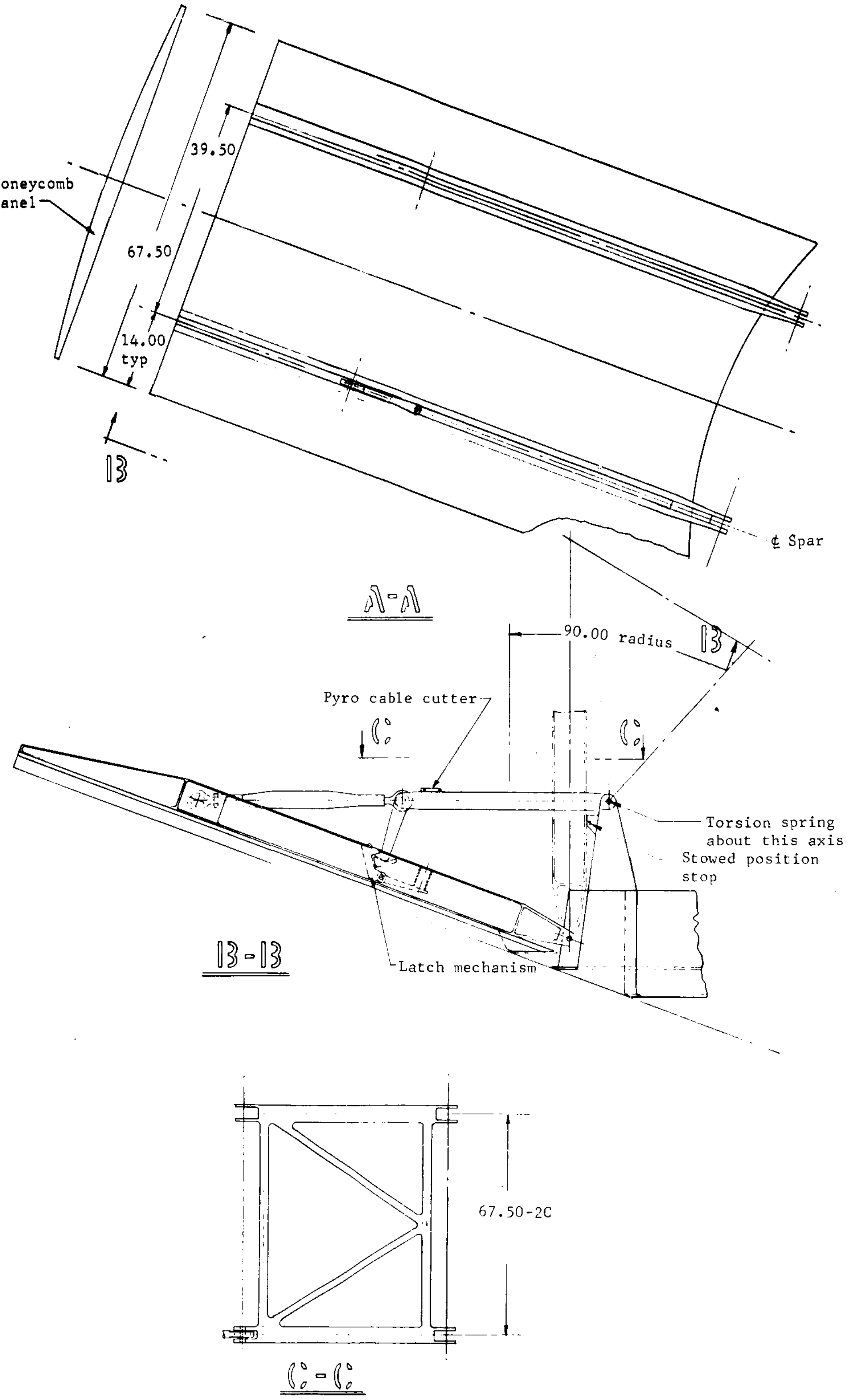
Aluminum honeycomb sandwich panel
39.50
67.50
14.00 typ
B
℄ Spar
A-A
90.00 radius
B
Pyro cable cutter
C
C
Torsion spring about this axis
Stowed position stop
Latch mechanism
B-B
67.50-2C
C-C

Figure C52.- Concluded

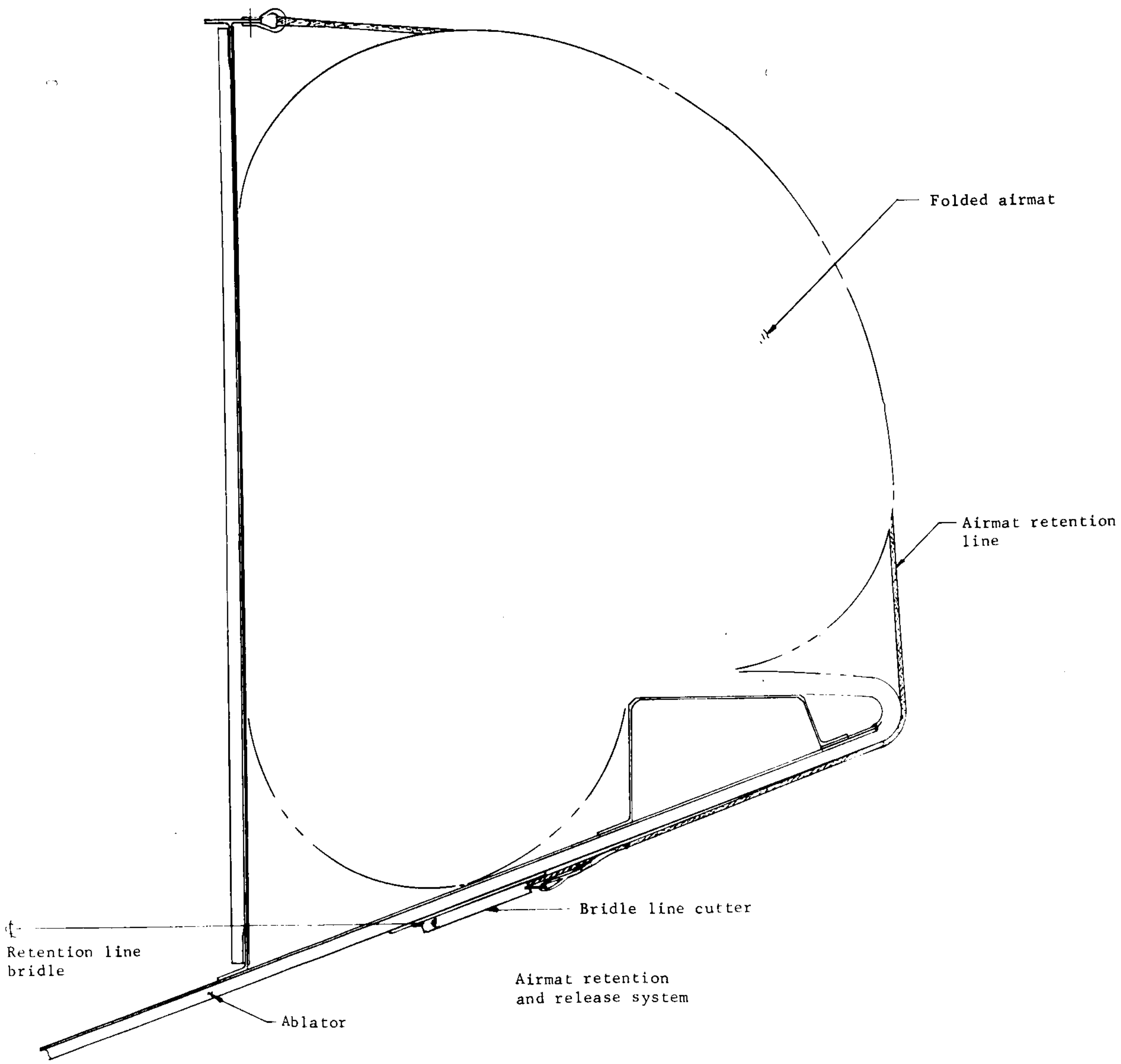
Folded airmat
Airmat retention line
Bridle line cutter
℄
Retention line bridle
Airmat retention and release system
Ablator

Figure C53.- Parametric Layout Study, 15-ft Diameter Fixed Aeroshell with Airmat Extension

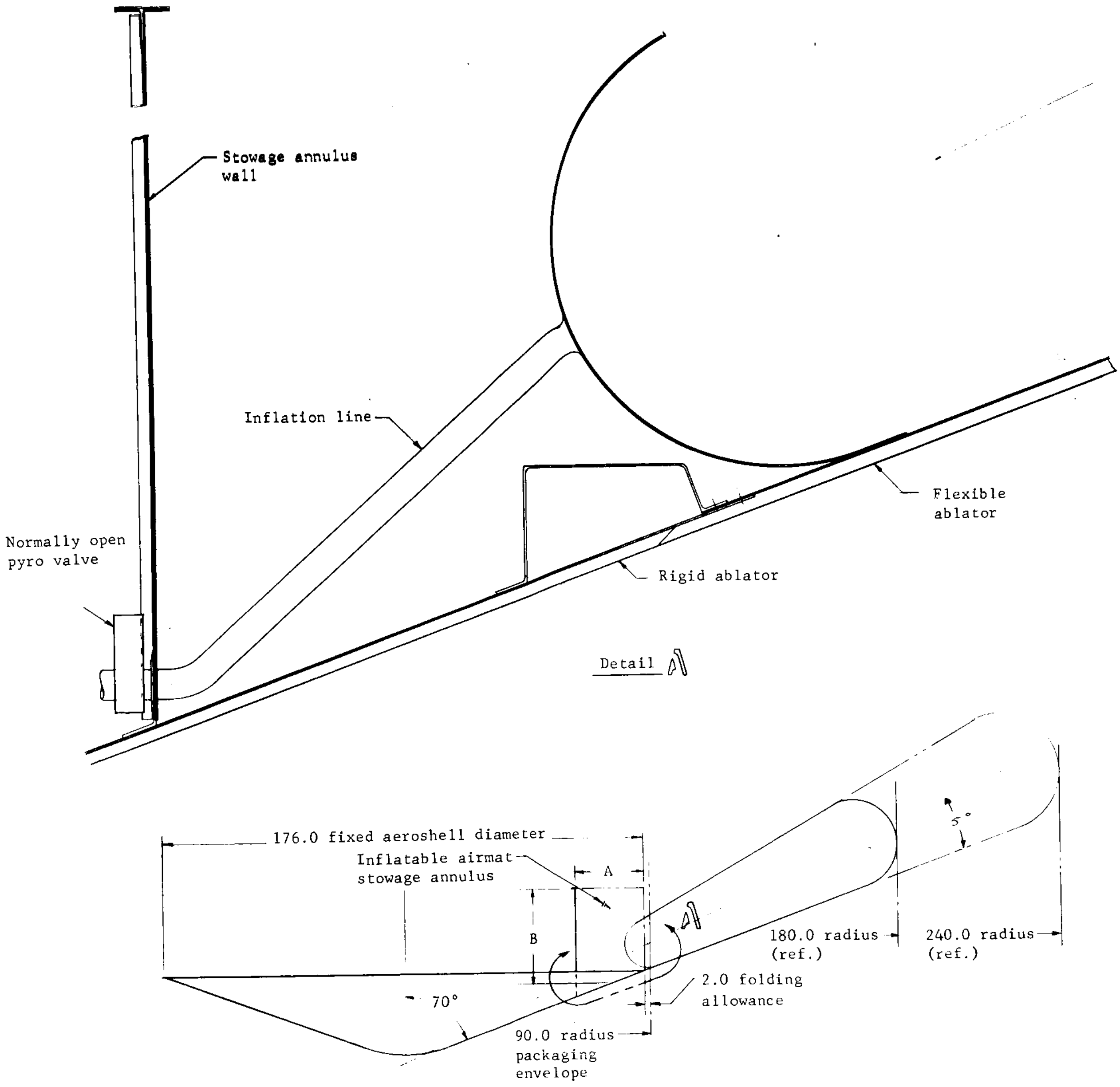
Stowage annulus wall
Inflation line
Normally open pyro valve
Flexible ablator
Rigid ablator
Detail A
176.0 fixed aeroshell diameter
Inflatable airmat stowage annulus
A
B
A
70°
5°
180.0 radius (ref.)
240.0 radius (ref.)
2.0 folding allowance
90.0 radius packaging envelope

Figure C53.- Concluded

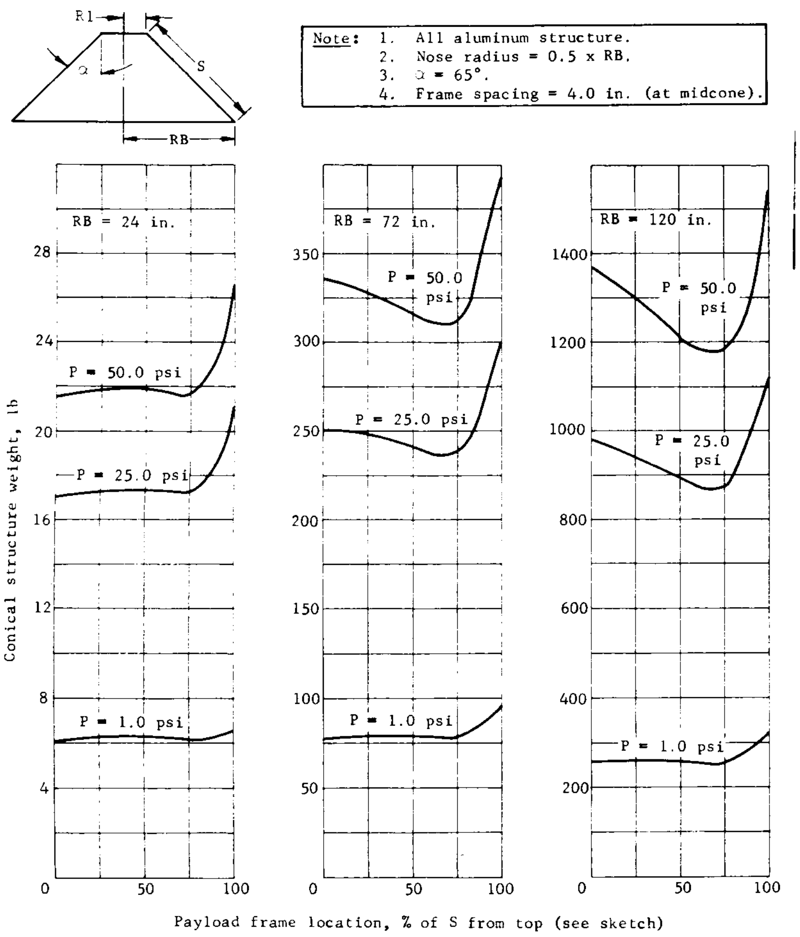

Note: 1. All aluminum structure.
2. Nose radius = 0.5 x RB.
3. α = 65°.
4. Frame spacing = 4.0 in. (at midcone).

Figure C54.- Aeroshell Parametric Studies, Effect of Payload Frame Radius on Weight of Conical Structure

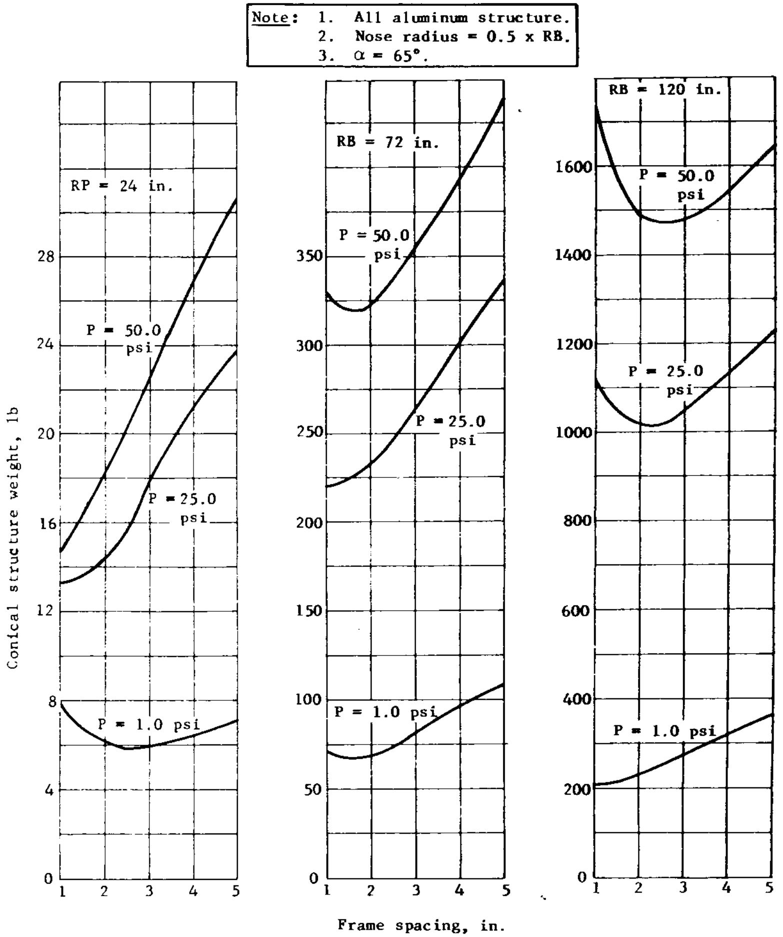

Note: 1. All aluminum structure.
2. Nose radius = 0.5 x RB.
3. α = 65°.

Figure C55.- Aeroshell Parametric Studies, Effect of Midcone Frame Spacing on the Weight of Conical Structure

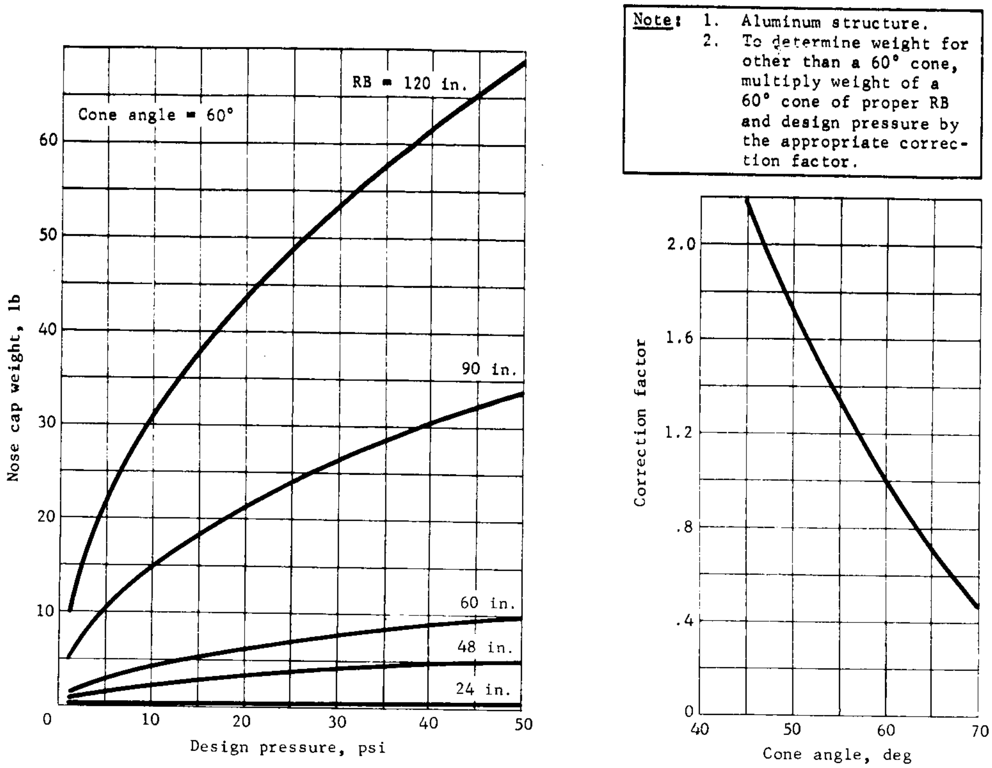

Note:
1. Aluminum structure.
2. To determine weight for other than a 60° cone, multiply weight of a 60° cone of proper RB and design pressure by the appropriate correction factor.

Figure C56.- Aeroshell Parametric Studies, Nose Cap Weight

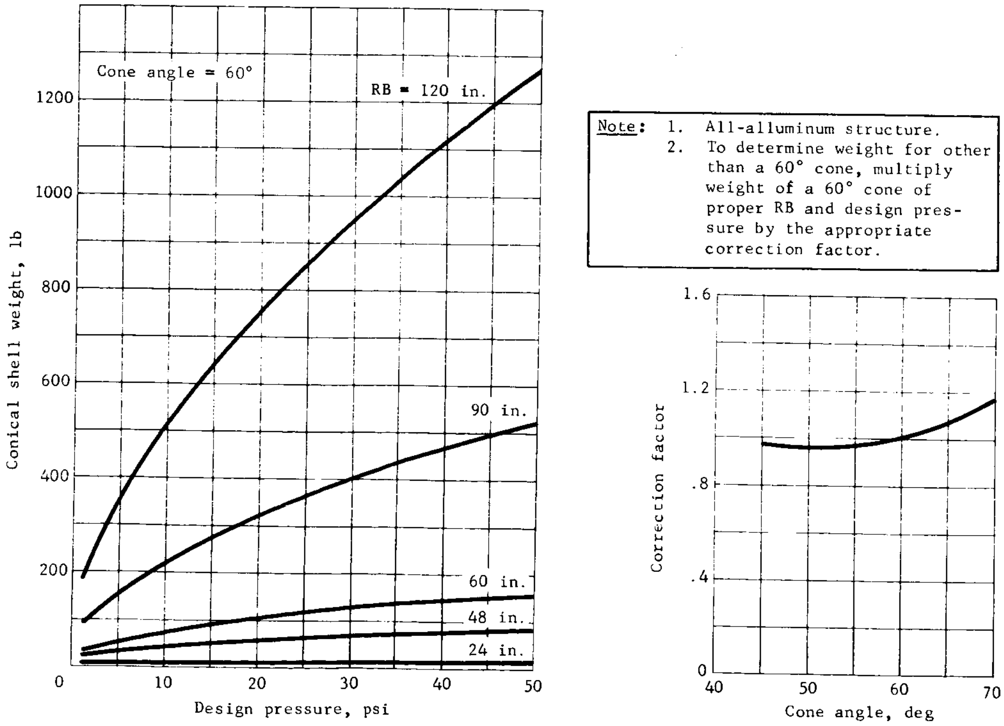

Note:
1. All-alluminum structure.
2. To determine weight for other than a 60° cone, multiply weight of a 60° cone of proper RB and design pressure by the appropriate correction factor.

Figure C57.- Aeroshell Parametric Studies, Conical Shell Weight

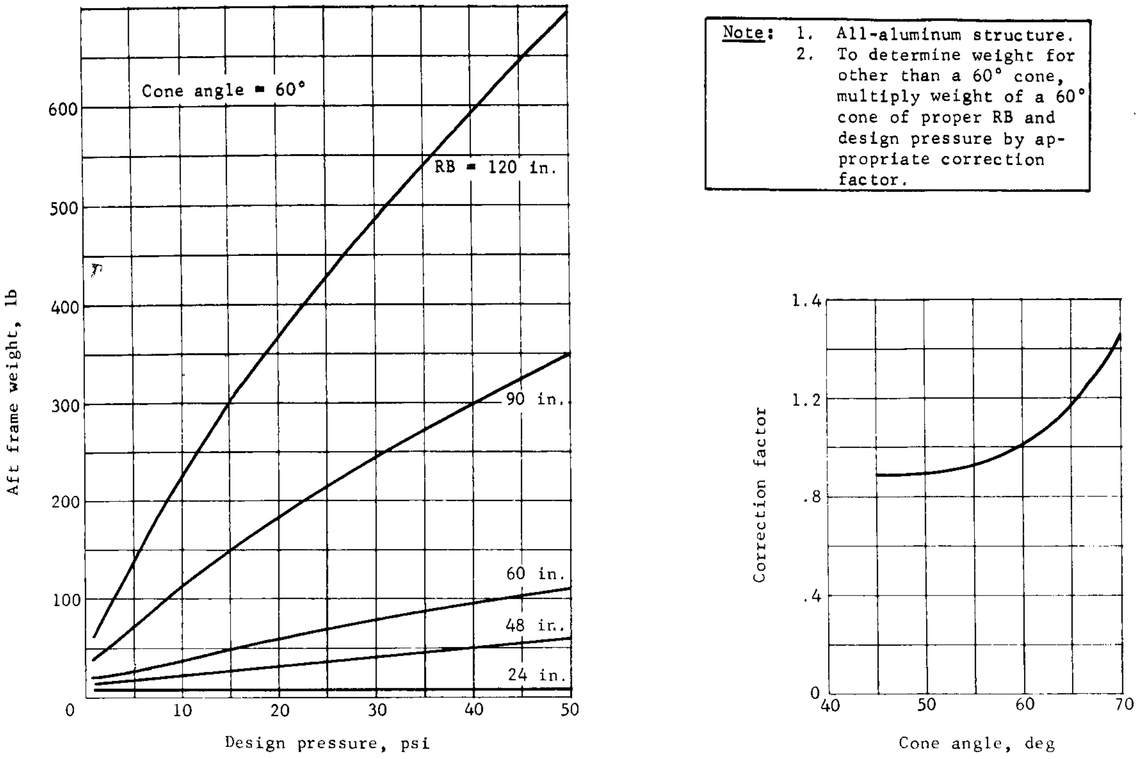

Note: 1. All-aluminum structure.
2. To determine weight for other than a 60° cone, multiply weight of a 60° cone of proper RB and design pressure by appropriate correction factor.

Figure C58.- Aeroshell Parametric Studies, Aft Frame Weight

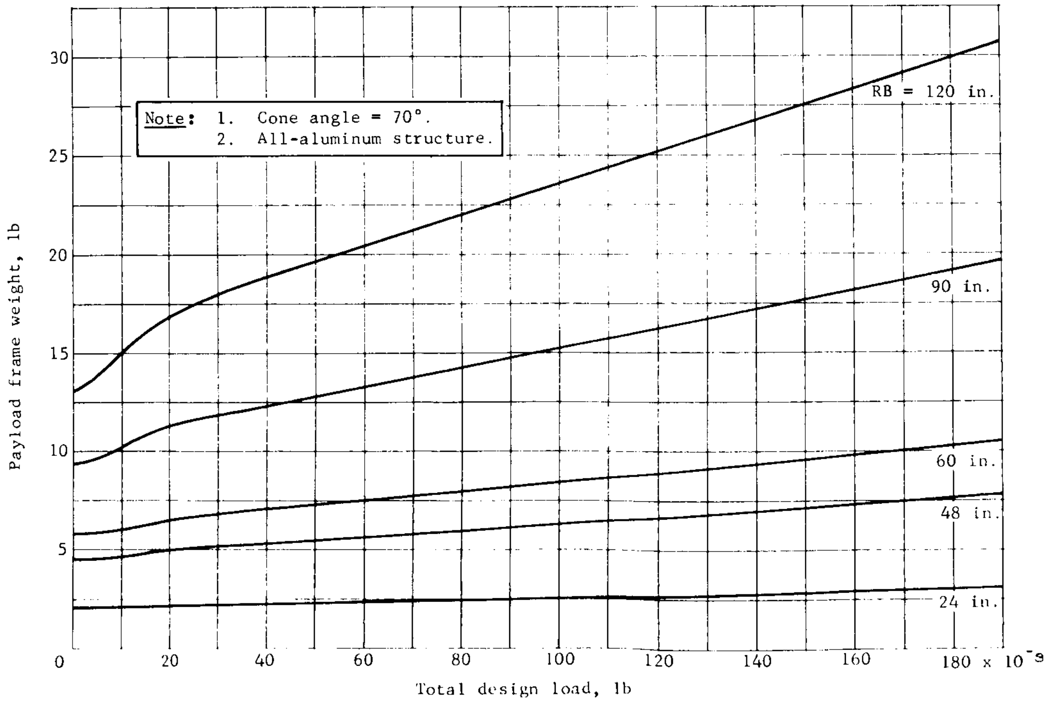

Note: 1. Cone angle = 70°.
2. All-aluminum structure.

Figure C59.- Aeroshell Parametric Studies, Payload Frame Weight

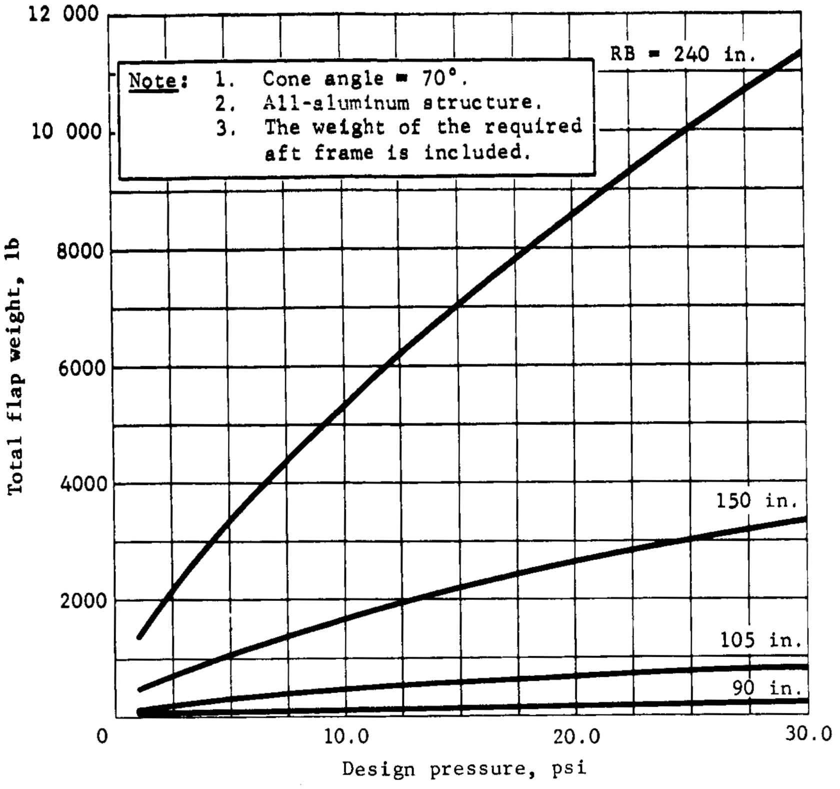

Figure C60.- Aeroshell Parametric Studies, Total Flap Weight

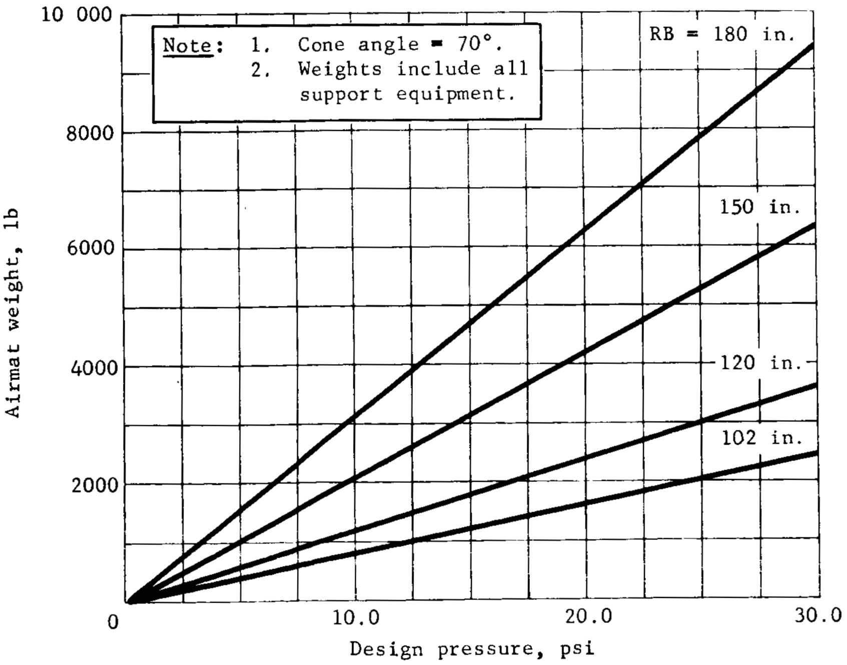

Figure C61.- Aeroshell Parametric Studies, Airmat Weight

APPENDIX C

Study Results

Figures C62 thru C75 represent the composite aeroshell weights, including ablator, for the entry trajectories indicated in the figure titles. Figures C62 and C63 are for the orbital entry mode and consider a rigid aeroshell from 6.5 to 20.0 ft in diameter at the base. Figures C64 thru C67 are for direct entry and consider rigid aeroshell from 6.5 to 15 ft base diameter. Figures C68 thru C75 are for the direct entry mode and consider a rigid aeroshell from 6.5 to 15.0 ft in diameter at the base with either rigid flaps or deployable airmat extensions up to an equivalent 30.0 ft base diameter. It should be noted that a break occurs in these curves at a ballistic coefficient of approximately 0.3. Two ablative materials were used in this study with a switchover from SLA-561 to PPA-1078 occurring when the maximum heating rate equaled or exceeded 100 Btu/ft^2-sec (see Section 2 of this appendix). The break in these curves is consistent with the change in ablator materials.

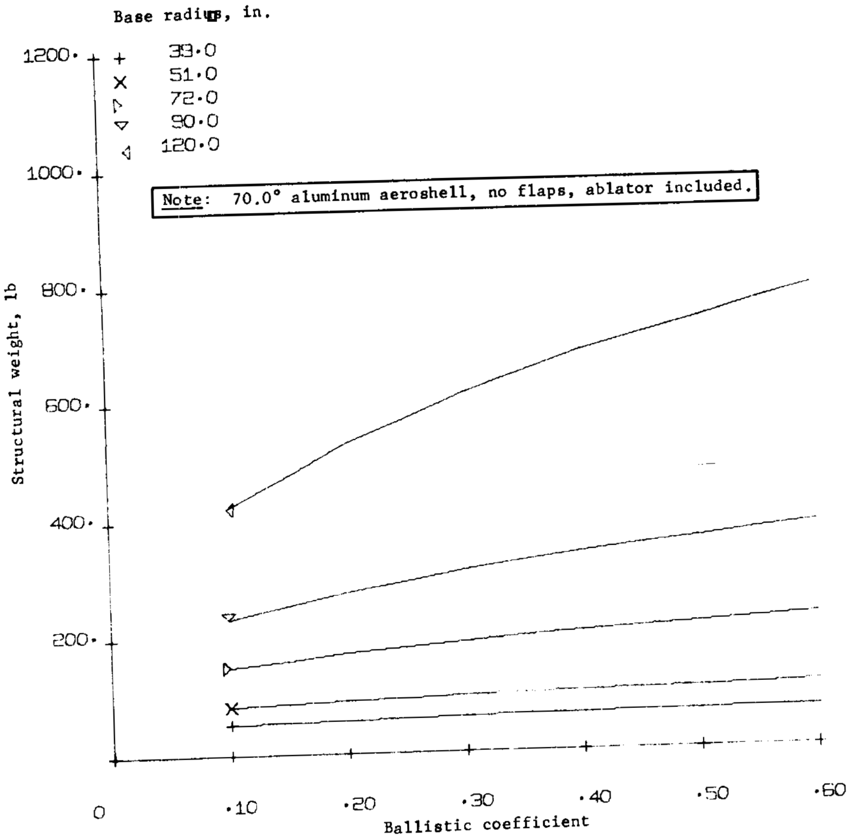

Figure C62.- Structural Weight, Orbital Entry, V_E = 14 765 fps, γ = -20°

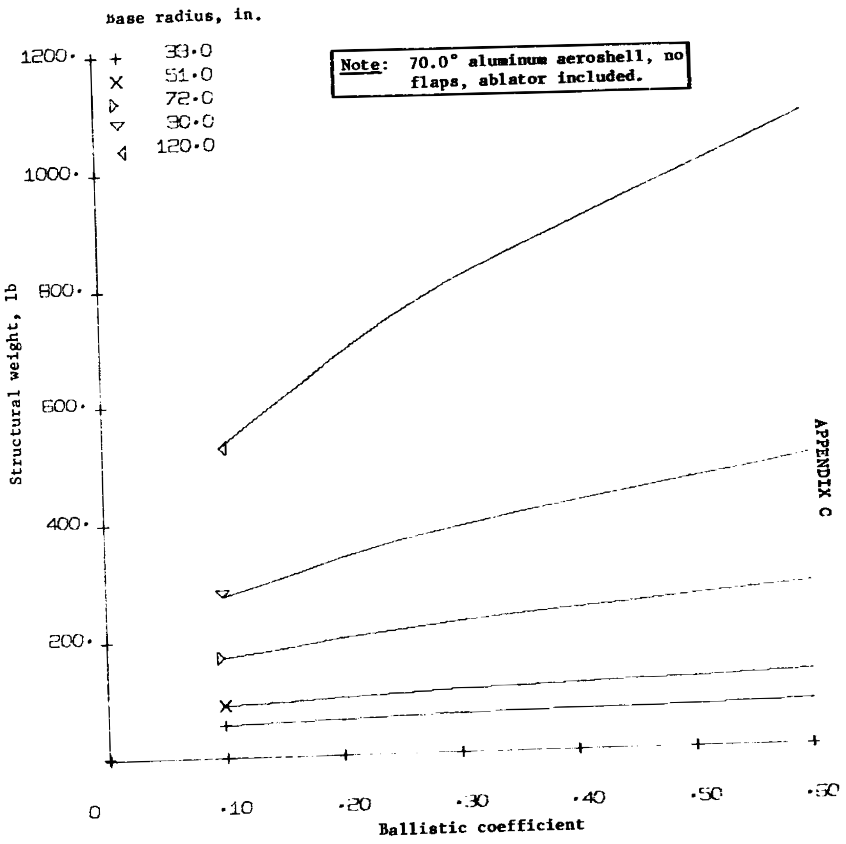

Figure C63.- Structural Weight, Orbital Entry, V_E = 14 765 fps, γ = -38°

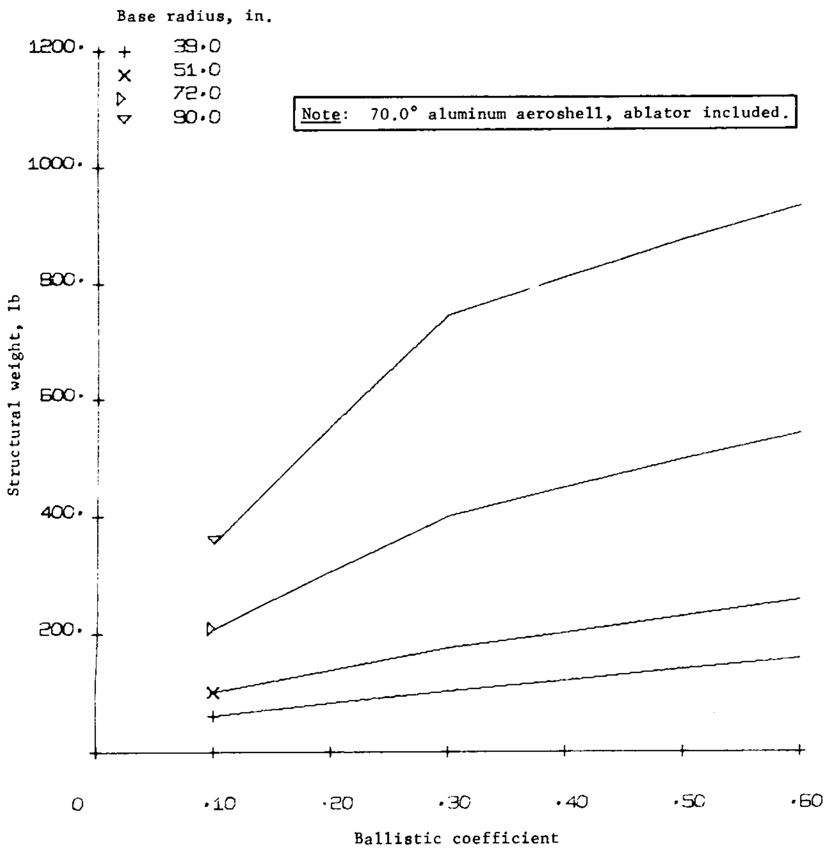

Figure C64.- Structural Weight, Direct Entry, V_E = 21 000 fps, γ = -30°

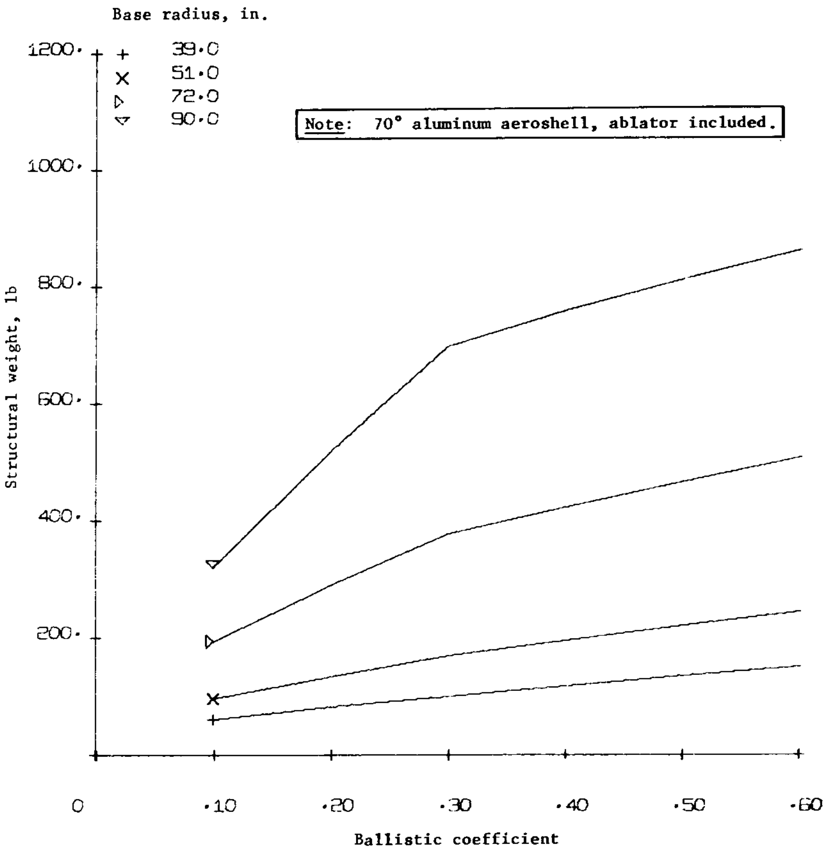

Figure C65.- Structural Weight, Direct Entry, V_E = 21 000 fps, γ = -38°

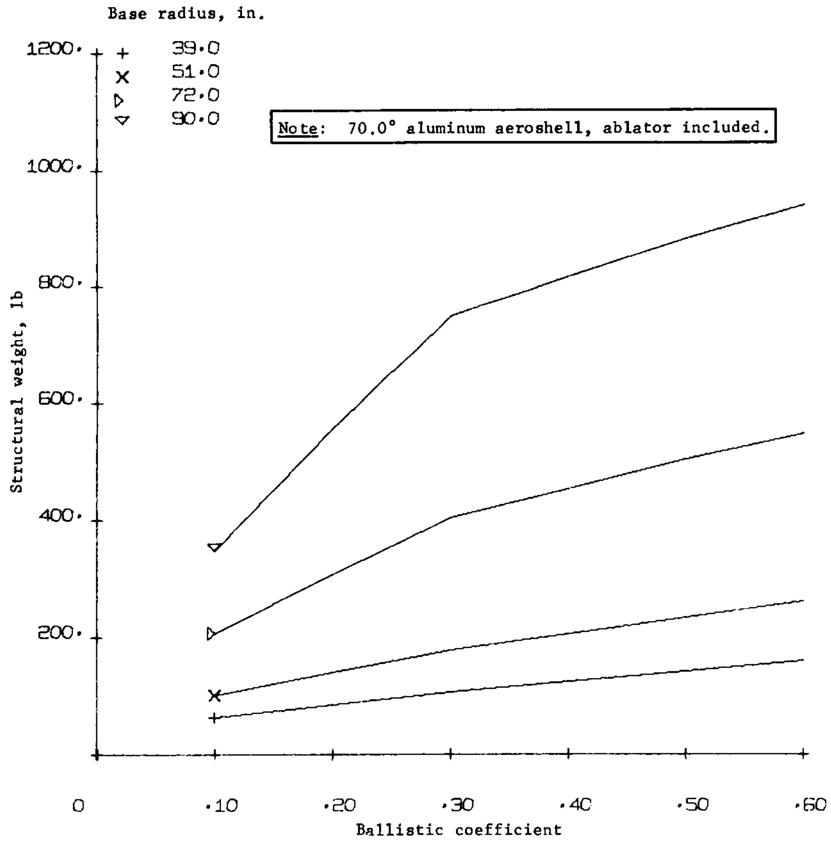

Note: 70.0° aluminum aeroshell, ablator included.

Figure C66.- Structural Weight, Direct Entry, V_E = 24 000 fps, γ = -30°

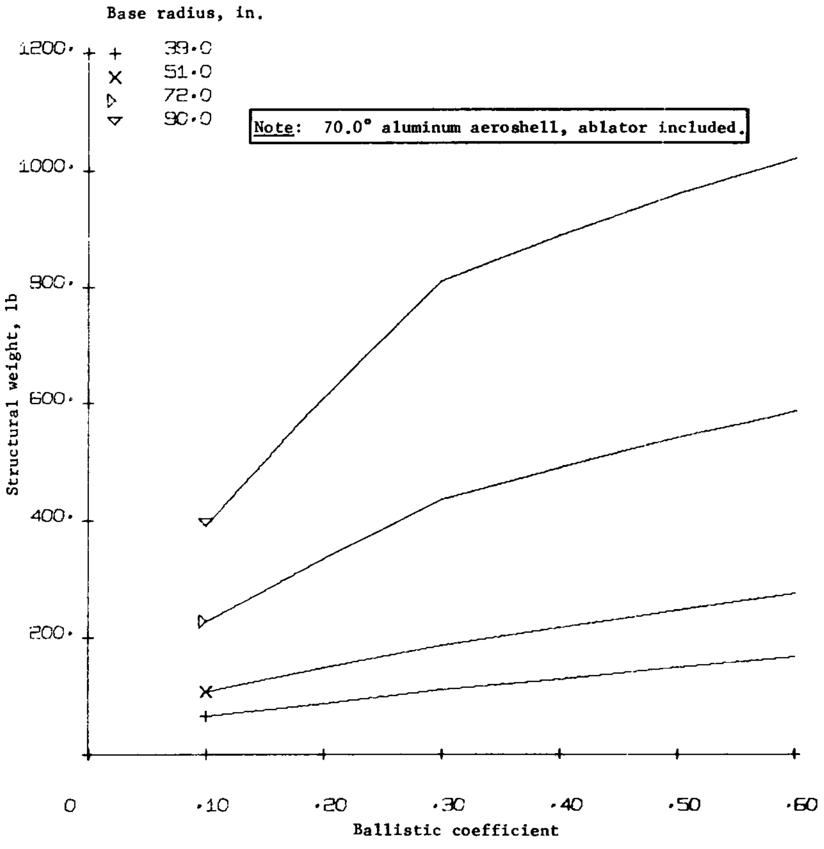

Note: 70.0° aluminum aeroshell, ablator included.

Figure C67.- Structural Weight, Direct Entry, V_E = 24 000 fps, γ = -38°

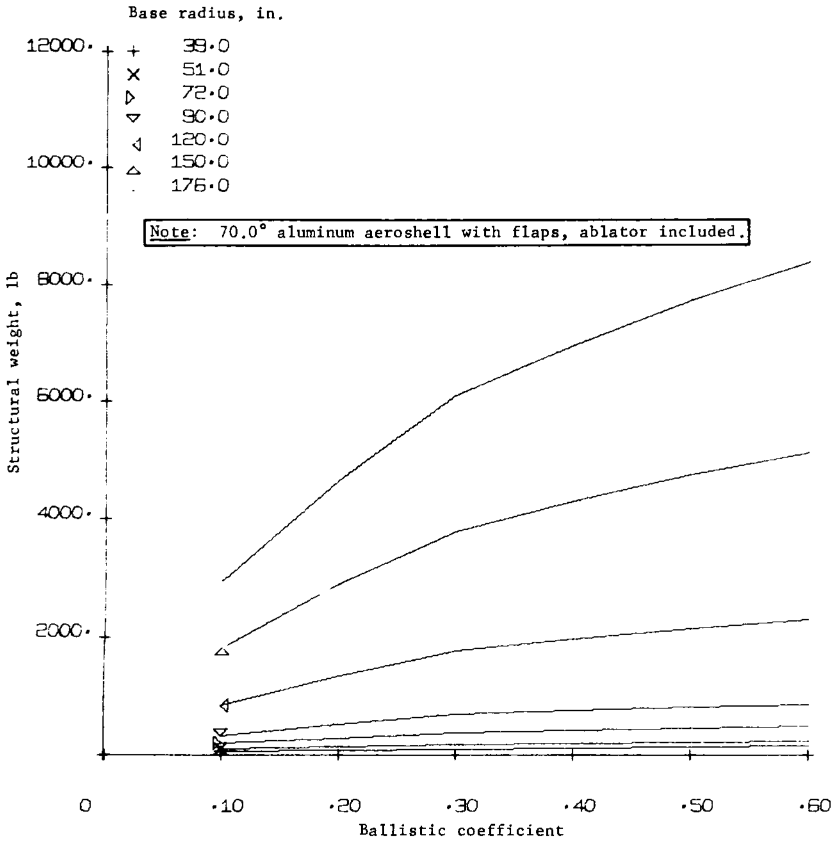

Figure C68.- Structural Weight, Direct Entry and Flaps, V_E = 21 000 fps, $\gamma = -30°$

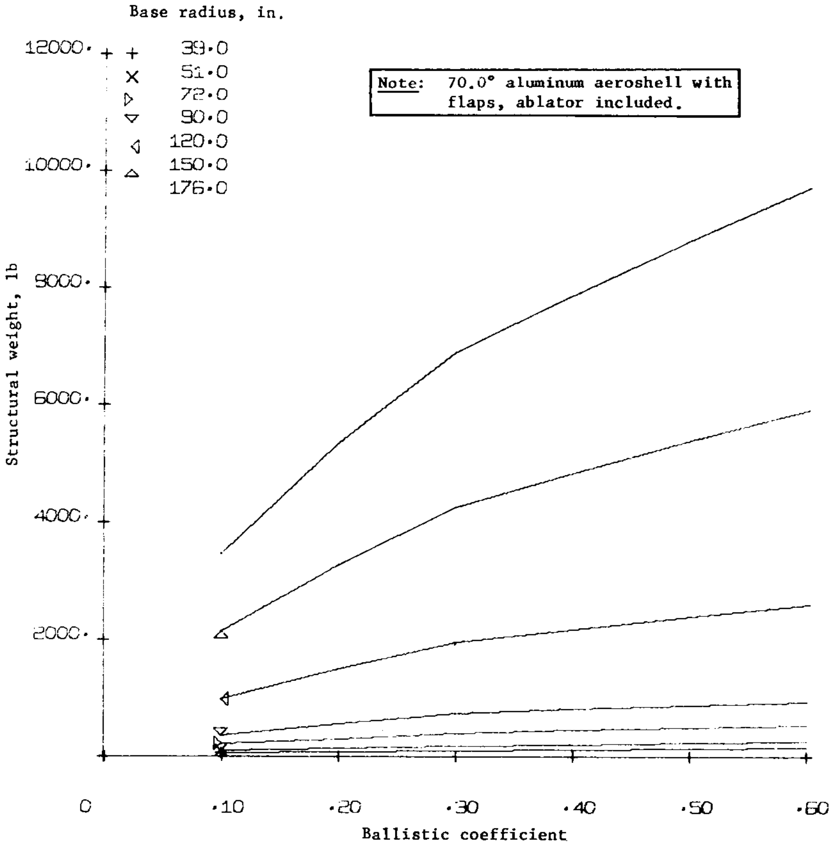

Figure C69.- Structural Weight, Direct Entry with Flaps, V_E = 21 000 fps, $\gamma = -38°$

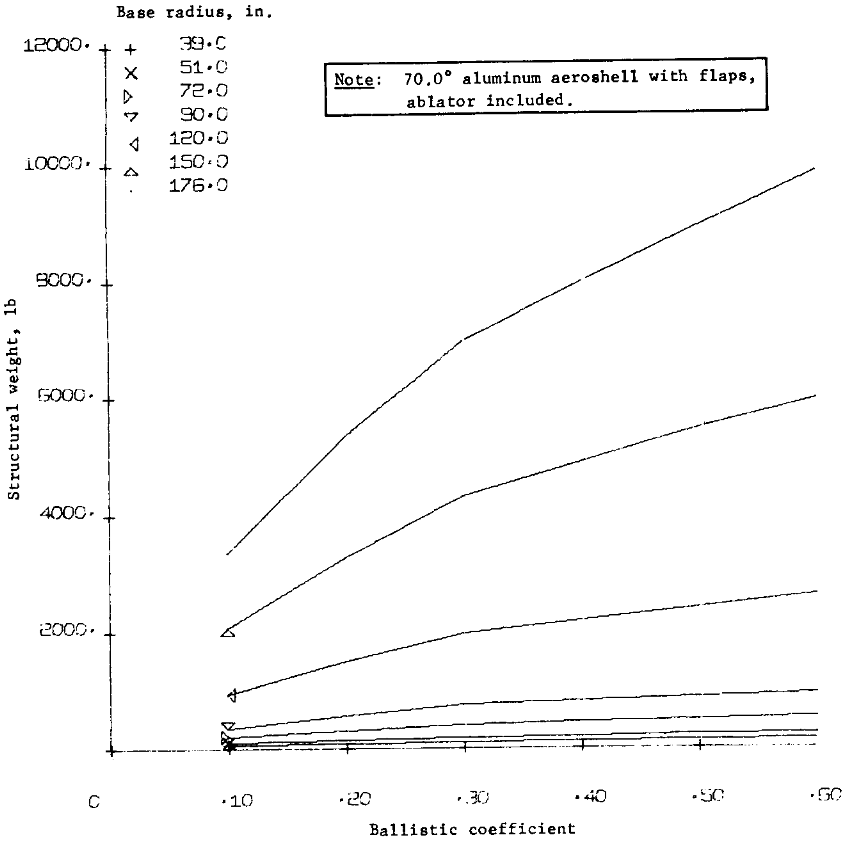

Figure C70.- Structural Weight, Direct Entry with Flaps, V_E = 24 000 fps, $\gamma = -30°$

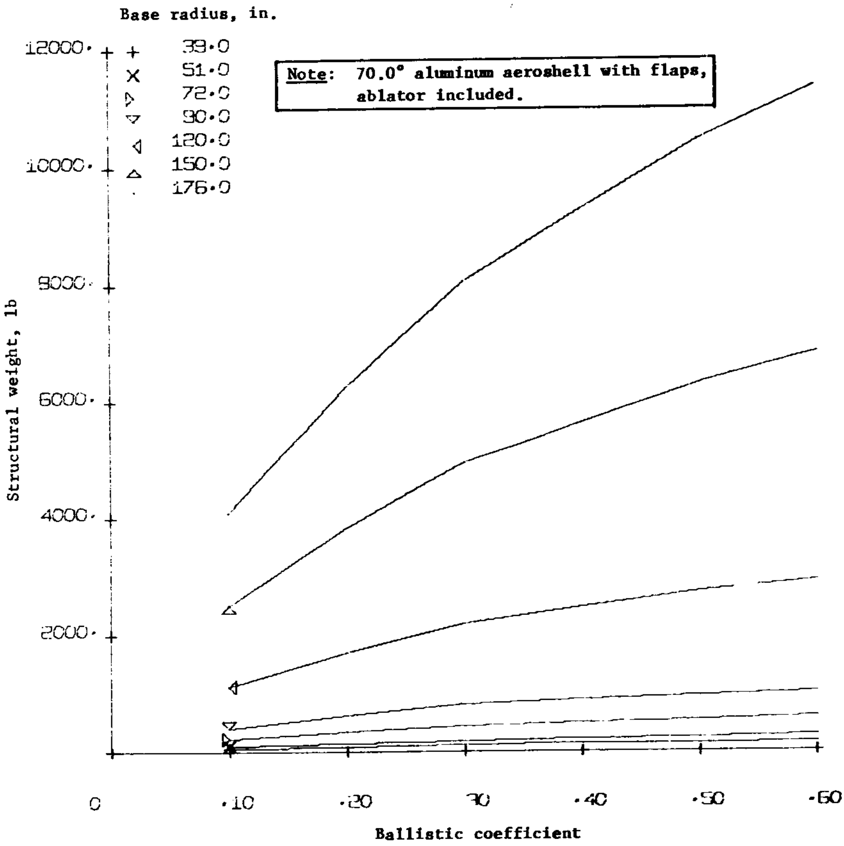

Figure C71.- Structrual Weight, Direct Entry with Flaps, V_E = 24 000 fps, $\gamma = -38°$

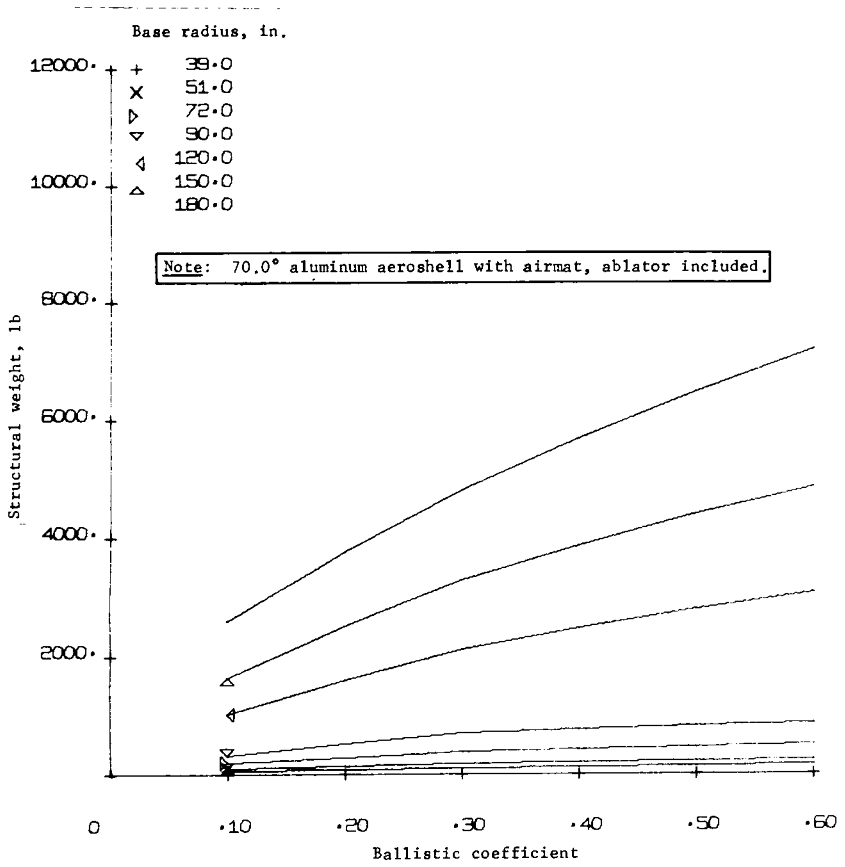

Figure C72.- Structural Weight, Direct Entry with Airmat, V_E = 21 000 fps, $\gamma = -30°$

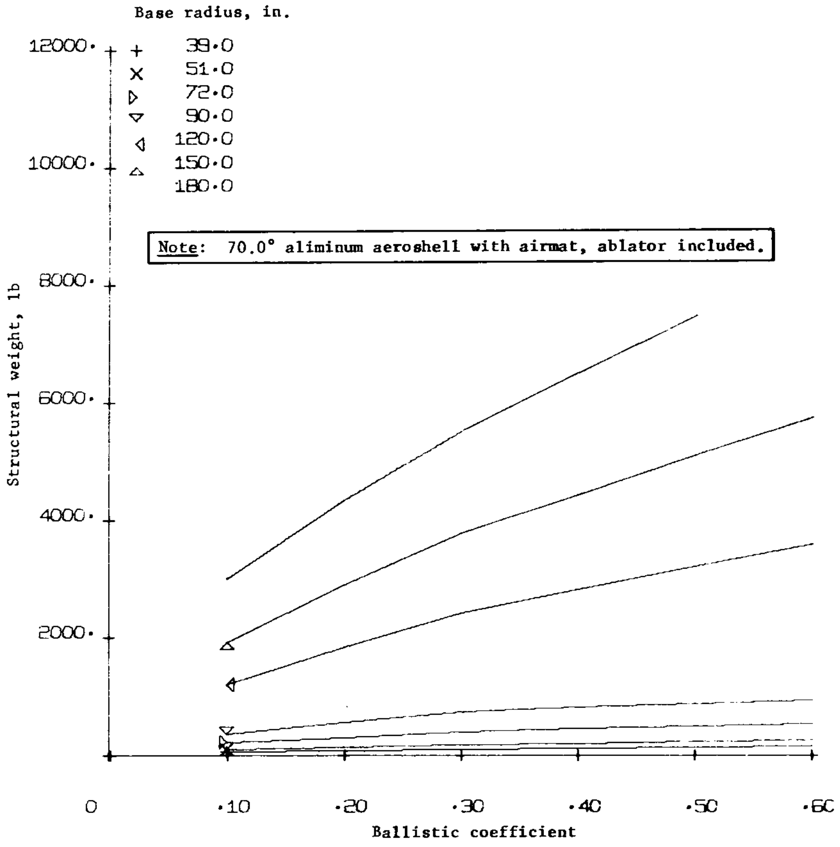

Figure C73.- Structural Weight, Direct Entry with Airmat, V_E = 21 000 fps, $\gamma = -38°$

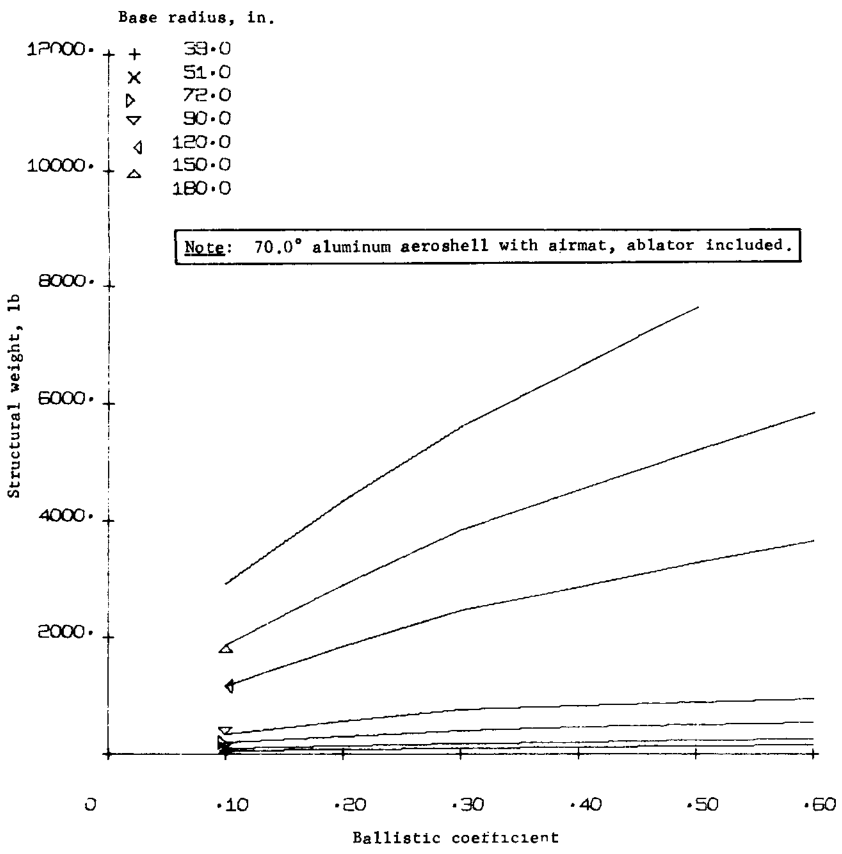

Note: 70.0° aluminum aeroshell with airmat, ablator included.

Figure C74.- Structural Weight, Direct Entry with Airmat, V_E = 24 000 fps, $\gamma = -30°$

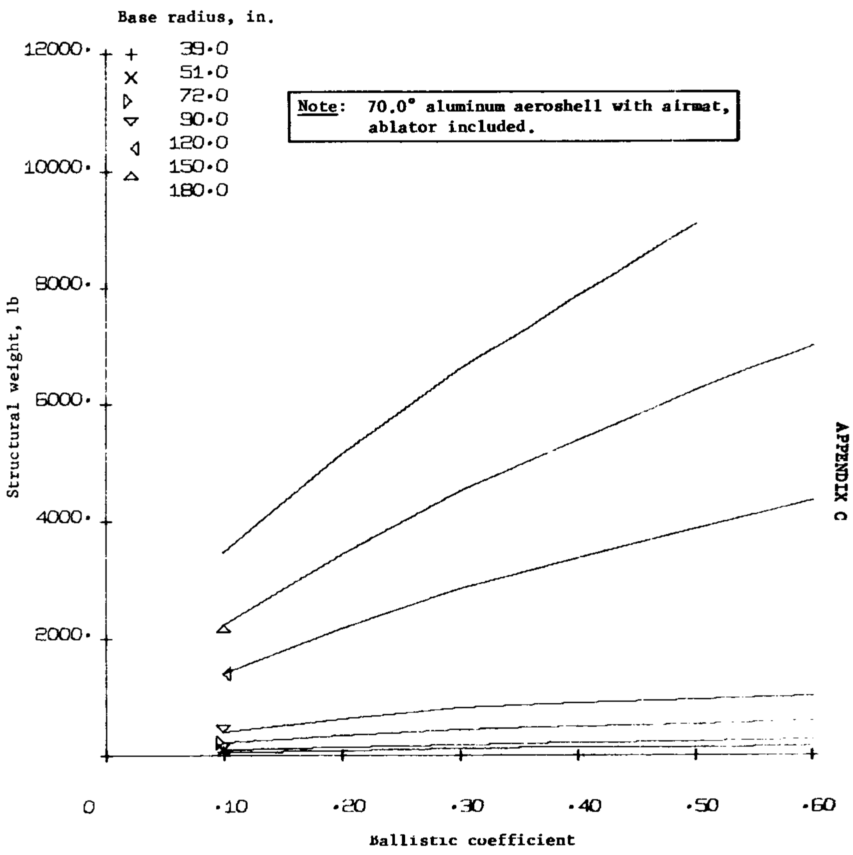

Note: 70.0° aluminum aeroshell with airmat, ablator included.

Figure C75.- Structural Weight, Direct Entry with Airmat, V_E = 24 000 fps, $\gamma = -38°$

APPENDIX C

Methods of Analysis for Conical Aeroshell Structure

The conical aeroshell structure for a planetary entry vehicle consists of four major components. They are:

1) Nose cap;
2) Conical shell or shells;
3) Aft stabilization frame;
4) Payload frame.

A discussion of the methods of analysis used to size and determine weights of these components is given below.

Nose cap. - The nose cap is designed as a monocoque shell with a constant radius of curvature. The method of analysis used is given on page 3.25-1 of reference C28. A simple equation is presented that allows determination of required thickness of a monocoque shell in terms of external pressure and radius of curvature.

$$t = \left[\frac{PR^2}{0.35E}\right]^{1/2}$$

where

t = required thickness

p = external pressure

R = radius of curvature

E = modulus of elasticity.

This equation applies for $4 < \lambda < 24$ where

$$\lambda = [12(1 - \mu^2)]^{1/4} \quad Ro/[Rt]^{1/2}$$

and

μ - Poisson's ratio

Ro - base radius of nose cap.

APPENDIX C

Conical shell structure. - Two methods of construction (sandwich, frame stabilized monocoque) have been considered for the shell structure of the aeroshell. Both methods assume a uniform external pressure on a conical shell simply supported at the boundaries. The basic equation for general instability of the shell structure is based on material given in reference C29 and results from experimental work on homogenous truncated cones subjected to external collapsing pressure. The expression for the general instability allowable is:

$$p = 0.736\ E \Big/ \frac{L}{R} \left(\frac{R}{t}\right)^{5/2}$$

where

p = allowable pressure, psi

E = modulus of elasticity, psi

L = slant length of the cone, in.

R = average slant radius of the cone, in.

t = thickness of cone skin, in.

The above equation, modified as required, and additional equations required for local instability checks were used to analyze the conical shells as discussed below.

Sandwich shells: The sandwich shells are analyzed as one or two truncated cones depending on the location of the payload frame. The analysis assumes both cones to be hydrostatically loaded, i.e., the cones are subjected to a compressive longitudinal stress. The analysis assumes that structures having equal radii of gyration, in the circumferential direction, will work to the same stress level before becoming unstable. By equating radius of gyration,

$$\left|\frac{btm^3}{12\ btm}\right|^{1/2} = \left|\frac{2\ btsd^2}{2\ bts}\right|^{1/2}$$

solving for tm

$$tm = \sqrt{12}\ d$$

and using the assumption of equal stress,

$$Pm\ R/tm = Ps\ R/2ts$$

$$Ps = 2ts\ Pm/tm$$

the general instability equation becomes:

$$p = \frac{9.49\ E\ ts\ d^{3/2}}{LR^{3/2}}$$

where

tm = monocoque thickness, in.

b = unit width, in.

ts = sandwich face thickness, in.

d = distance from sandwich centroid to centroid of face sheet, in.

It is assumed that core cell size is small enough to preclude intercellular buckling of the face sheets.

The above equation has been incorporated in a program written for the IBM 1130 computer that will determine optimum weight sandwich shells within the limits of minimum face thickness and minimum and/or maximum core height. Included are weight for the required core, bonding agent between face sheets and core, and appropriate edge members to allow manufacturing of a segmented aeroshell.

Frame stabilized monocoque shells: Frame stabilized monocoque shells were analyzed as one or two shells depending on the location of the payload frame with a differentiation in the type of loading being considered if the shell were forward or aft of the payload frame. Shells forward of the payload frame were considered hydrostatically loaded and shells aft of the payload frame were considered radially loaded by a uniform external pressure. The analysis assumes that structures have equal radii of gyration, in the circumerential direction, will work to the same stress level before becoming unstable. With this assumption, the general instability equation becomes:

$$P = \frac{0.736\ E\ \bar{t}}{LR^{3/2}} \left(\frac{12\ I}{b\bar{t}}\right)^{3/4}$$

where

$\bar{t}$ = smear thickness of structure over a width b, in.

I = moment of inertia of the structure over a width b and about an axis parallel to the shell skin, in.^4

b = frame spacing at the average radius of the cone, in.

In addition to a general instability check, the following checks are made on the detail shell structure:

1) Local instability of intermediate frame elements;

2) Local instability of the shell;

3) Local yield of any shell element.

The local instability check for the intermediate frame elements is expressed in general form as:

$$p = \frac{KR\pi^2 E}{12(1 - \mu^2)} \left(\frac{tr}{br}\right)^2 \left(\frac{\bar{t}}{R}\right)$$

where

K = a coefficient that is a function of the frame element boundary conditions

R = local radius of curvature of the shell, in.

tr = frame element thickness, in.

br = frame element width, in.

Local instability of the cone skin, between frames, is checked by the use of two expressions. The first assumes the skin to be in infinitely long flat panel simply supported at the edges. The second assumes the skin to be a truncated homogenous cone. The higher allowable of these two expressions is used:

1) $p = \frac{CE\bar{t}}{R} \left(\frac{ts}{b}\right)^2$

2) $p = \frac{0.736\ E\bar{t}\ ts^{3/2}}{bR^{3/2}}$

where

C = a coefficient that is a function of the skin element boundary conditions

ts = skin thickness

$\bar{t}$ = smear thickness

R = local radius of curvature

b = frame spacing.

The analysis consists of selecting the appropriate element sizes so that all the stability checks are satisfied, the structure will not be critical in yield, and a minimum weight structure will be achieved. This method of analysis was suggested by and has been compared to those proposed in references C30 and C31 and shows very good agreement. Results using this method are slightly more conservative than those using the methods of analysis from references C30 and C31.

A program for the IBM 1130 computer has been written to perform the analysis. The program will handle structure with rectangular-integral frames or channel frames. Variables input to the program include cone angle, minimum gages and dimensions on all elements, design pressure, material allowables, etc. Output consists of detail dimensions, allowables, and weights.

Aft stabilization frame. - The shell analysis considers general instability failure through multiwave buckling of the shell with the ends of the cone assumed to be supported. An end or edge frame is required to provide this support and to prevent general instability in the N = 2 mode of buckling. Because of the restraint provided by the basic shell, the frame will be forced to buckle out-of-plane. The frame moment of inertia required to prevent this buckling is given by the expression

$$I = \frac{a^4 p \tan^2 \alpha \sin^2 \alpha}{9E}$$

where

a = slant length of cone extended to the apex, in.

p = load on frame, lb/in.

α = 1/2 the included angle of the cone.

APPENDIX C

A program for the IBM 1130 computer has been written to size a minimum weight frame that will satisfy general and local instability requirements.

Payload frame. - The payload frame consists of structure to redistribute the payload weight, during entry, into a fairly uniform load into the shell structure of the aeroshell. The payload frame was analyzed as a circular stable web beam on the elastic foundation provided by the aeroshell shell structure. The method of analysis assumes a straight beam equal in length to the circumference of the payload frame and matched end conditions on either end of the frame. The analysis ignored the stiffness provided by hoop continuity of the frame and, therefore, give adequate but conservative results. A program was written for the IBM 1130 computer to size a minimum weight frame that will satisfy stiffness, stability, and strength requirements.

Rigid Deployable Flaps, Weight Analysis

The rigid deployable flap configuration is shown in figure C52 of this appendix. Entry pressure loads are reacted primarily by bending of the sandwich surface structure and twisting moments on the aeroshell aft frame. The longitudinal members in the flaps were positioned to minimize spanwise bending in sandwich surface structure. The link mechanisms were positioned on the flap longitudinal members to minimize bending in these members. The aft frame was treated as a circular torque box and designed by stiffness requirements. Rotation of the aft frame was restricted to an arbitrary 1°. Standard methods of analysis were used on the flap structure and will not be detailed here.

Airmat* Cone Weight Analysis

The airmat cone system is a means of expanding the aeroshell in the form of a continuous inflatable extension as indicated in figure C76. The total system weight is expressed by

$$W_{AM} = W_{cloth} + W_{gas} + W_{tank} + W_{plumbing} + W_{accessories}$$

---

*TM, Goodyear Aerospace Corporation.

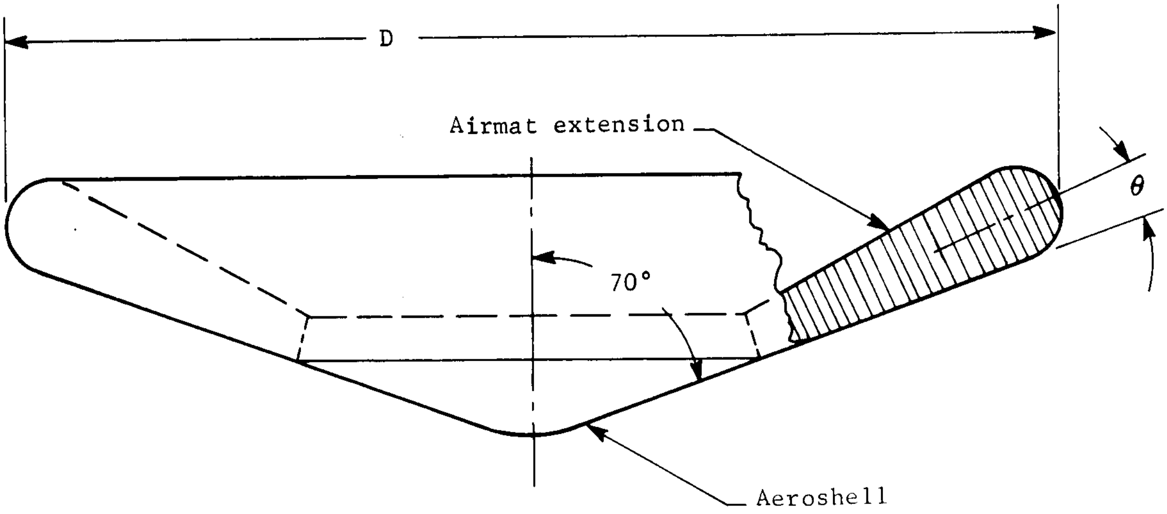
D
Airmat extension
θ
70°
Aeroshell

Figure C76.- Airmat Cone Configuration

APPENDIX C

where

W_{cloth} = weight of sealed fabric required to make the truncated cone extension

W_{gas} = weight of inflating, chosen as H_2 in this study

W_{tank} = storage tank weight

$W_{plumbing}$ = piping, valve, fittings, etc.

$W_{accessories}$ = weight of attachment, release, and stowage devices.

In this application the airmat is deployed and inflated to final entry configuration before the vehicle comes in contact with a sensible planetary atmosphere. This approach requires a full inflation system be provided.

The expressions for elemental weights are given below and, in the case of the cloth and accessories weights, are derived from Goodyear Aerospace Corporation analyses and supporting data (GAC report GER-12842, October, 3 1966).

$$W_{cloth} = \frac{3 C p q \pi D^3}{8} \cdot \frac{\tan \alpha}{K_{fa} \sin^2 \alpha} \left[\frac{(\cot \theta + \pi) \tan \theta - 1}{1 + \frac{\tan \theta}{\sin \alpha}} \right] \left[\frac{\frac{2 K_e}{\cos \theta} + 1}{1 + \frac{\tan \theta}{\sin \alpha}} \right] (\text{F.S.})$$

As it concerns this study, values used in this expression are:

C_p = 2.5

q = maximum free-stream dynamic pressure, from trajectory analysis

D = diameter of cone (see fig. C76)

K_{fa} = 38 900 ft (coated-Nomex fabric)

K_e = 1.0 (GAC recommendation)

$$\left.\begin{aligned} \theta &= 5^\circ \\ \alpha &= 70^\circ - \theta = 65^\circ \end{aligned}\right\} \text{(see fig. C76)}$$

F.S. = 2.0 (GAC recommendation).

APPENDIX C

With values above substituted,

$$W_{cloth} = 9.06\ (10^{-5})q\ D^3$$

$$W_{gas} = \frac{qV}{54\ 200}$$

where V = volume of cone extension

$$W_{tank} = 15\left(W_{gas}\right)$$

$$W_{plumbing} = 35\ \text{lb}$$

constant for all sizes

$$W_{accessories} = 0.0018q\ D_D^2$$

derived from GAC point design data.

APPENDIX C

4. REFERENCES

C1. Anon.: Statement of Work, Mars Mission Mode Study, Contract NAS1-7976. NASA-Langley Research Center.

C2. Anon.: Voyager Capsule Preliminary Design (Phase B) Final Report. FR-22-103 (Contract 952001), Martin Marietta Corporation, Denver, Colorado, Aug. 1967.

C3. Anon.: Parametric Aeroheating Data. ED-22-68-23, Martin Marietta Corporation, Denver, Colorado, June 1968.

C4. Horton, T. E.: The JPL Thermochemistry and Normal Shock Computer Program. JPL TR-32-660, Nov. 1964.

C5. Arave, R. J.: Approximate Thermodynamic, Transport, and Electrical Properties of High-Temperature Air. D2-11781 Boeing Company, 1963.

C6. Van Tassell, W.: Convective Heating in Planetary Atmospheres. RAD-TM-63-72, AVCO, Oct. 1963.

C7. Yos, J. M.: Transport Properties of Nitrogen, Hydrogen, Oxygen, and Air to 30 000°K. RAD-TM-63-7, AVCO, Mar. 1963.

C8. Marvin, J. G.; and Pope, R. B.: Laminar-Convective Heating and Ablation in the Mars Atmosphere. AIAA J., vol. 5, no. 2, Feb. 1967.

C9. James, C. S.: Experimental Study of Radiative Transport from Hot Gases Simulating in Composition the Atmospheres of Mars and Venus. AIAA J., vol. 2, no. 3, Mar. 1964.

C10. Arnold, J. O.; Reis, V. H.; and Woodward, H. T.: Studies of Shock-Layer Radiation of Bodies Entering Planetary Atmospheres. AIAA J., vol. 3, no. 11, Nov. 1965.

C11. Thomas, G. M.; and Menard, W. A.: Experimental Measurements of Nonequilibrium and Equilibrium Radiation from Planetary Atmospheres. AIAA Publ CP 9, 1964, pp. 170-185.

C12. Gruszczynski, J. S.; and Warren, W. R., Jr.: Experimental Heat-Transfer Studies of Hypervelocity Flight in Planetary Atmospheres. AIAA J., vol. 2, no. 9, Sep. 1964.

C13. Deacon, H. R., Jr.; and Boughner, R. E.: Equilibrium Radiative Heating of Shocked CO_2. AIAA J., vol. 5, no. 7, July 7, 1967.

C14. Kivel, B.; and Bailey, K.: Tables of Radiation from High-Temperature Air. Research Rep. AVCO, Dec. 21, 1957.

C15. French, E. P.: Approximate Absorption Coefficients for Vibrational Electronics Band System. AIAA J., vol. 2, no. 12, Dec. 1964.

C16. Wolf, F.; and Spiegel, J. M.: Status of Basic Shock Layer Radiation Information for Innerplanet Atmospheric Entry. AIAA Paper no. 66-421, June 1966.

C17. Menees, G. P.; and McKenzie, R. L.: A Simplified Chemical Model for Estimating the Nonequilibrium Radiant Emission of CN (violet) in Shock-Heated Mixtures of CO_2 and N_2. AIAA J., vol. 6, no. 3, Mar. 1968.

C18. Kemp, H. N.; Rose, P. H.; and Detra, R. W.: Laminar-Heat Transfer Around Blunt Bodies in Dissociated Air. JAS, vol. 26, no. 7, July 1959.

C19. Fay, J. A.; and Riddell, F. R.: Theory of Stagnation Point Heat Transfer in Dissociated Air. JAS, vol. 25, no. 2, Feb. 1958.

C20. Stetson, K. F.: Boundary-Layer Transition on Blunt Bodies with Highly Cooled Boundary Layers. JAS, vol. 27, no. 2, Feb. 1960.

C21. Hearne, L. F.; Chine, J. H.; and Woodruff, L. W.: Study of Aerothermodynamic Phenomena Associated with Reentry of Manned Spacecraft. Lockheed Missiles and Space Co. (Contract NASA 9-3531), May 1966.

C22. Jones, R. A.: Experimental Investigation of the Overall Pressure Distribution, Flow Field, and Afterbody Heat-Transfer of an Apollo Reentry Configuration at a Mach Number of 8. NASA TM X-813, June 1963.

C23. Lee, G.; and Sundell, R. E.: Heat Transfer and Pressure Distributions on Apollo Models at M = 13.8 in an Arc-Heated Wind Tunnel. NASA TM X-1069, Feb. 1965.

C24. Murphy, J. D.: Flight Test Aerodynamic Heating Data for the Afterbody of the Project Mercury Spacecraft with Comparisons to Available Prediction Methods. NASA CR-694, 1967.

C25. Stephenson, J. D.: Measurements of Optical Radiation from the Wake of Ablating Blunt Bodies in Flight at Speeds up to 10 Kilometers per Second. NASA TN D-2760, 1965.

C26. Strauss, E. L.: Research on Superlight Ablators for Mars Lander Thermal Protection. RM-321, Martin Marietta Corporation, Baltimore, Maryland, Feb. 1967.

C27. Strauss, E. L.: Development and Evaluation of Foamed Silicone Ablators. RM-309, Martin Marietta, Baltimore, Maryland, June 1966.

C28. Baker, E. H., et al.: Shell Analysis Manual, NASA/SID 66-398, June 1966.

C29. Weingarten, V. I.; Morgan, E. J.; and Seide, P.: Final Report on Development of Design Criteria for Elastic Stability of Thin Shell Structures. STL/TR-60-0000-19425, Space Technology Laboratories, Dec. 1960.

C30. Wickell, E. H.; and Crawford, R. F.: Optimum Ring Stiffened Cylinders Subjected to a Uniform Hydrostatic Pressure. Paper no. 578F, Society of Automotive Engineers, Oct. 1962.

C31. Baruck, Monsham; Singer, Josef; and Harari, Ovaclic: General Justability of Conical Shells with Nonuniformly Spaced Stiffeners under Hydrostatic Pressure. Israel TAE Report 37, Israel Institute of Technology-Department of Aeronautical Engineer, Haifa.